USER-CENTERED ARTIFICIAL INTELLIGENCE FOR HIGH SPATIAL URBAN FLOOD MAPPING

A Dissertation

by

BAHAREH ALIZADEH KHARAZI

Submitted to the Graduate and Professional School of
Texas A&M University
in partial fulfillment of the requirements for the degree of

DOCTOR OF PHILOSOPHY

Chair of Committee,	Amir H. Behzadan
Committee Members,	Ashrant Aryal
	Maria Koliou
	Michelle Meyer
	Xinyue Ye
Head of Department,	Phil Lewis

May 2023

Major Subject: Construction Science

ABSTRACT

The number and intensity of flood events have been on the rise in many regions of the world. In some parts of the U.S., residential properties, transportation networks, and major infrastructure are at risk of failure caused by floods. The vulnerability to flooding, particularly in coastal areas and among marginalized populations is expected to increase as the climate continues to change, thus necessitating more effective flood management practices that consider various data modalities and innovative approaches to monitor and communicate flood risk. With the goal of improving the quality of decisions made during flood events to evacuate people or move goods and services while avoiding flooded areas, this study first conducted a community needs assessment that highlighted the need for real-time data on floodwater conditions, risk-informed evacuation plans, and safe and shortest transit routes. Research points to the importance of reliable information about the movement of floodwater as a critical decision-making parameter in flood evacuation and emergency response. Existing flood mapping systems, however, rely on sparsely installed flood gauges that lack sufficient spatial granularity for precise characterization of flood risk in populated urban areas. To address these needs, this study utilizes crowdsourced photos of submerged stop signs to generate street-level flood maps with high spatial resolution (compared to flood gauge data), and develop risk-informed evacuation plans during floods by comparing sign's pole length in a paired photo (before and after a flood). To enable crowdsourced data collection, a web application, called Blupix, is designed and launched. Images collected by the Blupix app are analyzed using two developed computer

vision models (Computer Vision Model I and Computer Vision Model II) and validated. Next, two route optimization algorithms are implemented and compared based on the generated inundation map to determine the shortest flood-free evacuation route. Next, a mobile application (called Blupix Mobile) is developed with embedded computing functionality for on-demand floodwater depth estimation from geocoded photos of submerged stop signs which provide ordinary people and first response teams with reliable, ad-hoc flood water depth information. Finally, a user study is conducted to assess human's perception of flood risk using immersive virtual reality (VR).

DEDICATION

My dear father, Mohammad Masoud Alizadeh Kharazi, who supported and guided me to face this world and inspired me most about my higher educations, my dear mother, Masomeh Zarforoushan, who always supported me, cared, and loved most, and my dear brother, Behnam Alizadeh Kharazi for always encouraging me to pursue my dreams and aim high. They always supported me in every single step of my life.

ACKNOWLEDGEMENTS

I would like to specially thank my committee chair, Professor Amir H. Behzadan, and my committee members, Professor Michelle A. Meyer, Professor Xinyue Ye, Professor Maria Koliou, and Professor Ashrant Aryal, for their guidance and support throughout the course of this research.

I would also to thank Mr. Diya Li (Ph.D. student at Texas A&M University) for his assistance in developing GIS based flood depth mapping, route optimization algorithms, and for overseeing Blupix application design and content maintenance. I would also like to thank Mr. Nathan Young (undergraduate student at Texas A&M University) for his assistance in data collection for this project. I would also like to acknowledge the support of Mr. Greg Spiller and Mr. Chris Mouchyn (College of Geosciences IT professionals at Texas A&M University) for hosting the Blupix application on the web.

I would also to thank my lab mates Md Nazmus Sakib, Chih-Shen Cheng, and Nipun Nath for their suggestions, assistance and overall making my doctoral program more enjoyable. Thanks also go to my friends and colleagues, and the department faculty and staff for making my time at Texas A&M University a great experience.

Finally, special thanks to my mother, father and brother for their encouragement and ultimate support throughout this journey.

CONTRIBUTORS AND FUNDING SOURCES

Contributors

This work was supervised by a dissertation committee consisting of Professor Amir H. Behzadan [advisor] of the Department of Construction Science, Dr. Michelle Meyer of the Department of Urban and Regional Sciences, Professor Xinyue Ye of the Department of Urban and Regional Sciences, Professor Maria Koliou from the Department of Civil Engineering, Professor Ashrant Aryal from the Department of Construction Science.

The survey and complementary analyses presented in Chapter III were conducted in part by Julia Hillin (graduate student) and Professor Courtney Thompson of the Department of Geography. The data analyses described in Chapter V were conducted in part by Diya Li (graduate student) and Professor Zhe Zhang of the Department of Geography.

All other work conducted for the dissertation was completed by the student independently.

Funding Sources

This study is funded by award #NA18OAR4170088 from the National Oceanic and Atmospheric Administration (NOAA), U.S. Department of Commerce, under the Texas Sea Grant program. Any opinions, findings, conclusions, and recommendations expressed in this study are those of the author and do not necessarily represent the views

of the NOAA, Department of Commerce, Texas Sea Grant program, or the individuals named above.

NOMENCLATURE

AI	Artificial intelligence
AIIMS	Australasian Inter-service Incident Management System
AP	Average Precision
AP	Average Precision
BiFPN	Bi-Directional Feature Pyramid Network
CIMS	Coordinated Incident Management System
CNNs	Convolutional Neural Networks
CSP	Cross-stage-partial-connections
DEM	Digital Elevation Model
DEM	Digital Elevation Models
DSSD	Deconvolutional Single Shot Detector
FCN	Fully Convolutional Networks
FEMA	Federal Emergency Management Agency
FN	False Negative
FP	False Positive
FPN	Feature Pyramid Network
FPN	Feature Pyramid Network
FPSFPS	Frames per second
FwDET	Floodwater Depth Estimation Tool
GCP	Google Cloud Platform

GIS	Geographic Information System
GSV	Google Street View
HCI	Human Computer Interaction
HRRC	Hazard Reduction and Recovery Center
IoU	Intersection over Union
JESIP	Joint Emergency Services Interoperability Program
LiDAR	Light Detection and Ranging
MAE	Mean Absolute Error
mAP	Mean Average Precision
MUTCD	Manual on Uniform Traffic Control Devices
NEXRAD	Next Generation Weather Radar
NFIP	United States National Flood Insurance Program
NGOs	Nongovernmental Organizations
NIMS	National Incident Management System
RoI	Region of Interest
RPN	Region Proposal Network
RSME	Root Mean Square Error
SAR	Synthetic-Aperture Radar
SDSS	Spatial Decision Support System
SPP	Spatial Pyramid Pooling
SSD	Single Shot Detector
TAM	Technology Acceptance Model

TP	True Positive
TTC	Texas Target Communities
USGS	United States Geological Survey
VR	Virtual Reality
YOLO	You Only Look Once

TABLE OF CONTENTS

Page

ABSTRACT ii

DEDICATION iv

ACKNOWLEDGEMENTS v

CONTRIBUTORS AND FUNDING SOURCES vi

NOMENCLATURE viii

TABLE OF CONTENTS xi

LIST OF FIGURES xv

LIST OF TABLES xviii

CHAPTER I INTRODUCTION 1

Flood: The Most Prevalent Natural Hazard 1
Historical Perspective of Floods 1
Current Patterns and Future Outlook of Floods 4
Flood Management and Response by Rescue Operators 5
Access to Information in Flood Evacuation 6
Flood Risk Perception 7
Research Context 9
Gaps in Knowledge and Practice 9
Dissertation Outline 11

CHAPTER II EXISTING FLOOD MONITORING AND DATA PROCESSING CAPACITIES 14

FEMA Flood Maps 14
Flood Gauges and Water Level Sensors 15
Advanced Flood Mapping Tools 18
Computer Vision for Flood Depth Estimation 19
Remote Sensing 20

CHAPTER III DATA NEEDS IN FLOOD EMERGENCIES 23

Survey Design 23
Survey Sampling 24
Survey Data 24
Survey Results Analysis 24
Demographic of Respondents 24
Respondents' Flood Experience 27
Information Used by Respondents 28
Information Desired by Respondents 29
Community Engagement 29
Summary and Conclusions 31

CHAPTER IV COMPUTER VISION FOR FLOOD DEPTH ESTIMATION IN URBAN ENVIRONMNETS 33

Flood Depth Estimation Using Street Photos 34
Computer Vision Model I: Image Processing and Convolutional Neural Networks 37
Convolutional Neural Networks for Stop Sign Detection in Photos 37
Image Processing for Pole Detection in Photos 39
Data Description 46
Results and Analysis 49
Pole Tilt Correction 53
Floodwater Depth Estimation 55
Computer Vision Model II: Training Convolutional Neural Networks for Flood Depth Estimation 57
Object Detection Model for Pole Detection 57
Pre-trained model 58
Clustering The Training Set 59
Training the Model 60
Validating the Model 61
Tilt Correction 63
Model Performance 66
Flood Depth Estimation 67
Data Description 69
Results and Analysis 74
Benchmarking 80
Model Validation on a Case Study 83
Techniques to Overcome Other Challenging Cases 85
Designing an Evacuation Decision Support Platform Based on the Identified Needs 87
Summary and Conclusion 92

CHAPTER V HUMAN-CENTERED FLOOD MAPPING AND INTELLIGENT ROUTING THROUGH AUGMENTING FLOOD GAUGE DATA WITH CROWDSOURCED STREET PHOTOS 95

Route Optimization for Intelligent Wayfinding in Flood Events....96
Proposed Methodology for Using Enhanced Flood Depth Data for Risk-Informed Route Optimization....98
Routing Approach I: Flood Depth Mapping Using Stop Sign Data and Route Optimization Using A* Search Algorithm....98
Routing Approach II: Flood Depth Mapping Using Augmented Stop Sign Data with Flood Gauge Data and Route Optimization Using Dijkstra Routing Algorithm....104
Mobile Device Implementation for Ad-hoc Situation Awareness....111
Background....111
Using Convolutional Neural Networks for Stop Sign Detection....112
Using Google Street View to Obtain Pre-flood Imagery of a Test Photo....113
Mobile Device Implementation....114
Blupix Preflood Crowdsourcing Platform....117
The Connection Between Blupix App, Blupix Mobile App, and Blupix Preflood App....119

CHAPTER VI FLOOD RISK PERCEPTION ASSESSMENT USING VIRTUAL REALITY....121

Introduction....121
Risks Associated with Floodwater Depth....121
Flood Risk Perception....122
Disaster Risk Assessment Using Virtual Reality....124
Methodology....125
VR Environment....125
Participants....126
Procedure....127
Preliminary Results....130
Pre-survey Results....130
Post-survey Results....131
Distribution of Data in Different Groups....132
Difference Between Flood Depth Estimation Error Between Various Groups....133
Summary and Conclusions....137

CHAPTER VII CONCLUSION....140

Summary....140
Research Contributions....145
Technical Contributions....145
Societal Contributions....147
Practical Limitations and Future Work....152
Standardized Urban Landmarks as Flood Depth Sensing Stations....152
Data Augmentation Using Various Resources....152

Water Level Change and Flowing Water 153
Human-Technology Interaction 154
Citizen Science 155
The Effect of Drainage Systems on Flood Depth Mapping 156
Human Perception of Risk 157

REFERENCES 158

APPENDIX A 196

APPENDIX B 204

LIST OF FIGURES

Page

Figure I-1 Map of major flood events in the world (2001-2016) (Courtesy of Maptitude).....3

Figure I-2 Map of flood events from January to July in 2021 (Courtesy of FloodList). ...3

Figure I-3 The study roadmap.....13

Figure II-1 FEMA flood map showing all water (normal and flooding) on August 29th, 2017 (during Hurricane Harvey) in Houston, Texas (Courtesy of Federal Emergency Management Agency). 15

Figure II-2 USGS flood gauges in the United States (Courtesy of National Water Information System, USGS).....17

Figure II-3 Comparison of the number of USGS flood gauges in different cities in Texas (Courtesy of National Water Information System, USGS).....17

Figure II-4 USGS flood gauges in San Francisco, California.....18

Figure II-5 Maximum observed flooding from satellite observatory in Houston, Texas during Hurricane Harvey (28th August-8 September 2017) (Courtesy of Dartmouth Flood Observatory).....22

Figure III-1 Distribution of respondents in Texas based on TWDB flood planning regions (Base map courtesy of Texas Water Development Board).....26

Figure III-2 Meeting with students and community partner from Port Arthur, Texas.....30

Figure IV-1 Paired pre- and post-flood photos showing the same stop sign in a residential neighborhood. 37

Figure IV-2 Overall architecture of the Mask R-CNN implementation in this research. 39

Figure IV-3 Canny edge detection process applied to a sample flood image. 42

Figure IV-4 Determining the intersection point of the sign and pole from the stop sign bounding box 45

Figure IV-5 Confining the line detection solution space along horizontal axis. 45

Figure IV-6 Approximating the stop sign pole from multiple close line candidates. 46

Figure IV-7 Ground-truth information in (a) a pre-flood photo, and (b) its post-flood paired photo. 49

Figure IV-8 Three different directions for rotation. 54

Figure IV-9 Title angle detection using template stop signs. 54

Figure IV-10 Examples of floodwater depth estimation for paired pre- and post-flood photos. 56

Figure IV-11 The architecture of the YOLOv4 network adopted in this research. 58

Figure IV-12 *(a)* Nine clusters (k = 9) corresponding to the training set, and (b) Recalculated anchor boxes for the in-house dataset 60

Figure IV-13 Adjusting flood depth estimation for pre-flood and post-flood stop signs with unequal degrees of tilt. 64

Figure IV-14 Tilt detection approach (base photo is courtesy of KjzPhotos/Shutterstock). 65

Figure IV-15 Workflow for estimating flood depth in a sample paired pre- and post-flood photos (base post-flood photo is courtesy of Erich Schlegel/Getty Image). 68

Figure IV-16 Photos of various stop signs in different forms and languages available from the Microsoft COCO dataset. 72

Figure IV-17 Sample annotated (a) pre-flood photo, and (b) post-flood photo (base photo in (b) is courtesy of Erich Schlegel/Getty Images). 73

Figure IV-18 Map of 11 test data related to the 2021 Pacific Northwest flood (numbers refer to IDs shown in Table IV-12). 84

Figure IV-19 Demonstration of challenging cases in post-flood photos: (a) multiple detections (base photo courtesy of Steve Zumwalt/FEMA), and (b) reflection in water (base photo courtesy of TSGT Mike Moore, USAF). 86

Figure IV-20 The graphical user interface of the Blupix crowdsourcing application. 88

Figure IV-21 The Model View Controller (MVC) framework of the Blupix crowdsourcing application. 89

Figure IV-22 Illustration of the system architecture of the Blupix crowdsourcing application. 90

Figure IV-23 Uploading and pairing crowdsourced photos on the Blupix app. 92

Figure V-1 Pseudo algorithm for A* Search. 101

Figure V-2 sample output of A* Search algorithm with obstacles. 101

Figure V-3 locations of selected paired flood photos in Houston, TX after Hurricane Harvey (2017). 102

Figure V-4 Illustration of the routing algorithm using buffered points that represent estimate floodwater depths collected from inundated areas. 104

Figure V-5 Location of start and end points (black pins), flood gauges (green squares), and stop sign points (red circles) in the experiment area. 108

Figure V-6 Flood mapping and risk-informed evacuation route optimization using EBK and Dijkstra algorithms: (a) regular route planning with Dijkstra algorithm; (b) EBK method with Dijkstra algorithm using only flood gauge data; (c) EBK method with Dijkstra algorithm using flood gauge data and stop sign data. 109

Figure V-7 Schematic representation of the Blupix app. 116

Figure V-8 Sample flood depth estimation on the Blupix app. 117

Figure V-9 The interface of the Blupix Preflood crowdsourcing application. 118

Figure V-10 The relationship and information flow between the Blupix app, Blupix Mobile app, and Blupix Preflood app. 120

Figure VI-1 The simulated town in Unity. 125

Figure VI-2 Virtual reality headset (Oculus) and controllers. 126

Figure VI-3 First-person view of the VR environment using the VR headset. 126

Figure VI-4 Virtual reality experiments in the user studies. 129

Figure VII-1 Screenshots of KHOU (CBS Houston) news segment covering the Blupix app (August 2020) (KHOU 11, 2020). 149

Figure VII-2 Community meetings with students from Port Arthur, Texas, who carried out tabletop experiments using the Blupix app to estimate floodwater depth (March 2022). 150

Figure VII-3 Community data collection in Port Arthur, Texas (November 2022). 151

LIST OF TABLES

Page

Table III-1 The distribution of income level among respondents. 27

Table III-2 Number of flood events experienced by respondents. 28

Table IV-1 Number of paired flood photos in BluPix v.2020.1 dataset in each FEMA region and Canada. 48

Table IV-2 Performance of stop sign detection in pre- and post-flood photos. 51

Table IV-3 Performance of pole detection in pre- and post-flood photos before tilt correction. 52

Table IV-4 Performance of pole detection in pre- and post-flood photos before tilt correction. 55

Table IV-5 The highest average performance of the trained model on five validation sets using 5-fold cross validation (S: Stop sign; P: sign pole; S+P: stop sign and sign pole). 63

Table IV-6 Overview of the training and test datasets. 70

Table IV-7 Performance of the trained model in detecting stop signs and poles in pre- and post-flood photos of the test set (S: Stop sign; P: sign pole; S+P: stop sign and sign pole). 75

Table IV-8 Performance of the trained model in estimating pole lengths in pre- and post-flood photos of the test before and after tilt correction. 77

Table IV-9 Performance of dummy methods I and II on the test set. 79

Table IV-10 The performance of the flood depth estimation model based on stop sign language. 80

Table IV-11 Comparison of the results of this study with the literature on floodwater depth estimation. 82

Table IV-12 Performance of the model on flood depth estimation. 85

Table V-1 Performance of floodwater depth estimation on paired pre- and post-flood photos. 103

Table V-2 Performance of the trained YOLOv4 model on 20 selected paired photos in Hurricane Harvey (August 27 – September 1, 2017) in Houston, Texas (S=stop sign; P=pole). 107

Table V-3 Comparison of three routing scenarios in the experiment area.....110

Table VI-1 Results of the post-survey on a 5-point Likert scale.....131

Table VI-2 Pearson correlations.....133

Table VI-3 Results of identifying significant difference between flood depth estimation errors with respect to variables. 136

CHAPTER I [1]

INTRODUCTION

Flood: The Most Prevalent Natural Hazard

Historical Perspective of Floods

Flooding is the most frequent weather threat and costliest natural hazard in the world (Mizutori & Guha-Sapir, 2018). The United States National Flood Insurance Program (NFIP) estimates the cumulative damage cost of floods to be over $1.75 trillion since 1980 (Smith, 2020b). Over the past two decades, there have been close to 5,000 flood events in the U.S. alone, leading to approximately 2,000 deaths (American Climate, 2019). Flooding can happen as a result of excess rainfall, tropical depressions or storms, hurricanes, or typhoons (Texas General Land Office, 2021). Between 1851 and 2019, the continental U.S. has experienced around 310 hurricane landfalls, averaging to almost 2 hurricanes per year (Texas General Land Office, 2021), including major hurricanes such as Harvey in 2017 which brought unprecedented rainfall and windstorms, and flooded more than

[1] Some of the materials presented in this chapter have been previously appeared in the following publications by the author:
Kharazi, B. A., Behzadan, A. H. (2021). Flood depth mapping in street photos with image processing and deep neural networks. Computers, Environment and Urban Systems, 88, 101628. https://doi.org/10.1016/j.compenvurbsys.2021.101628.
Alizadeh, B., Behzadan, A. H. (2022). Crowdsourced-based deep convolutional networks for urban flood depth mapping. 2022 European Conference on Computing ion Construction https://doi.org/10.48550/arXiv.2209.09200.
Alizadeh, B., Behzadan, A. H. (In Press) Scalable flood inundation mapping using deep convolutional networks and traffic signage. Computational Urban Science. (Accepted on 03/12/2023) https://doi.org/10.1007/s43762-023-00090-1.
Alizadeh, B., Li, D., Hillin, J., Meyer, M. A., Thompson, Courtney M., Zhang, Z., and Behzadan, A. H. (2022). Human-centered flood mapping and intelligent routing through augmenting flood gauge data with crowdsourced street photos. Advanced Engineering Informatics 54 (2022): 101730. https://doi.org/10.1016/j.aei.2022.101730

150,000 homes, 46% of which were outside the 500-year floodplain zones of the Federal Emergency Management Agency (FEMA) (Galloway et al., 2018). Figure I-1 demonstrates areas affected by large flood events in the world from 2001 to 2016. More recently, more frequent patterns of flooding were observed around the globe. Figure I-2 shows the distribution of flood events in the world from January 2016 to July in 2021. As an example of more recent floods, a major rainfall event spurred a series of floods in northern parts of the U.S. state of Washington and southern parts of the Canadian province of British Columbia in November 2021. In British Colombia, this flood caused record-breaking insured damage of $450 million (Insurance Bureau of Canada, 2021). In Germany, severe flooding resulted in $40 billion of economic loss in 2021. The 2021 flooding in Belgium was the worst flooding over the past 100 years with estimated damage of $3 billion approximately (Rodriguez Castro et al., 2022). In central China, the July 2021 flooding killed almost 100 people and resulted in more than $11 billion economic losses (T. Wang, 2021). In Europe, more than 200 million people live in coastal regions (within 50 km from coastal lines) (Vousdoukas et al., 2020). Among European countries, the Netherlands has the highest relative population (58%) living in flood-prone areas (Rentschler & Salhab, 2020).

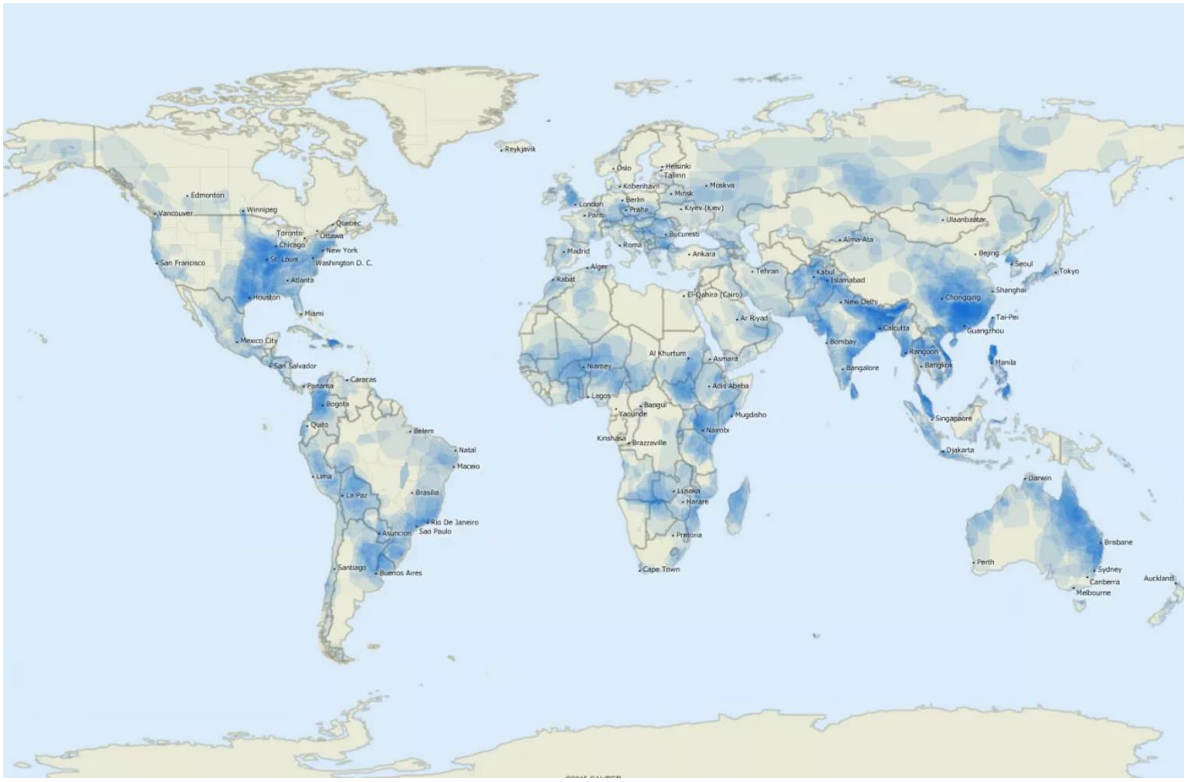

Figure I-1 Map of major flood events in the world (2001-2016) (Courtesy of Maptitude).

Figure I-2 Map of flood events from January to July in 2021 (Courtesy of FloodList).

Current Patterns and Future Outlook of Floods

In the U.S., there has been, on average, 16.2 weather and climate disasters annually between 2015 to 2020 (Smith, 2020a), and nearly one-third of people who live in coastal areas are exposed to elevated coastal hazard risks (United States Census Bureau, 2019). However, in 2021 alone, 223 flood events occurred which surpasses the reported annual average. Asymmetric urbanization, growing coastal population, climate change, and deforestation are the main drivers of increased flooding worldwide (Alizadeh et al., 2021; Bjorvatn, 2000; Sahin & Hall, 1996), and are expected to contribute to a tenfold increase in the annual flood loss over the next several decades, from $6 billion in 2005 to $60 billion by 2050 (Arnell & Lloyd-Hughes, 2014; Mills, 2005). Currently, more than one billion people around the world live in areas just 10 meters above high tide lines, which may be inundated in the near future due to changes in the hydrological cycle (Kulp & Strauss, 2019). According to a recent study, by the year 2100, the amount of land in the U.S. that is vulnerable to a 100-year flood event may increase by 45% in riverine floodplains, and 55% in coastal floodplains with fixed shorelines (e.g., stabilized through beach nourishment and other activities) (AECOM, 2013). As sea levels rise (Church & White, 2011), many communities, especially those in coastal areas, will experience growing risks and differential vulnerability to floods and storm water surge (Alfieri et al., 2017; Ford et al., 2019; Hauer et al., 2016; Rachel, 2013).

A study by Forizeri et al. (2017) also showed that weather-related natural hazards could affect about two-thirds of the Europe's population annually over the next century (Forzieri et al., 2017). Huang et al. (2015) investigated the combination of different climate

scenarios in the five large basins in Germany, and showed that most rivers in the study area could experience more 50-year floods (S. Huang et al., 2015). In Europe, strong mitigation incentives are expected to lead to a double increase in the average risk-based flood insurance premium between 2015 to 2050 (Hudson et al., 2019). Research also indicates that by 2100, at least 190 million people globally will experience flooding for the first time (Kulp & Strauss, 2019).

Flood Management and Response by Rescue Operators

In the aftermath of large-scale natural hazard events such as floods and hurricanes, having access to timely and accurate information is key not only to successful response and recovery (Gebrehiwot et al., 2019; Pi et al., 2020a), but also to mitigation, which aims to protect the health and safety of people, and limit damage to property or the environment (Federal Emergency Management Agency, 2016; Public Safety Canada, 2010). When a disaster strikes, a wide range of rescue groups with various levels of competence and resources attempt to organize themselves quickly and distribute available resources to perform crucial activities (Altay, 20085; Eller et al., 2015). Disaster response actors include government agencies, nongovernmental organizations (NGOs), private sectors, and volunteer residents (Chikoto et al., 2013; Cvetkovic & Martinović, 2020). First responders and emergency managers deployed from different jurisdictions to a disaster-affected area mainly follow their own command structure, abide by different standard operational procedures, and more importantly, use various communication and data exchange platforms which may not be compatible with one another or accessible to all participating teams (Texas General Land Office, 2021).

Different countries have different disaster management systems, such as the National Incident Management System (NIMS) in the U.S. (Annelli, 2006), the Australasian Inter-service Incident Management System (AIIMS), the Coordinated Incident Management System (CIMS) in New Zealand (Dwyer & Owen, 2009), and the Joint Emergency Services Interoperability Program (JESIP) in the UK (Flanagan, 2014). These systems serve as a disaster collaboration model between different agencies and guide approaches for federal, state, and local governments to prepare, respond to and recover from disasters. However, rescue operators still need real-time and accurate information about local conditions during disasters since different groups of people have different needs that must be considered in rescue mission decision-making. Geographic Information Systems (GIS) is one of the most common tools used to identify risk areas and available resources in order to support disaster response. Yet, GIS-based approaches do not provide knowledge-sharing and communication support among decision-makers (W. Zhang et al., 2018). Therefore, cyberinfrastructure is needed for sharing data and knowledge in addition to geospatial visualization tools to provide integrated and unified information to be utilized by different decision-makers.

Access to Information in Flood Evacuation

During flood events, beside the missions of rescue operators, ordinary people try to utilize the information distributed by various sources to determine their best course of action (e.g., evacuate or shore up). Unfortunately, much of the information from the field remains unseen by ordinary people who are the most affected, leading them to seek help through other channels, thus quickly overwhelming the telecommunication network. For instance,

during Hurricane Harvey, trapped people dialed non-emergency numbers such as 2-1-1 or 3-1-1 which only connected them to community services and information, or municipal government services (Texas General Land Office, 2021). Of the 19% world population at risk of substantial flooding, 89% live in low and middle-income communities with undeveloped or poorly developed disaster risk management practices (Rentschler & Salhab, 2020). However, the anticipated elevated risk of flooding in many parts of the world also necessitates innovative risk management approaches that can effectively navigate uncertainty, remove duplication, and utilize various publicly available resources and data (World Bank Group, 2021). A decentralized yet authenticated platform for collecting immediate multi-faceted data about the unfolding hazard event, and exchanging timely and accurate information with all stakeholders could potentially remedy this problem.

Flood Risk Perception

Due to various stakeholder groups, timely access to unified and reliable flood information is of the essence (Mai et al., 2020). Effective disaster management and response require clear communication with accurate information between citizens and rescue personnel. Also, effective and accurate communication depends on having effective and functional tools for sharing disaster-related information. Effective communication of flood risks helps raise public awareness and plays a critical role in increasing community resilience against natural hazards (Becker et al., 2008; Beggs, 2018; Brown et al., 2018; Buchecker et al., 2013; Fuchs et al., 2017; Nunn et al., 2014; Reser et al., 2012; Tyler & Sadiq, 2018). In this regard, having access to flood information and mitigation resources at multiple

levels (e.g., educational content and training programs offered by state and local governments, reports and evidence collected by rescue teams and emergency managers, documented stories and lived experiences of residents in flood-prone areas) can contribute significantly to improved risk perception and communication (Fitzpatrick-Lewis et al., 2010; Sansom et al., 2021). The means and the frequency by which people gather, access, process, and prioritize risk information influence how they make important decisions about sheltering, evacuation, and relocation during disasters (M. Lindell & Perry, 2004; Sansom et al., 2021). People's perceptions and expectations of disaster risks can also vary over time. For example, it was found that flood risk perception was significantly altered for some residents after being struck by severe flooding (Brown et al., 2018).

Traditionally, one-way risk communication from the authorities down to the public (i.e., experts informing residents of potential risks of natural hazards) has been used for alerting communities about flood risks. However, to promote trust in data and resulting policies and actions, recent research strongly favors two-way risk communication (Bennett et al., 2010; Bradbury, 1994), where members of the community actively participate in creating, sharing, and utilizing information about hazard risks, state of the environment affected by the hazard, and forthcoming decisions concerning sheltering, evacuation, and relocation (Alsnih & Stopher, 2004). Recently, various technologies have been used to develop disaster mitigation information systems. However, studies focusing on the technology acceptance model (TAM) in the context of disaster mitigation indicate that gaps still exist between the services provided by the system and the community's real needs (Siswanto et al., 2018; Thompson et al., 2006). For example, as discussed by Thompson et al.

(Thompson et al., 2006), the implementation of most of the currently available decision support systems such as CEMPS (designed by (Hernández & Serrano, 2001) for damage assessment) and ARTEMIS (designed by (de Silva & Eglese, 2000; Mishra et al., 2022) for floods) is limited. Integrating community input in technology design can be a potential solution to the lack of acceptance of and trust in flood mitigation and risk communication technologies (Mishra et al., 2022). Crowdsourcing the data collection, for instance, can promote data transparency, as well as technology usefulness at the time of a disaster (Kankanamge et al., 2019; Mehta et al., 2017; Song et al., 2020).

Research Context

Gaps in Knowledge and Practice

Disaster management and response are complex and challenging. Specifically, flood management and response currently face several limitations that affect their effectiveness. Some of the limitations are as follows:

- Traditional flood monitoring techniques have limitations in their spatial coverage. For instance, flood gauges and sensors are typically installed outside of residential areas, which result in incomplete flood monitoring especially in urban areas. In some regions, FEMA flood maps have not been updated for several years, which makes them unreliable and inadequate for flood risk assessment (AECOM, 2013). While light detection and ranging (LiDAR), Synthetic-aperture radar (SAR), and hydrological modeling techniques have the potential to improve flood depth mapping in urban areas, it is important to note that these methods are often associated with significant time and computational costs (Kwan & Ransberger,

2010). Additionally, proper data acquisition and processing are required to ensure accurate and reliable results (McDougall & Temple-Watts, 2012). Accurately mapping flood depths in urban areas is essential for effective flood management and response which highlight the need for a cost-effective, and high spatial resolution flood depth map.

- A high spatial resolution flood inundation map should be accompanied by an accurate and real-time route planning system for facilitating safe and effective evacuation of individuals during a flood event (Lu, 2006). The development of a safe route optimization systems enables individuals to make informed decisions about their evacuation plans and enable safe and efficient evacuation of all affected individuals, including those with mobility challenges.
- Real-time flood depth information is critical for individuals and first responders to make informed decisions and take appropriate measures during a flood event (Salmoral et al., 2020). However, currently this information is not readily available in all geographical regions, making it difficult for people to understand flood risk in their area (Salmoral et al., 2020). This lack of information can lead to delays in response, loss of property, and even loss of life.
- With the growing prevalence of social media and other digital platforms, critical and operationally relevant information is now commonly exchanged through these channels, enabling direct communication between citizens and emergency management organizations. Although few crowdsourcing applications have been developed for sharing disaster related information, they may not always adhere to

the standard process of information verification, challenging the ways in which both citizens and governments accept, process, and act on the information exchanged (Garcia-Molina et al., 2016). This presents a critical challenge to disaster management, which must balance the need for rapid response and action with the imperative of ensuring that the information upon which decisions are based is trustworthy and accurate. A concerted effort to overcome these challenges and leverage crowdsourced data could enhance the efficacy of flood management and response systems, resulting in improved preparedness and response during flood events.

- Different people have different perceptions of flood risk, and this perception can affect their level of exposure to such risk. In response, both local and national agencies are placing more emphasis on the role of risk perception to inform the development of new policies and technologies, as highlighted by Sjöberg in 2002. There is insufficient research on how individuals interpret and obtain flood risk in urban areas during evacuations. Findings of such studies can be used to inform the development of more effective flood management and response systems.

Dissertation Outline

This study first provides a background on current flood monitoring methods (Chapter II) with proposing a methodology as follow: First, a community needs assessment is conducted that highlighted the need for (near) real-time data on floodwater conditions, risk-informed evacuation plans, and safe and shortest transit routes (Chapter III). To address community's needs, a crowdsourcing application (called Blupix) was

subsequently developed to collect photos of traffic signs which are analyzed by computer vision models to estimate flood depth at the location of traffic signs. Then, to help people gain ad-hoc situation awareness, an intelligence wayfinding was implemented on generated flood depth map using crowdsource photos to determine the shortest flood-free evacuation route and a mobile device implementation of the decision support system (called Blupix Mobile) is designed to access real-time flood depth data and automate the data collection process (Chapter V). In the last Chapter, a user study is conducted to assess human's perception of flood risk during a flood evacuation (Chapter VI) (Figure I-3).

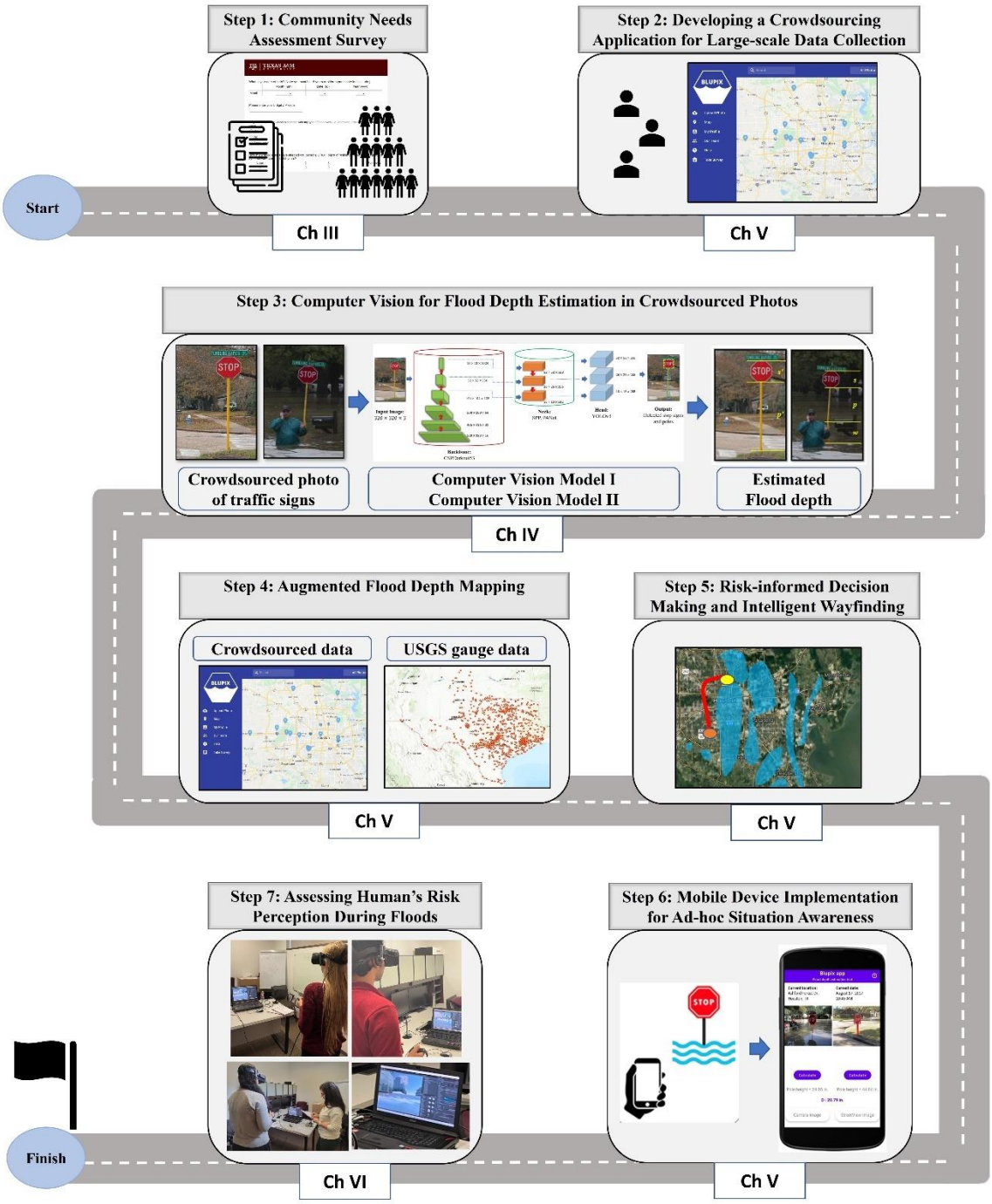

Figure I-3 The study roadmap.

CHAPTER II [2]

EXISTING FLOOD MONITORING AND DATA PROCESSING CAPACITIES

As discussed earlier, knowing the depth of floodwater in urban roads is critical to the success of response and recovery operations that follow. Traditional and advanced flood depth monitoring tools especially in urban areas have certain limitations which make them inefficient to provide highly granular and real-time flood depth data in urban roads. In this Chapter, most common flood depth measurement methods are presented with their advantages and disadvantages.

FEMA Flood Maps

Historically, the most common tool to inform communities about the local flood risk has been FEMA flood maps (Federal Emergency Management Agency, 2010). A sample FEMA flood map showing all water (normal and flooding) on August 29th, 2017 (during Hurricane Harvey) in Houston, Texas is presented in Figure II-1. In this figure, highlighted areas with blue color show the water extent after Hurricane Harvey and highlighted areas in yellow correspond to national flood hazard layer. A sample small area in near downtown area is enlarged in the figure to show the resolution of the flood map. Flood maps set minimum floodplain standards and serve as the basis for determining the cost of flood

[2] Some of the materials presented in this chapter have been previously appeared in the following publications by the author:
Alizadeh, B., Li, D., Hillin, J., Meyer, M. A., Thompson, Courtney M., Zhang, Z., and Behzadan, A. H. (2022). Human-centered flood mapping and intelligent routing through augmenting flood gauge data with crowdsourced street photos. Advanced Engineering Informatics 54 (2022): 101730. https://doi.org/10.1016/j.aei.2022.101730

insurance, which provides property owners with some level of financial protection (Federal Emergency Management Agency, 2010). However, approximately 75% of FEMA flood maps are older than 5 years, and 11% date back to the 1970s and 80s (First Street Foundation, 2019). A 2017 report by the U.S. Department of Homeland Security's Office of Inspector General found that only 42% of the total flood map miles in FEMA's inventory were updated and valid, falling short of FEMA's internal performance goal of 80% (Department of Homeland Security, 2017). At present, many parts of the U.S. do not have flood maps or have maps that are 15-30 years old (First Street Foundation, 2019).

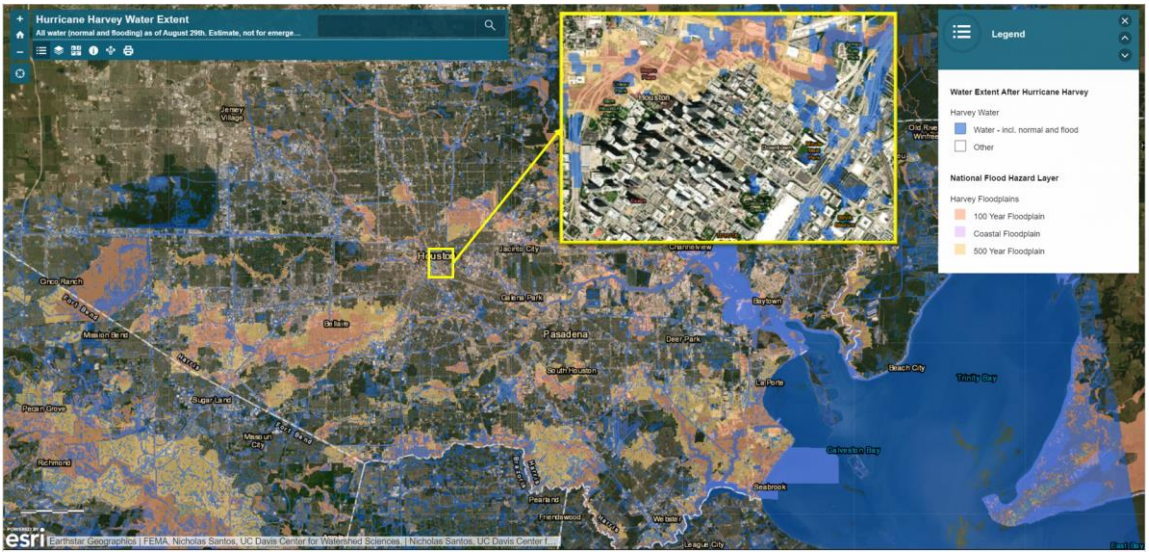

Figure II-1 FEMA flood map showing all water (normal and flooding) on August 29th, 2017 (during Hurricane Harvey) in Houston, Texas (Courtesy of Federal Emergency Management Agency).

Flood Gauges and Water Level Sensors

Conventional methods of flood depth calculation utilize data from water depth sensors or water wells in predefined locations. The United States Geological Survey (USGS), for example, operates a little more than 9,500 flood gages nationwide that transmit rainfall

amounts and/or stream levels (National Oceanic and Atmospheric Administration, 2022) (Figure II-2). However, these gauges are dispersedly distributed which result in insufficient data acquisition during floods in many regions (Z. Li et al., 2018). For example, Figure II-3 demonstrates a comparison between the number of USGS flood gauges in Houston, Austin, Dallas, Waco, San Antonio and College Station in Texas. As shown in this figure, while there are several of these gauges available in major cities (e.g., Houston, Austin and Dallas), there are few or none in small towns (e.g., Waco and College Station) which is determined as "data deserts" and has been also addressed in many studies (McCoy, 2017; Stahl et al., 2023). An example of data desert in major cities is demonstrated in Figure II-4, which shows that no USGS flood gauge is installed in San Francisco, California. Other than USGS based flood maps, researchers have also used hydrostatic pressure, mechanical float systems, thermal conductivity, and radiation-based water level measurement methods (Chetpattananondh et al., 2014). Previous work has attempted to predict flooding by detecting the rise or fall of water levels by comparing sensor readings with predefined thresholds (Chetpattananondh et al., 2014; Odli et al., 2016; Töyrä et al., 2002). These sensors, however, have limited coverage area (primarily in and around riverine or coastal lands), can be washed away in heavy rain, and need major effort for installation, calibration, and maintenance in flood susceptible locations.

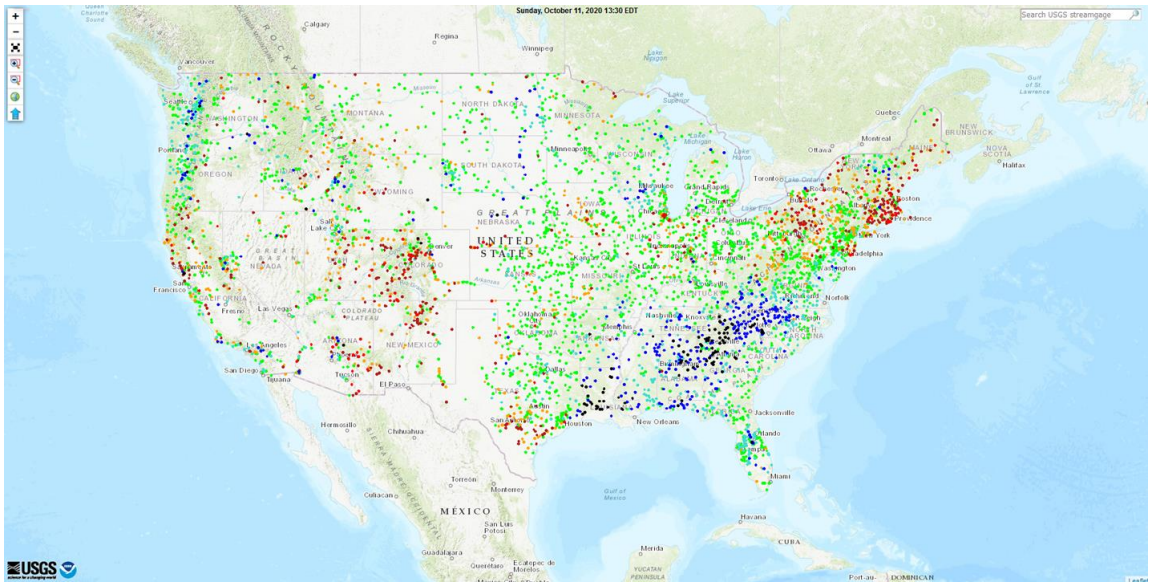

Figure II-2 USGS flood gauges in the United States (Courtesy of National Water Information System, USGS).

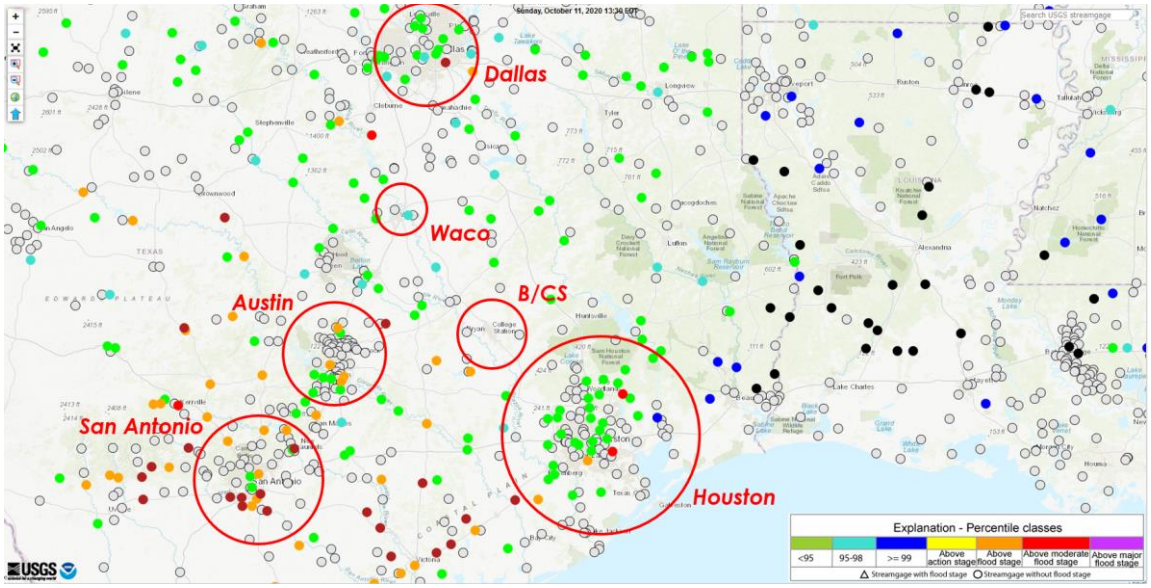

Figure II-3 Comparison of the number of USGS flood gauges in different cities in Texas (Courtesy of National Water Information System, USGS).

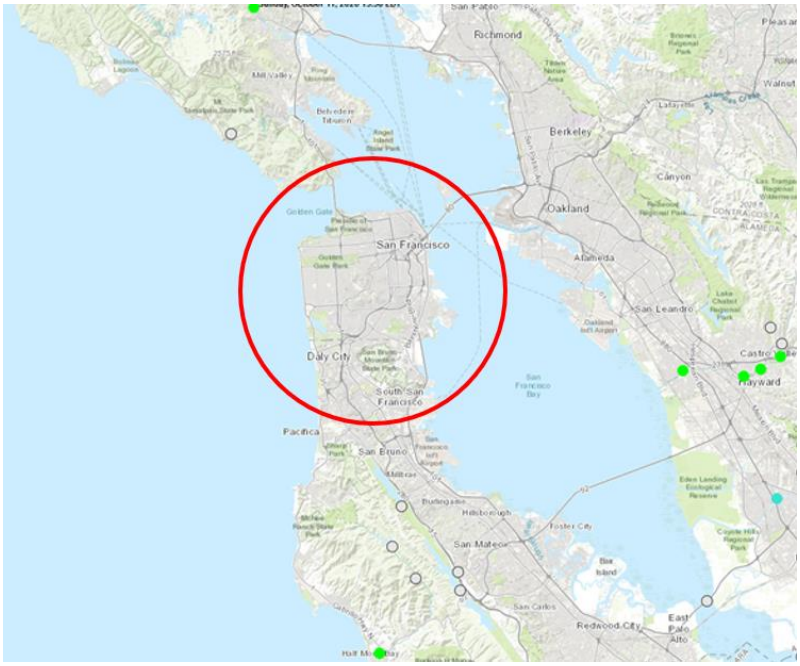

Figure II-4 USGS flood gauges in San Francisco, California.

Advanced Flood Mapping Tools

Researchers have also used computer models to estimate flood depth and flow characteristics. However, surface variability and inconsistency coupled with the difficulty in differentiating saturated surface soil and standing water in aerial images makes it difficult for these models to achieve accurate results especially in urban areas (Salmonsson, 2015; United States Geological Survey, 2019). Additionally, most existing global digital elevation models (DEMs) used for flood mapping are dated and insensitive to reshaped surface topography, and acquisitions are not routinely repeated (Hawker et al., 2018). DEMs tend to result in large vertical errors especially over complex topography (e.g., urban areas), exhibit little microtopographic variations in relatively flat terrain, and suffer from vegetation bias (Baugh et al., 2013; O'Loughlin et al., 2016), rendering them

unreliable for resolving key terrain features that control flood characteristics (Schumann, 2014). In a study that assessed several large-scale DEMs for hydrologic runoff prediction, it was concluded that different DEMs can lead to almost 10% in runoff prediction error (Kenward, 2000). In developing Floodwater Depth Estimation Tool (FwDET), based solely on an inundation map with an associated DEM, researchers reported an average difference of 18 cm and 31 cm for selected coastal (using a 1-m DEM) and riverine (using a 10-m DEM) areas compared to physically-based hydrodynamic simulations (Cohen et al., 2019). In some cases, even high-accuracy DEMs from aerial photogrammetry may be significantly different from ground-truth, especially when looking at smaller catchments or applications for which localized elevation errors can be detrimental to local scale applications (Walker & Willgoose, 1999).

Computer Vision for Flood Depth Estimation

More recently, advancements in artificial intelligence (AI) for object detection have led to new opportunities for remotely estimating water level depth using computer vision algorithms. Yang et al. (2014), for instance, used visual recognition to read water levels from a video camera set up alongside a river embankment in order to predict flood due to rising water levels. They utilized Laplacian method (Vincent & Folorunso, 2009) for detecting the edges of different objects and probabilistic Hough transform (Z. Zhu & Brilakis, 2009) for detecting the straight waterline. Testing this method on an indoor water channel and in simulated rainfall resulted in less than 1.2% and 2.5% in average absolute error, respectively. Dong et al. (2020) simulated the failure cascade process and flood control network vulnerability with a Bayesian method based on the topological structure

of the flood control network (Dong et al., 2020). Pan et al. (2018) calculated water level by remotely monitoring the length of a measuring ruler (in pixels) in footage obtained from a video camera installed next to a river, and found that convolutional neural networks (CNNs) outperformed traditional image processing algorithms with an average error of 9 mm and a standard deviation of 6.69 mm (Pan et al., 2018). Park et al. (2021) estimated the depth of flood through detecting submerged vehicles in flood photos using Mask R-CNN (K. He et al., 2017b), and comparing them with the most similar 3D rendered objects based on feature maps extracted by VGGNets (Simonyan & Zisserman, 2014)(Park et al., 2021). Using features extracted from the 4th pooling layer of VGG16, they achieved mean absolute error (MAE) values as lows as 6.49 cm. Other than cameras, drone and satellite imagery have been used for detecting floods using visual information. For example, in a study by Gebrehiwot et al. (2019), flooded areas were found from videos captured by a drone using four object detection methods based on different variations of fully convolutional networks (FCN-16, FCN-18, and FCN-32) (Long et al., 2015a) and support vector machines (SVM) (Cortes & Vapnik, 1995) with an accuracy of 95%, 95.52%, 92% and 87.45%, respectively (Gebrehiwot et al., 2019). Pi et al. (2020) trained a CNN model on VOC dataset (Everingham et al., 2010) to detect flooded areas with a mean average precision (mAP) of 80.69% in aerial videos (Pi et al., 2020a).

Remote Sensing

Besides the high cost of sensor installation and operation for real time data acquisition, a key challenge in floodwater depth analysis especially in urban settings is the lack of granularity of flood information in comparison with roads and neighborhood data, which

makes it extremely difficult to contextualize the relationship between the road network and flooded areas (Federal Emergency Management Agency, 2016). Recently, LiDAR (Kwan & Ransberger, 2010; McDougall & Temple-Watts, 2012), structure from motion (SfM) (Meesuk et al., 2017), and the U.S. Geological Survey (USGS) National Water Information System (United States Geological Survey, 2019) have been used to map flood events and determine the flow path to estimate floodwater depth, albeit their application is limited to places that are fully visible from air and not obscured by vegetation or bridges (United States Geological Survey, 2019). At present, precise measurement of water depth (i.e., with centimeter-level accuracy) from aerial views is mostly done with highly sophisticated instruments and expensive computations that are not readily available for large-scale adoption (United States Geological Survey, 2019). An example of generated flood maps of Hurricane Harvey in Houston, Texas between August 28th and September 8th in 2017 using satellite observatory method is presented in Figure II-5. In this figure, blue is the reference normal water extent and red is the maximum observed flooding from satellites observatory method (using data from the satellites of NASA MODIS, ESA Sentinel 1, ASI Cosmo SkyMed, and Radarsat 2). Also, light gray in the figure corresponds to all previously mapped floods.

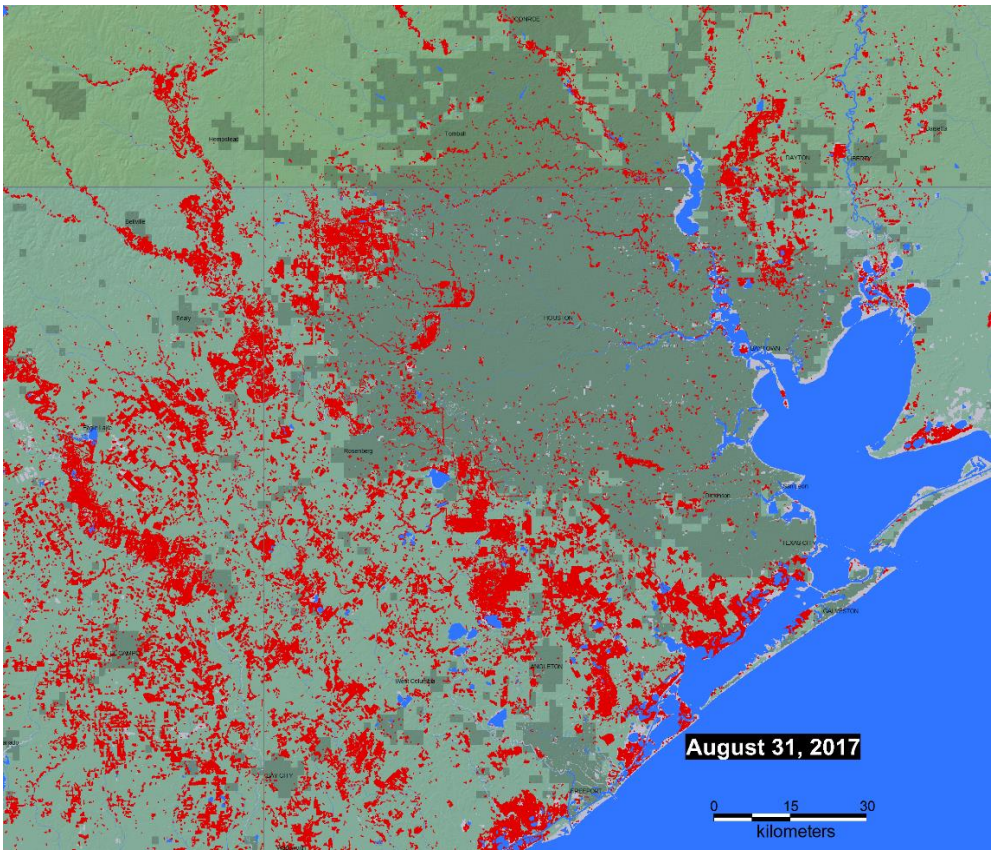

Figure II-5 Maximum observed flooding from satellite observatory in Houston, Texas during Hurricane Harvey (28th August-8 September 2017) (Courtesy of Dartmouth Flood Observatory).

CHAPTER III [3]

DATA NEEDS IN FLOOD EMERGENCIES

In this research, a survey was designed to identify information characteristics demanded by rescue operators and regular citizens for rescue missions and evacuation processes. The goal of this survey was to enable the incorporation of local knowledge and decision-making needs at the public citizen and rescue operator level into designing a spatial decision support system (SDSS) for flood events.

Survey Design

The focus groups of the survey were public citizens and rescue operators. Both regular citizens and first responders were asked questions about their flood experiences in the past, whether they have ever needed rescue assistance during flooding events, and what information they would like to have to help them evacuate. Also, first responders were asked questions about their challenges during rescue operations, the information they needed, and the information they wished they had to get to people in need. Thirteen questions were designed as multiple-choice, select all that apply, and short answers. The online version of the survey was implemented using Qualtrics. The survey and the related consent materials were approved by the Institutional Review Board (IRB2019-1506D). All survey questions along with their multiple choices are presented in Appendix A.

---

[3] Some of the materials presented in this chapter have been previously appeared in the following publications by the author:
Hillin, J., Kharazi, B. A., Li, D., Thompson, C. M., Meyer, M., Zhang, Z., & Behzadan, A. H. (In Press) Designing user-centered decision support systems for climate disasters: What information do communities and rescue responders need during floods? Journal of Emergency Management. (Accepted 9/7/2022).

Survey Sampling

The survey was conducted using the convenience sampling method. The survey link was distributed through email listservs and social media accounts of community partners (e.g., Hazard Reduction and Recovery Center (HRRC), Texas Target Communities (TTC), and disaster relief NGOs of Cajun Navy Relief and Crowdsource Rescue). Additionally, surveys were distributed to participants in community meetings, research presentations, and through community partners' outreach networks and campuswide university emailing lists.

Survey Data

Survey responses were first cleaned by dismissing incomplete responses or those that refused consent. Among 13 questions, 4 short answers were determined as the focus of the analysis. Responses for each of the four questions were then imported as distinct projects into Atlas.ti (version 9) and then analyzed using the descriptive coding method (Saldaña, 2021). The type of information (evacuation; built environment) and information characteristics (real-time, accuracy) needed were specified in the pattern coding.

Survey Results Analysis

Demographic of Respondents

A total number of 218 responses were collected through the Qualtrics survey. The first response was submitted on April 30, 2020 and the last response was submitted on Feb 11, 2021. Out of 218 responses, 118 responses were female, 94 were male, 1 non-binary and 5 did not wish to answer. Respondents were 73.73% White or Caucasian, 10.14% Hispanic, 5.53% Asian, 1.84% Black or African American, and 8.76% had other ethnicity

or multi-ethnicities. At the end of the survey, the youngest responder was 21 years old and the oldest was 80 years old. A 50% of respondents (majority) aged between 20 to 40 years (1983-2003) years old, 28.44% respondents aged between 40 to 60 years old (1963-1983), and 20.62% respondents aged between 60 to 80 years old (1943-1963), and finally 0.92% respondents aged more than 80 years old (1937-1943). From all who responded to the survey, 212 (97.25% of respondents) were based in Texas, with 2 responses from New York, 1 from North Carolina, 1 from Georgia, 1 from Ohio, and 1 from Colorado. Figure III-1 presents the distribution of the 212 Texas-based participants in each region of the State based on the flood planning regions specified by The Texas Water Development Board (TWDB) (The Texas Water Development Board, 2020). As this Figure shows, the majority of the participants resides in region 6 – San Jacinto (in/near Houston, $N = 107$) and region 8 – Lower Brazos (in/near College Station and Bryan, $N = 73$). The income level for the 218 respondents is presented in Table III-1. This Table shows that 30 respondents were first responders (based on their answers to the questions related to flood rescue experience) and the rest were ordinary people. Among all respondents, only one person did not have mobile device. Based on responses, 33.49% had an Android device, 62.33% had an iPhone device, and 4.19% had both Android and iPhone devices. Only 3.72% of respondents had no access to mobile data (without Wi-Fi).

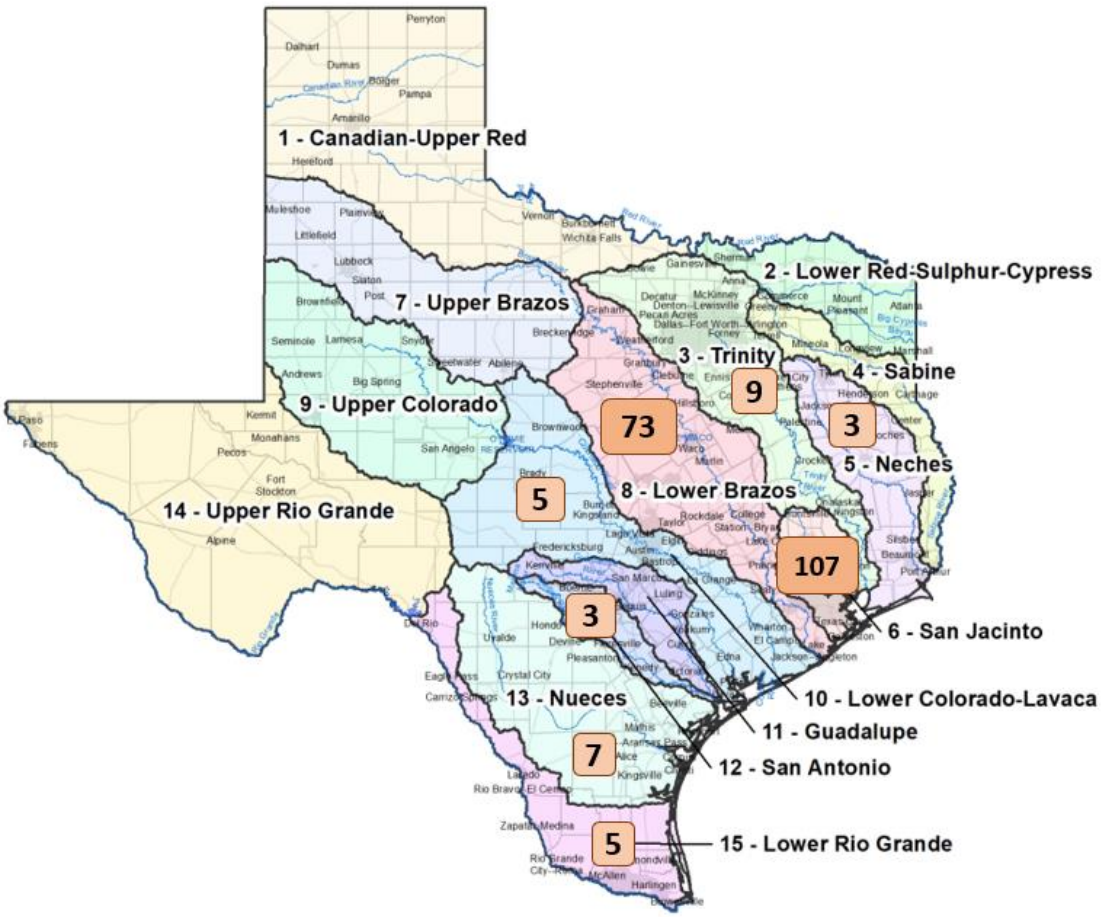

Figure III-1 Distribution of respondents in Texas based on TWDB flood planning regions (Base map courtesy of Texas Water Development Board).

Table III-1 The distribution of income level among respondents.

Income Level	Percentage of Respondents (*N* = 218)
Below $14,000	3.21%
$14,001 … $31,000	8.26%
$31,001 … $63,000	15.63%
$63,001 … $113,000	23.85%
$113,001… $184,000	16.51%
$184,001 … $248,000	8.72%
$248,001 … $475,000	7.34%
Above $475,000	1.38%
Did not wish to answer	15.14%

Respondents' Flood Experience

Out of 218 responses, 32 people stated that they had no first-hand experience with floods, and 184 people declared that they had first-hand experience with floods, and 2 people did not know. Two respondents (which were based in Texas) reported that they do not know if they had first experience with floods. All respondents from states other than Texas had first-hand experience with floods. Respondents were asked to provide the number of flood events they had experienced (0-5 or more). Table III-2 demonstrates the distribution of responses based on the number of flood experiences. Out of 218 responses, only 160 people answered the question related to evacuation experience, in which 35% indicated

that they evacuated). Out of 30 rescue operators, 73.33% declared that they had challenges in estimating the depth of floodwater in roads during rescue operations.

Table III-2 Number of flood events experienced by respondents.

Number of Flood Event	Percentage of Respondents (*N* = 218)
0	26.73%
1	19.82%
2	18.89%
3	13.36%
4	6.91%
5 or more	14.29%

Information Used by Respondents

For regular citizens, the types of information used during a flood were organized into six themes (e.g., notification systems, physical conditions, government sources, online sources, social networks, and personal knowledge.) For rescue operators, the types of information used during a flood were organized into six themes (e.g., physical conditions, real-time information, evacuee information, emergency management organizations, local resources, and government sources. For regular citizens, the types of information used during a flood were organized into six themes (e.g., notification systems, physical conditions, government sources, online sources, social networks, and personal knowledge.)

Information Desired by Respondents

For rescue operators, the types of information used during a flood were organized into six themes (e.g., physical conditions, real-time information, evacuee information, emergency management organizations, local resources, and government sources.) For regular citizens, the types of information desired were organized into five broad categories: accurate information, advanced warning, evacuation destination/resources, evacuation process, and safety. The type of information desired by rescue operators was grouped into categories: rescue information, real-time information, evacuee information, physical conditions, and accurate information.

Community Engagement

The development of an effective system for flood response requires a thorough understanding of the community's needs and perspectives. To gain insight into the community's flood risk awareness and gather input on technology development, several community meetings were held in addition to the surveys. These meetings provided a platform for community members to share their concerns, experiences, and feedback on the potential system's design and functionality. During these meetings, the research team engaged with community leaders, local officials, and residents to discuss the current state of flood response in the area and explore potential solutions. A picture of a meeting with a community partner from Port Arthur, Texas is presented in Figure III-2. The team presented their developed tools and research findings and sought additional input from the attendees. The discussions focused on topics such as the accessibility and usability of the flood risk assessment tool, the types of information that should be included, and how the

tool could be integrated into the existing emergency response system. Through these community meetings, the research team was able to raise awareness about flood risk and its potential impacts on the community. The meetings also helped to foster a sense of collaboration and trust between the research team and the community, which is essential for the successful implementation of any technology or intervention. Overall, the community meetings were an essential component of this study, helping to ensure that the developed technology would meet the community's needs and be effective in improving flood response and management in the area.

Figure III-2 Meeting with students and community partner from Port Arthur, Texas.

Summary and Conclusions

Based on survey results, both regular citizens and first responders rely on information distributed by the government and physical conditions during flood events. However, the sources for getting this information varied between respondents. Based on the identified themes of the survey responses, citizens and first responders needed information on available local resources, evacuees, emergency management organizations, and real-time data. The survey results mainly highlighted a need for accurate, real-time data during flood events which differs from the general disaster information distributed by the government that takes hours to process. As an example, first responders are more in need of accurate information to perform rescues rather than having more data. This finding also complies with the study by Salmoral et al. (Salmoral et al., 2020) and Blum et al. (Blum et al., 2014), stating that rescue operators require accurate and real-time information.

On the other hand, responses from regular citizens demonstrated that they mostly rely on information from less formal channels or specifically designated for the public, such as existing notification systems, social networks, online sources, and personal knowledge. In fact, regular citizens tend to need more dependent and accessible communication from various sources. That can be the reason behind the increasing use of social media by regular citizens for information access. However, according to Mihunov et al. (Mihunov et al., 2020), disparities in social media make it more useful for populations less vulnerable to disaster impacts (e.g., well-education, employed, higher income, etc.), and not all people.

It should be noted that this is an ongoing survey, however, the responses received so far pointed out clearly to the direction that community and disaster management professional both looked for accurate, real-time flood depth information during flood events. In conclusion, the number of complete responses so far is sufficiently large for the purpose of this study although more responses are expected in the future.

CHAPTER IV [4]

COMPUTER VISION FOR FLOOD DEPTH ESTIMATION IN URBAN ENVIRONMNETS

In flood events, knowing the depth of floodwater is of critical importance to first responders, emergency managers, and ordinary people involved in search and rescue operations and community evacuation. This information, however, is not readily available or shared in many jurisdictions particularly in the immediate flood aftermath when it is most needed. Additionally, current flood mapping methods such as those relying on DEMs fail to capture reshaped surface topography and microtopographic variations in flat terrain especially in urban areas, leading to large vertical errors. New digital media capture and data exchange platforms coupled with advancements in ML, image processing, and computer vision for object detection have created new opportunities for remotely estimating water level depth in flooded areas. In this Chapter, a new approach to

[4] Some of the materials presented in this chapter have been previously appeared in the following publications by the author:
Kharazi, B. A., Behzadan, A. H. (2021). Flood depth mapping in street photos with image processing and deep neural networks. Computers, Environment and Urban Systems, 88, 101628. https://doi.org/10.1016/j.compenvurbsys.2021.101628.
Alizadeh, B., Behzadan, A. H. (2022). Crowdsourced-based deep convolutional networks for urban flood depth mapping. 2022 European Conference on Computing ion Construction https://doi.org/10.48550/arXiv.2209.09200.
Alizadeh, B., Behzadan, A. H. (2023). Scalable flood inundation mapping using deep convolutional networks and traffic signage. Computational Urban Science. (Accepted on 03/12/2023) https://doi.org/10.1007/s43762-023-00090-1.
Alizadeh, B., Li, D., Hillin, J., Meyer, M. A., Thompson, Courtney M., Zhang, Z., and Behzadan, A. H. (2022). Human-centered flood mapping and intelligent routing through augmenting flood gauge data with crowdsourced street photos. Advanced Engineering Informatics 54 (2022): 101730. https://doi.org/10.1016/j.aei.2022.101730

estimating floodwater depth in street photos using stop signs as measurement benchmark was introduced and validated. To estimate flood depth in street photos, two computer vision models (Computer Vision Model I and Computer Vision Model II) were developed and their performance were evaluated and compared with each other.

Flood Depth Estimation Using Street Photos

In this study, image processing technique and computer vision models are utilized to measure floodwater depth. The model input is a pair of pre- and post-flood street photos taken by ordinary handheld devices (e.g., smartphones, tablet computers, digital cameras), and the output is the depth of floodwater in the location where the photos were taken. While images can be taken from different angles and different distances from the water surface, to measure the depth of the flood, the model relies on the dimensions of a known benchmark visible in the image, for which the real size (e.g., in inches) is known. Image processing and computer vision are then used to determine the size of this benchmark in pixels and calculate a constant measurement ratio (e.g., inches to pixel), which in turn, is used to convert all other measurements from pixel to standard units (e.g., inches).

Past research has investigated the use of various objects for flood depth estimation. For instance, Barz et al. (2019) proposed an image retrieval approach with relevance feedback to find flood images on social media (Barz et al., 2018). Sazara et al. (2019) trained deep neural networks to recognize flooded roads in photos taken by mobile devices (Sazara et al., 2019). In another research, the size of submerged objects in water was used to estimate the depth of flood with an MAE of approximately 10 cm (Chaudhary et al., 2019). In contrast to past work that has used objects with arbitrary shapes and sizes as benchmarks,

to increase the practicality of this work in real world flood response operations, the visual benchmark selected in this research is ubiquitous (i.e., existing in many places), and have standardized shape and dimensions that are known to the model beforehand. In addition, to maximize scalability and increase technology adoption among users, the benchmark should be relatable, and easy to find and access. This last requirement is of particular importance when crowdsourcing is the main source of flood data collection, as past research has indicated that participants should be continuously kept motivated and engaged to complete delegated tasks with expected quality (Puttinaovarat & Horkaew, 2020; Sazara et al., 2019). Considering these factors, traffic signs are used in this study as standard visual benchmarks. Unlike sophisticated flood measurement sensors, traffic signs are omnipresent and easy to identify. In a study by Shinar et al., 78% of local traffic signs were perfectly identified by people (regardless of age or group) (Shinar et al., 2003). Stop signs, in particular, can be found in many intersections in urban and rural areas. Boeing (2018) used OpenStreetMap to analyze 27,000 U.S. street networks and counted approximately 50 intersections (~56% three-way and 27.5% four way) per 1 km2 of neighborhood-scale street network (Boeing, 2020). While the exact number of stop signs in the U.S. is a matter of debate, it is a fact that many intersections feature two-way or four-way stop signs to control traffic flow especially when there is high-speed traffic, restricted view, or pedestrian crossing (Federal Highway Administration, 2009). In many parts of the world, a stop sign is easily recognizable by its octagonal shape with standardized equal height and width. In the U.S., traffic sign shapes and dimensions are laid out in the Manual on Uniform Traffic Control Devices (MUTCD) and its companion

volume, Standard Highway Signs (SHS) (Federal Highway Administration, 2004). The size of a stop sign may slightly vary depending on the location it is installed; 30×30 inches in single-lane roads (almost all residential neighborhoods), and 36×36 inches in multi-lane conventional roads and expressways. While the shape and dimensions of the sign itself is standardized, the pole that holds it may or may not be regulated and can be made of different material and have different length.

As shown in Figure IV-1, the depth of floodwater, i.e., d_w, can be calculated as the difference between pole lengths in a pair of pre- and post-flood photos. In Figure IV-1(a), knowing the height of the sign octagon in both pixels (s) and in inches (30"), the constant ratio r is obtained as $30 \ / \ s$, indicating the number of inches corresponding to one pixel in the post-flood photo. Using this ratio, the length of the pole above waterline is calculated as $r \times p$, in which p is the pole length in pixels. Similarly, In Figure IV-1(b), knowing the height of the sign octagon in pixels (s') and inches (30", same as before), the constant ratio r' is obtained as $30 \ / \ s'$, indicating the number of inches corresponding to one pixel in the pre-flood photo. Using this ratio, the full length of the pole (with no floodwater) is calculated as $r' \times p'$, in which p' is the pole length in pixels. Note that ratios r and r' are not necessarily equal since the two photos could be taken at different angles and distances from the stop sign. The following Subsections describe how pixel dimensions s, p, s', and p' are extracted with image processing.

Figure IV-1 Paired pre- and post-flood photos showing the same stop sign in a residential neighborhood.

Computer Vision Model I: Image Processing and Convolutional Neural Networks

Convolutional Neural Networks for Stop Sign Detection in Photos

In the first part of this research, the first flood depth estimation model (Computer Vision Model I), e.g., a modified version of Mask R-CNN (K. He et al., 2017b), which uses RetinaNet (T. Y. Lin et al., 2017)for regression, classification, and mask estimation, is implemented based on Keras open-source library (Gulli & Pal, 2017)to detect and generate a mask (pixel boundaries) of the stop sign in the input image. Mask R-CNN is a deep neural network that is pre-trained on the COCO image dataset (containing 80 classes) for instance segmentation (T.-Y. Lin et al., 2014). For this research, any classes other than stop signs are filtered out during mask detection. As shown in Figure IV-2, the Mask R-CNN architecture internally combines two smaller networks, Faster R-CNN (Ren et al.,

2015) for detecting objects, and an FCN (T. Y. Lin et al., 2017)for understanding the image context. The loss function of Mask R-CNN is therefore the sum of the loss functions of these two networks.

Faster R-CNN utilizes region proposal network (RPN) (Ren et al., 2015)to generate region proposals, followed by a secondary network that uses these proposals to detect objects and draw bounding boxes. The output of the RPN consists of proposed regions with different sizes, leading to differently sized feature maps. Prior to classification and bounding box regression, these feature maps should be reduced to the same size. For this purpose, region of interest (RoI) pooling (Girshick et al., 2014)is used which splits the input feature map into a fixed number of roughly equal regions, followed by max pooling on every region. The final output of the Faster R-CNN is class labels (classification) and bounding boxes (localization). In order to generate object masks inside each bounding box, FCN decompresses the image to $1/32$ of its original size with blocks of convolution and max pooling layers to capture contextual and semantic information. Next, class prediction is made, and the image is rescaled to its original size with deconvolution layers and upsampling to return spatial information that were lost during downsampling. To minimize information loss, spatial data is transferred before downsampling with a skip connection (Long et al., 2015b). Figure IV-2 shows the overall architecture of the Mask-RCNN consisting of two internal networks and the flow of image processing through each part.

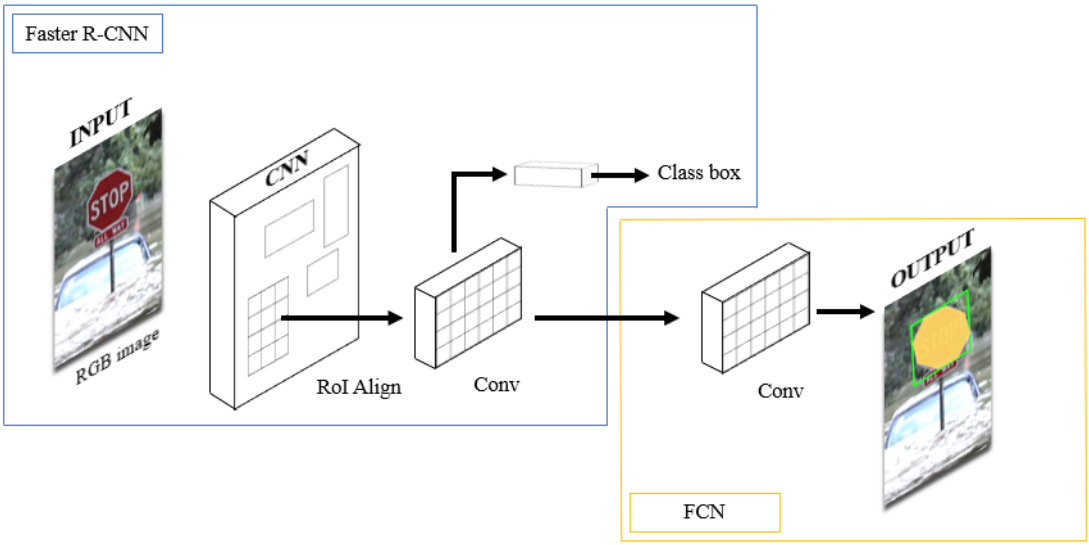

Figure IV-2 Overall architecture of the Mask R-CNN implementation in this research.

Image Processing for Pole Detection in Photos

Pole detection is performed in a two-step process using pre- or post-flood photos with generated stop sign masks from previous section. First, all edges in the grayscale input image are discovered using Canny edge detector (Liang, 2020), and next, probabilistic Hough transform for straight line detection is utilized to create a list of pole candidates by selecting edges that form lines. To implement Canny edge detector (R. Wang, 2013), images are first converted from the original red-green-blue (RGB) color space to grayscale using Equation IV-1, in which pix_c, pix_r, pix_g, and pix_b represent the grayscale, red, green, and blue values of each pixel, respectively.

$$pix_c = 0.3 \times pix_r + 0.59 \times pix_g + 0.11 \times pix_b \qquad \text{Equation IV-1}$$

The raw output of the Canny edge detector is an edge map which consists of all detected edges (regardless of angle and position) in the image. To reduce the noise in the image, a

5×5 Gaussian filter is used to replace the value of each pixel with the weighted average of its adjacent pixels. This eliminates false positives (FPs) and edges that are the least consequential (e.g., lines that appear too small, or are too far away). As shown in Equation IV-2, the 5×5 Gaussian filter is applied (through a convolution operation, *) to the input image Img_i to generate an output image Img_o with smoothened noise. Evidently, the size of the Gaussian filter can affect the outcome of edge detection. Generally, while a larger filter size lowers the sensitivity to noise, it may as well increase the localization error (Pedersini et al., 1997). However, previous work has shown that a 5×5 filter is suitable in most cases (Delgado, n.d.; Pei-Yung Hsiao et al., 2006).

$$Img_o = \frac{1}{159}\begin{bmatrix} 2 & 4 & 5 & 4 & 2 \\ 4 & 9 & 12 & 9 & 4 \\ 5 & 12 & 15 & 12 & 5 \\ 4 & 9 & 12 & 9 & 4 \\ 2 & 4 & 5 & 4 & 2 \end{bmatrix} * Img_i \qquad \text{Equation IV-2}$$

Next, the intensity gradient of each detected edge in Img_o is determined by a Sobel filter (Sobel, 1978) which returns a value for the first derivative in the horizontal direction (G_x) and vertical direction (G_y). Using these two values, the edge gradient (G) and direction (θ) are determined using Equations IV-3 and IV-4. The calculated gradient is always perpendicular to the edge.

$$G = \sqrt{{G_x}^2 + {G_y}^2} \qquad \text{Equation IV-3}$$

$$\theta = \tanh^{-1}\left(G_x / G_y\right) \qquad \text{Equation IV-4}$$

Following the gradient calculation, an edge thinning technique called non-maximum suppression is used to compare the edge strength of each pixel with that of the pixel in the

positive and negative gradient directions, and subsequently remove pixels that are not local maximums in the direction of the edge gradient (Rong et al., 2014). The output of this stage is a binary (i.e., grayscale) image of remaining edge pixels providing a more accurate representation of real edges in the image. This image is processed with hysteresis thresholding, a noise reduction step to determine if weak edge pixels (e.g., pixels detected as edges because of noise or color variation) should be kept or eliminated from the final image. The literature on Canny edge detector has proposed different values for minimum and maximum thresholds based on image type and application. Some have used fixed values of 100 and 300 for lower and upper thresholds, respectively (OpenCV Dev Team, 2019; R. Wang, 2013). Alternatively, threshold values can be determined based on the pixel values of an image (Farras A. W., 2020; Liang, 2020). More advanced methods involve automated Canny edge thresholding using a Gaussian Kernel, and fuzzy logic-based threshold selection (Incetas et al., 2019; Powers, 2011; Tanyeri et al., 2019). Considering the content and diversity of flood photos used in this study, upper and lower thresholds for edge detection are constructed based on percentages of the median of pixel intensities in the image. Minimum and maximum threshold values serve as the basis to determine whether a pixel belongs to an edge (if its intensity gradient is more than the upper threshold) or must be discarded (if its intensity gradient is less than the lower threshold). A pixel with an intensity gradient between the lower and upper thresholds is assessed in the context of its neighboring connections; if it is connected to a strong edge pixel, it will be kept as part of that edge, and otherwise it will be marked as a non-edge

pixel. Figure IV-3 shows the steps of the Canny edge detection process applied to a sample flooded stop sign image.

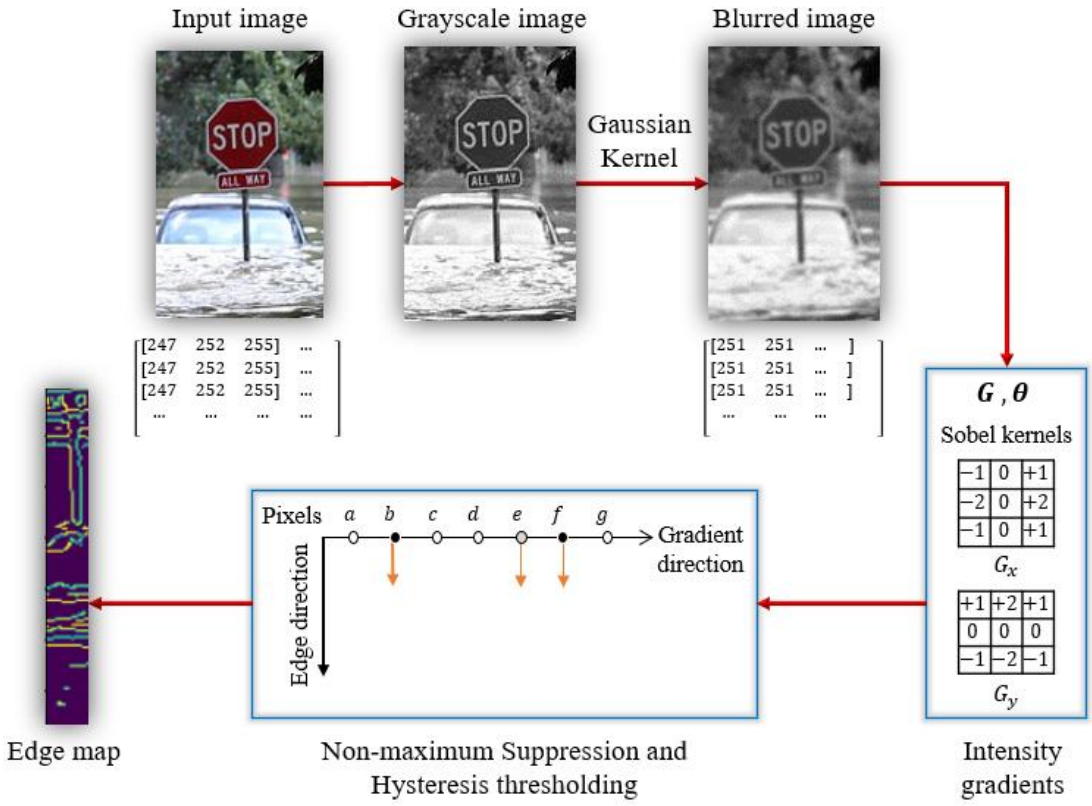

Figure IV-3 Canny edge detection process applied to a sample flood image.

Next, probabilistic Hough transform is utilized to detect straight lines in the output image of Canny edge detector, as potential pole candidates. Probabilistic Hough transform is commonly used to isolate features of a parametrically defined shape (e.g., line, circle, ellipse) within an image by a voting procedure (Li et al., 2020). Using this technique, the image coordinate system is transformed from the Cartesian space (x, y) to a polar space (ρ, θ) using Equation IV-5 in which, $\rho > 0$ and $0 \leq \theta \leq 2\pi$.

$$\rho = x \cos\theta + y \cos\theta \qquad \text{Equation IV-5}$$

The premise of probabilistic Hough transform is that if values defined by each edge pixel are plotted, points in the Cartesian space map to curves in the polar Hough parameter space. This point-to-curve transformation denotes the Hough transformation for straight lines. When viewed in Hough parameter space, points that are collinear in the Cartesian space become apparent as they form curves which intersect a common (ρ, θ) point. Four thresholds are defined, i.e., minimum line length (L_{min}), maximum allowed gap between points on the same line to link them (L_{gap}), accumulator threshold parameter that represents the number of votes for each line candidate $(L_{threshold})$, and distance resolution of the accumulator in pixels (L_{rho}). In this research, subsets of candidate points are randomly picked, and threshold values are empirically selected as $L_{min} = 30$, $L_{gap} = 10, L_{threshold} = 30$, and $L_{rho} = 1$ for pre-flood photos, and $L_{min} = 30$, $L_{gap} = 10, L_{threshold} = 80$, and $L_{rho} = 1$ for post-flood photos. The primary reason behind selecting two different $L_{threshold}$ values for pre- and post-flood photos is the background noise; in pre-flood photos, more line segments are needed to approve the pole line, while in post-flood photos, pole line can be identified with fewer line segments. The output of this step is a vector of matched endpoints of the detected straight and curved lines. For best results, tilt correction (will be discussed later) is later applied to all photos to ensure poles are in near vertical position prior to the application of Hough transform for detecting straight lines. With stop sign poles in near vertical position, only detected lines that are almost vertical are kept. Note that for a given image, the x-axis runs from left to right, and the y-axis runs from top to bottom with the origin in the top left corner. Several other problem-specific assumptions are made to reduce noise and confine the solution space to

a desired region within the image (i.e., pole is expected to appear under the sign), ultimately leading to an improved output. In particular,

a. The top of the pole is attached to the midpoint of the bottom edge of the octagon sign. The coordinates of this point, (x_{coo}, y_{coo}), are calculated from the geometry of the bounding box detected by the Mask R-CNN model. In particular, x_{coo} (measured along the horizontal axis of the image) is calculated by taking the average of the x coordinates of the lower corners of the bounding box (i.e., x_3 and x_4), while y_{coo} is equal to the y coordinate of one of the lower corners of the bounding box ($y_{coo} = y_3 = y_4$). This is shown in Figure IV-4.
b. The bottom of the pole always touches the ground (in pre-flood photos) or the waterline (in post-flood photos). If the pole is not titled, then the x coordinates of the top and bottom points of the pole are (almost) the same. In this case, the solution space (i.e., where pole is likely to be located) is horizontally confined along the x axis to $(x_{coo} - w, x_{coo} + w)$. The value of w can be empirically selected without excessively lowering the accuracy of line detection. In this research, w is set equal to the octagon side (S_{oct}), as shown in Figure IV-5.
c. The vertical length of the solution space (h) extends from the bottom edge of the octagon sign down to the bottom edge of the image, as shown in Figure IV-5.
d. In some cases, multiple vertical lines are detected under the octagon sign as pole candidates in close proximity from one another (e.g., due to visual inconsistencies such as different shades, colors, or textures). This situation is reconciled by directly connecting (x_{coo}, y_{coo}) to the endpoint that has the maximum y coordinate value

among all detected endpoints, i.e., $y = y_{max}$. The pole length is then calculated by measuring the distance between y_{coo} and y_{max}, as shown in Figure IV-6.

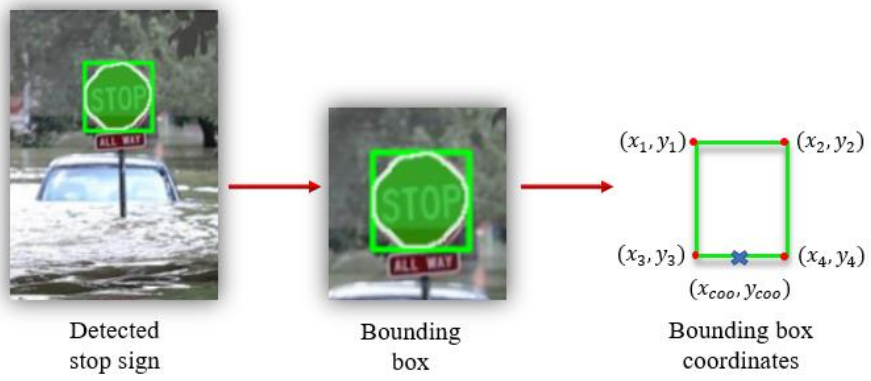

Figure IV-4 Determining the intersection point of the sign and pole from the stop sign bounding box

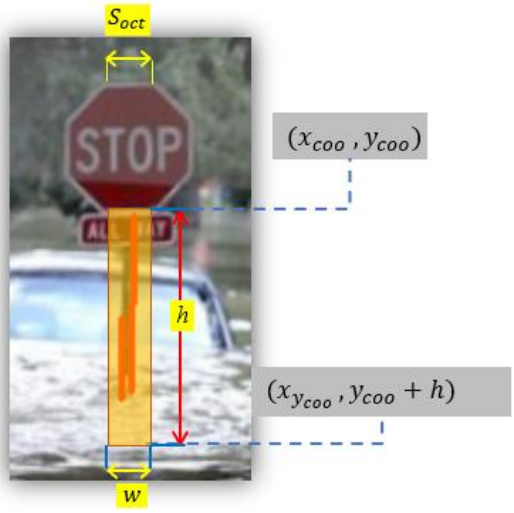

Figure IV-5 Confining the line detection solution space along horizontal axis.

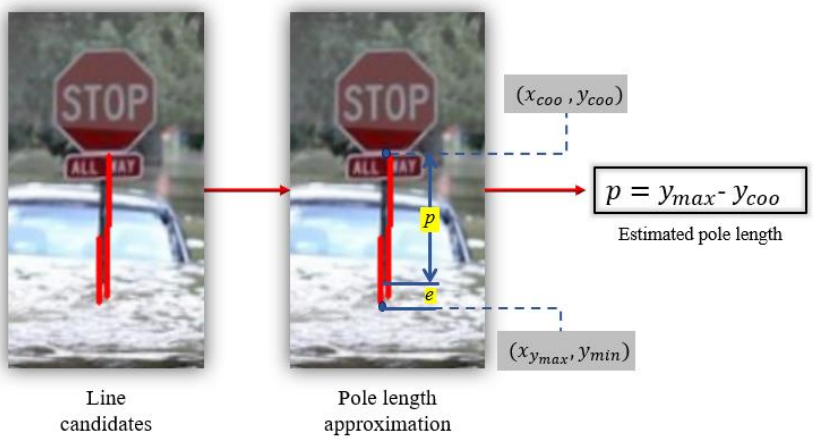

Figure IV-6 Approximating the stop sign pole from multiple close line candidates.

Data Description

A large number of flood photos are taken by people, emergency managers, and rescue teams in the aftermath of flood events. Many of these photos (especially those taken in urban areas) depict various traffic signs including stop signs that are submerged in floodwater. To test the methodology described in the previous section, publicly available flood photos that contain at least one visible stop sign are web-mined using keywords such as "street", "stop sign", and "flood" among others. For each photo, available geotag information including location (country, state/province, city, global coordinates), flood event name (if known), dates photo was taken and saved, and source (web link) is also extracted. Next, each post-flood photo is paired with a pre-flood photo of the same location containing the same stop sign, taken from Google Street View (GSV) API. The average time to pair a post-flood photo with the correct pre-flood photo can range from a few minutes (easy pairing, when geotag information is available) to 30 minutes (difficult pairing through excessive manual search or personal experience, with no geotag

information). For each pre-flood photo, longitude and latitude data, as well as a link to the exact location on Google Maps are stored as meta-data.

The dataset, named BluPix v.2020.1 contains 186 paired photos of submerged stop signs that are processed by Mask R-CNN and Canny edge detector and probabilistic Hough transform. Of these, 173 photos depict U.S. locations, and the remaining 13 photos are from locations in Canada. Table IV-1 show the geographical distribution of these photos across 10 FEMA regions (Ogawa et al., 2010) and Canada. As shown in this Table, the majority of paired photos (46%) in the U.S. belongs to FEMA region IV which covers locations in Alabama, Florida, Georgia, Kentucky, Mississippi, North Carolina, South Carolina, Tennessee, followed by region VI which contains Arkansas, Louisiana, New Mexico, Oklahoma, and Texas. A temporal analysis of BluPix v.2020.1 dataset reveals that 136 paired photos were taken from flood events that took place between 2011 and 2020, while 12 were taken from flood events that took place between 2000 and 2010, and 1 was taken prior to 2000, with the remaining missing date information. In particular, 93 flood photos were taken since 2017 which coincides with several highly active water-related events including Hurricane Harvey in Texas (FEMA Region VI) during which many people-contributed photos were posted on social media.

Table IV-1 Number of paired flood photos in BluPix v.2020.1 dataset in each FEMA region and Canada.

Region	Paired photos	Locations included
I	7	Connecticut, Maine, Massachusetts, New Hampshire, Rhode Island, Vermont
II	13	New Jersey, New York, Puerto Rico, U.S. Virgin Islands
III	17	Delaware, Maryland, Pennsylvania, Virginia, West Virginia, District of Columbia
IV	42	Alabama, Florida, Georgia, Kentucky, Mississippi, North Carolina, South Carolina, Tennessee
V	17	Illinois, Indiana, Michigan, Minnesota, Ohio, Wisconsin
VI	38	Arkansas, Louisiana, New Mexico, Oklahoma, Texas
VII	21	Iowa, Kansas, Missouri, Nebraska
VIII	4	Colorado, Montana, North Dakota, South Dakota, Utah, Wyoming
XI	13	Arizona, California, Hawaii, Nevada, American Samoa, Guam, Northern Mariana Islands, Marshall Islands, Micronesia
X	1	Alaska, Idaho, Oregon, Washington
Canada	13	Alberta, British Columbia, Ontario, Quebec, Queensland

Furthermore, 91% of flood photos were published on Google image repository (a.k.a., Google Images), 6% were accessed from Facebook, and other social media sites (i.e., Twitter, Pinterest) accounted for 1% or less of all photos in BluPix v.2020.1 dataset. An

interesting observation that in part motivated this research is that aside from Google, which is considered a search engine rather than a crowdsourcing platform, there is no dedicated online tool or website for ordinary people to upload flood photos, which adds to the already complex problem of collecting and analyzing these photos for the purpose of calculating and sharing floodwater depth information.

Results and Analysis

To prepare the ground-truth information, all stop signs and pole objects in the dataset are separately labeled. Figure IV-7 shows ground-truth examples in pre- and post-flood photos. This information is later used to determine the accuracy of Mask R-CNN in detecting stop sign masks, and Canny edge detector and probabilistic Hough transform in estimating pole lengths. Data processing is conducted on a Lenovo ThinkPad laptop computer with 7 cores, 9750H CPU, 16 GB RAM, and Nvidia Quadro T1000 GPU with a 4 GB memory.

(a) (b)

Figure IV-7 Ground-truth information in (a) a pre-flood photo, and (b) its post-flood paired photo.

To evaluate the performance of Mask R-CNN, the intersection over union (IoU) of detected and ground-truth masks is calculated by dividing the overlapping area between the two masks by their union area. IoU is a validated accuracy metric in object detection (K. He et al., 2017a; Z. Huang et al., 2019; Pi et al., 2020b). In addition to IoU, precision and recall are determined using Equations IV-6 and IV-7. In these Equations, true positive (TP) and true negative (TN) refer to the number of correct detections; TP indicates positive detections that are correct, while TN indicates negative detections that are correct. On the other hand, FP and false negative (FN) refer to the number of incorrect detections; FP indicates positive detections that are incorrect, while FN indicates negative detections that are incorrect (Powers, 2011).

$$Precision = \frac{\mathrm{TP}}{\mathrm{TP+FP}} \qquad \text{Equation IV-6}$$

$$Recall = \frac{\mathrm{TP}}{\mathrm{TP+FN}} \qquad \text{Equation IV-7}$$

Next, average precision (AP) is calculated by plotting precision as a function of recall and calculating the area under the curve (Dunham, 2006). From all 186 photos in BluPix v.2020.1 dataset, 27 are excluded since they only depict partially visible stop sign or sign pole. In the remaining 159 paired photos, stop signs are successfully detected in 142 pre-flood and 151 post-flood photos, resulting in 89.31% and 94.97% recall, respectively. Table IV-2 summarizes the performance of stop sign detection task in pre- and post-flood photos.

Table IV-2 Performance of stop sign detection in pre- and post-flood photos.

Metric	Pre-flood $n = 159$	Post-flood $n = 159$
IOU (%)	93.36	92.29
Precision (%)	100	100
Recall (%)	89.31	94.97
AP (%)	89.31	94.97
Processing time (s)	2.23	2.85

To evaluate the performance of Canny edge detector and probabilistic Hough transform for straight line detection, estimated pole length is compared with ground-truth length, and the root mean square error (RMSE) is calculated using Equation IV-8, in which, p and p' are detected and ground-truth lengths in pixels, respectively (Figure IV-1). Several visual features in analyzed photos lead to misdetection or highly erroneous pole detection. For pre-flood photos, for example, the top three sources of error include image background ($Er_p = 50.78$" for 6 photos with cluttered background), pole sideways tilt ($Er_p = 33.90$" for 4 photos with excessive pole tilt), and pole shape ($Er_p = 33.73$" for 8 photos with unusual pole shape). Similarly, for post-flood photos, the top three sources of error include wavy water surface ($Er_p = 69.80$" for 45 photos), water reflection ($Er_p = 55.53$" for 47 photos with pole reflection in water), and pole sideways tilt ($Er_p = 16.93$" for 5 photos with excessive pole tilt). Detection error due to the pole sideways tilt is further investigated in another section since this source of error is a common issue in both categories of pre-

and post-flood photos. A discussion of other error types, i.e., water reflection, pole shape, background effects, and image resolution, is beyond the scope of this study, and will be pursued as part of the future work in this research.

$$Er_p = \sqrt{\frac{1}{N}\sum_{m=1}^{N}(p - p')^2} \qquad \text{Equation IV-8}$$

Table IV-3 summarizes the performance of pole detection task in a subset of 42 pre-flood and 42 post-flood photos that were ultimately selected. To isolate and further study the effect of sideways tilt, photos in this subset do not depict unusual pole shapes, excessively cluttered background, water reflection, and wavy water surface. Each selected photo contains a detected stop sign (by Mask R-CNN) and at least one detected line (by edge and line detectors), and is assigned to one of the two groups of qualified photos showing a stop sign without tilt, or those showing a stop sign with excessive sideways tilt (e.g., $\pm 25°$).

Table IV-3 Performance of pole detection in pre- and post-flood photos before tilt correction.

Metric	**Pre-flood (all, no-tilt, tilted)**			**Post-flood (all, no-tilt, tilted)**		
	$n = 42$	$n = 38$	$n = 4$	$n = 42$	$n = 37$	$n = 5$
RMSE (in.)	21.67	20.38	33.90	15.30	15.08	16.93
Processing time (s)	1.78	1.76	1.93	2.07	1.94	2.19

Pole Tilt Correction

The general approach to tilt correction is to apply a reverse rotation to the image to visually rectify tilt. Given the standard shape of the stop sign, the amount of tilt (expressed in the 3D space by yaw, pitch, and roll angles, as in Figure IV-8) is determined based on the appearance of the octagon sign. The positive direction of rotations about each axis is determined using the right-hand grip rule (Cutnell & Johnson, 1998). First, a template octagon of 200×200 pixels is created in a binary color space and rotated along x, y, and z axes. The range of rotations for pitch and yaw angles is set to $(-45°, +45°)$ with $2°$ increments, because above this region the stop sign is hardly visible to Mask R-CNN. Since an octagon has rotational symmetry of order 8 with an internal angle of $135°$ and a central angle of $45°$, the shape of the octagon repeats in every $45°$ of rotation along the z axis. By limiting the range of the central rotation angle (i.e., roll) to $(-35°, +35°)$ with $2°$ increments, a total of $283{,}500$ rotation combinations in the 3D space are created and used as benchmarks to approximate yaw, pitch, and roll angles of the detected stop sign mask. Next, the mask is resized to the template octagon and laps over each benchmark octagon. As shown in Figure IV-9, in each case, the pixel overlap (shown as Ol) of the stop sign mask and the benchmark octagon is calculated. The comparison leading to the maximum overlap area (i.e., Ol_{max}) is selected as the one with closest rotation angles (in the 3D space) to the detected stop sign mask. Applying the reverse rotation to the image corrects the tilt problem by bringing the pole closer to vertical position. Since the size of the mask and the location of the bounding box may change as a result of this operation, the image

is reprocessed by Mask R-CNN to detect the stop sign mask, and Canny edge detector and probabilistic Hough transform to estimate pole length.

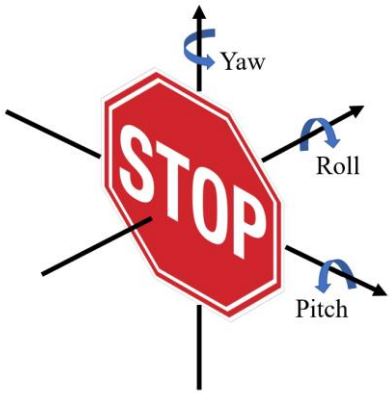

Figure IV-8 Three different directions for rotation.

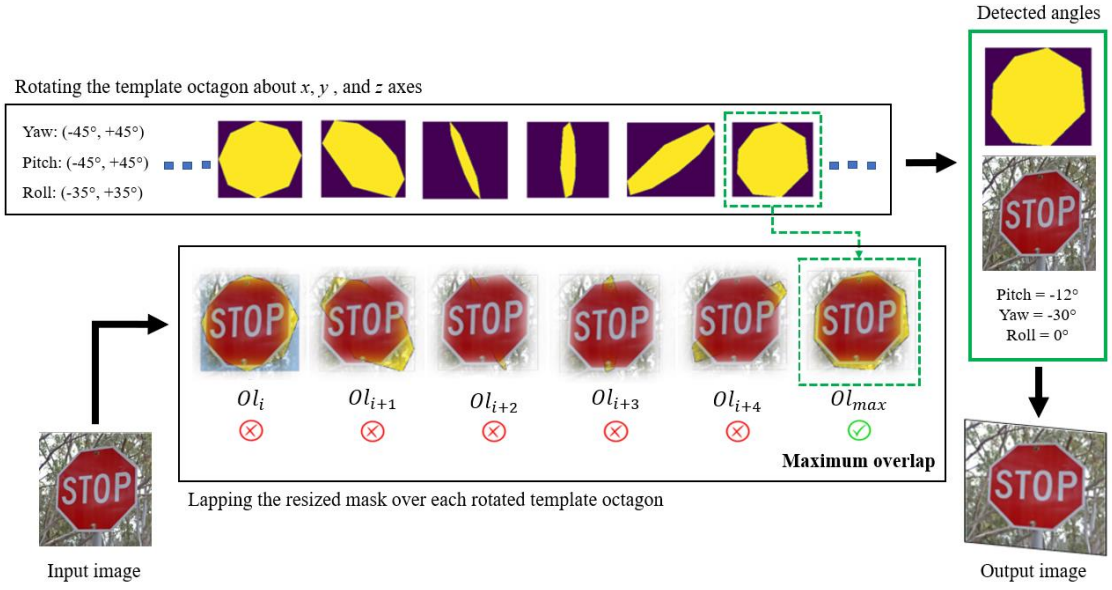

Figure IV-9 Title angle detection using template stop signs.

Table IV-4 summarizes the performance of pole detection task in pre- and post-flood photos after tilt correction. Comparing Table IV-3 and Table IV-4, it is evident that

applying tilt correction reduces the error of pole detection in both pre- and post-flood photos. In particular, the overall error in pole detection after tilt correction is 17.43" (compared to 21.67" in Table IV-3) in pre-flood photos and 8.61" (compared to 15.30" in Table IV-3) in post-flood photos. It can thus be concluded that the designed tilt correction method improves the accuracy of pole detection, especially in post-flood photos where the presence of sideways tilt is more apparent.

Table IV-4 Performance of pole detection in pre- and post-flood photos before tilt correction.

Metric	Pre-flood (all, no-tilt, tilted)			Post-flood (all, no-tilt, tilted)		
	$n = 42$	$n = 38$	$n = 5$	$n = 42$	$n = 37$	$n = 5$
RMSE (in.)	17.43	16.49	26.39	8.61	9.56	1.62
Processing time (s)	3.34	3.35	3.31	3.56	3.32	3.71

Floodwater Depth Estimation

Knowing the pole length in paired pre- and post-flood photos taken from the same location, the depth of floodwater d_w is calculated as the difference between the two pole lengths. Figure IV-10 shows sample results from floodwater depth calculation. In Figure IV-10(a), pole lengths in pre- and post-flood photos are estimated as 47.26 inches (compared to the ground-truth of 47.81 inches) and 23.61 inches (compared to the ground-truth of 24.88 inches), indicating 23.65 inches of floodwater.

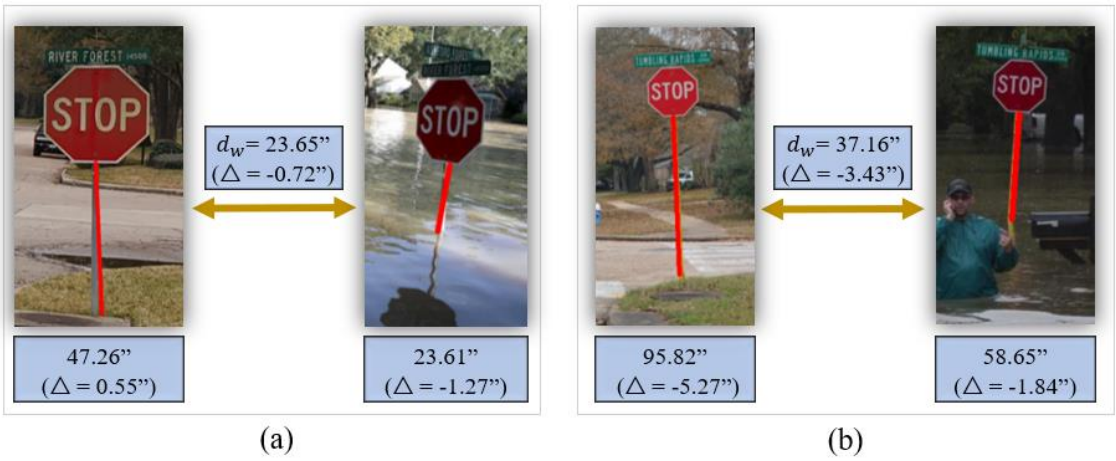

Figure IV-10 Examples of floodwater depth estimation for paired pre- and post-flood photos.

Overall, floodwater depth estimation leads to an MAE of 12.63 inches. In comparison, Cohen et al. (2019) reported an average absolute difference of 18-31 cm (approximately 7-12 inches) in estimating the depth of flood for coastal (using a 1-m DEM) and riverine (using a 10-m DEM) locations (Cohen et al., 2019), Chaudhary et al. (2019) obtained an MAE of 10 cm (approximately 4 inches) using social media images that depict submerged objects of various sizes (Chaudhary et al., 2019), and Park et al. (2021) presented an MAE value of 6.49 cm (approximately 2.5 inches) using images of flooded vehicles (Park et al., 2021). However, it must be noted that the real added value of the developed technique in this study is its generalizability to new scenarios (stop signs are omnipresent and easy to locate), as well as its scalability by significantly increasing the number of points where floodwater depth estimation can be calculated.

Computer Vision Model II: Training Convolutional Neural Networks for Flood Depth Estimation

Object Detection Model for Pole Detection

For visual recognition of stop signs and their poles, a robust and accurate object detection model is desired. Moreover, to implement the flood depth estimation technique on mobile devices, the model should be computationally light. To satisfy these two design conditions, You Only Look Once (YOLO) v4 (Bochkovskiy et al., 2020) was utilized for stop sign and pole detection. YOLOv4 is fast and accurate, and features a light version (a.k.a., Tiny YOLO) for implementation on mobile devices. Other object detection models such as RetinaNet-101-500 (T. Y. Lin et al., 2017), R-FCN, Single Shot Detector (SSD) 321 (W. Liu et al., 2016), and Deconvolutional Single Shot Detector (DSSD) 321 (Fu et al., 2017) achieve mAP of 53.1% (at 11 frames per second (FPS)), 51.9% (at 12 FPS), 45.4% (at 16 FPS), and 46.1% (at 12 FPS) on the Microsoft COCO dataset (T.-Y. Lin et al., 2014), respectively. By comparison, YOLOv3-320, YOLOv3-416, and YOLOv3-608 models (Redmon & Farhadi, 2018) yield mAP of 51.5% (at 45 FPS), 55.3% (at 35 FPS), and 57.9% (at 20 FPS) on the same dataset, respectively. YOLOv4 surpasses YOLOv3 in terms of speed and accuracy, by achieving 65.7% mAP at 65 FPS on the Microsoft COCO dataset. This superior performance is primarily the result of using a different backbone in the YOLOv4 model. Particularly, the model utilizes the cross-stage-partial-connections (CSP) network with Darknet-53 (Bochkovskiy, 2020) as the backbone for more efficient feature extraction. As shown in Figure IV-11, this backbone extracts essential features from the input image, which are then fused in the neck of the YOLO model. The neck is

comprised of layers that collect feature maps from different stages. This part of the model consists of two networks, namely spatial pyramid pooling (SPP) (K. He et al., 2015)and path aggregation network (PANet) (Liu S. et al., 2018). The neck consists of several top-to-bottom paths and bottom-to-top paths that better propagate layer information. Similar to the head of YOLOv3, the head of YOLOv4 adopts the feature pyramid network (FPN) (T. Y. Lin et al., 2017), predicts object bounding boxes, and outputs the coordinates along with the widths and heights of detected (Redmon & Farhadi, 2018) through three YOLO layers.

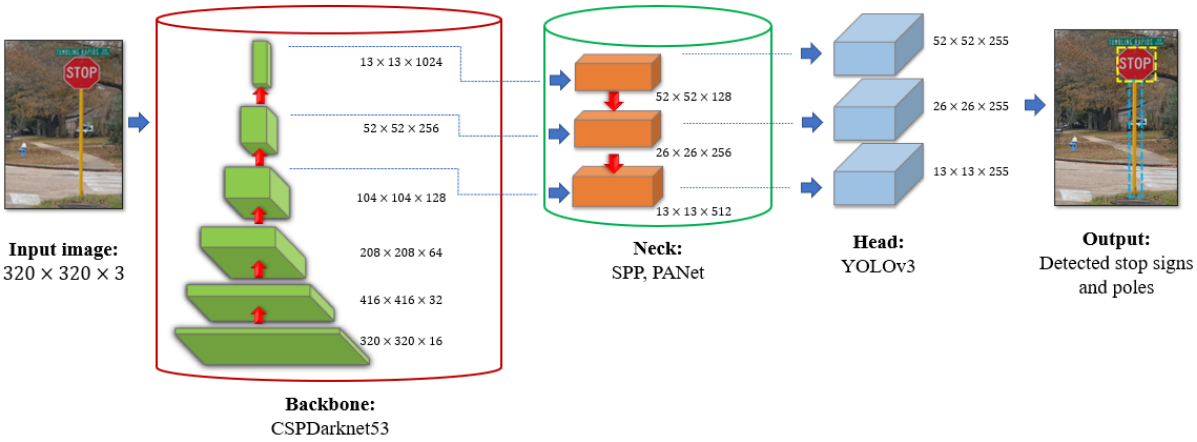

Figure IV-11 The architecture of the YOLOv4 network adopted in this research.

Pre-trained model

The YOLOv4 model is pre-trained on the publicly available Microsoft COCO dataset to detect 80 object classes. To train the adopted model on the target dataset in this study, transfer learning is used, which is a validated approach for training a CNN model on a relatively small dataset (a.k.a., target dataset) by transferring pre-defined weights (that the network has learned when trained on a large dataset) to allow the model to detect relevant

intermediate features (Gao & Mosalam, 2018; Han et al., 2018; Hussain et al., 2019; Tammina, 2019). The dataset used for training has images containing two classes: stop sign and pole. This reduces the output size of YOLO layers from 80 classes to 2 classes. Using transfer learning, all network weights except those of the last three YOLO layers are kept constant (i.e., frozen). At the beginning of the training process, the weights of the three YOLO layers are randomly selected, and then constantly optimized with the goal of maximizing the mAP for pole and stop sign detections. At these optimal values, the model is neither overfitting (i.e., unable to detect objects in new data due to overly learned features in the training set and forgetting general features) nor underfitting (i.e., unable to detect objects in training data and new data due to limited features that were learned).

Clustering The Training Set

YOLO models use pre-defined anchor boxes, which are a set of candidate bounding boxes with fixed width and height initially selected based on the dataset, and subsequently scaled and shifted to fit the target objects (Ju et al., 2019). The YOLOv4 model, in particular, utilizes nine anchor boxes. Therefore, all 1,262 ground-truth boxes in the training set (containing instances of both stop sign and pole classes), shown in Figure IV-12(a), are clustered into nine groups using k-means clustering ($k = 9$) (Redmon & Farhadi, 2018). The centroids of these nine clusters are used to define nine anchor boxes, as illustrated in Figure IV-12(b).

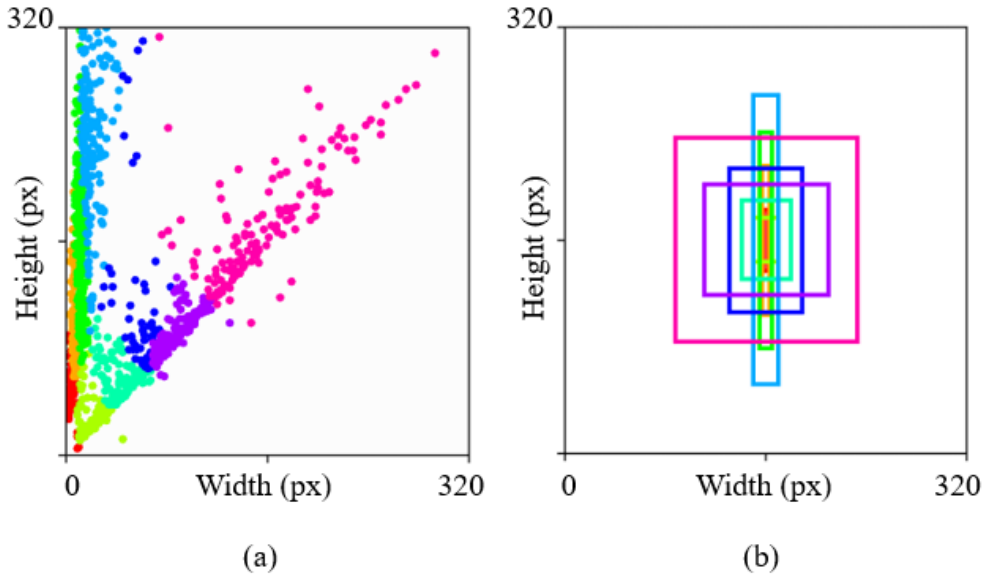

Figure IV-12 *(a)* Nine clusters (k = 9) corresponding to the training set, and (b) Recalculated anchor boxes for the in-house dataset

Training the Model

Following Bochkovskiy (2020), the adopted YOLOv4 model is trained for 4,000 iterations (2,000 iterations for each class), with a learning rate of 0.001 using Adam optimizer (Kingma & Ba, 2014), with a batch size of 1 and subdivision of 64. The Darknet-53 (backbone of this model) is built in Windows on a Lenovo ThinkPad laptop computer with 7 cores, 9750H CPU, 16 GB RAM, and Nvidia Quadro T1000 GPU with a 4 GB memory. The network resolution (i.e., image input size) is reduced to the size of $320 \times 320 \times 3$ to lower computational cost and time. The total processing time for training the model is approximately 12 hours, with an average loss of 0.567.

Random and real-time data augmentation is automatically applied to the training set to increase the size of training data by creating slightly modified copies of existing images.

Past studies have investigated various approaches to data augmentation. In particular to the YOLO architecture, Kang et al. (2019) changed the hue, saturation and exposure of images for training a Tiny YOLO model to detect fire (Kang et al., 2019). Ma et al. (2020) applied color jittering and saturation, exposure, and hue change for augmenting images of thyroid nodules for training a YOLOv3 model (Ma et al., 2020). Koirala et al. (2019) augmented images of fruits for training a YOLO model by modifying hue, saturation, jitter and multiscale (Koirala et al., 2019). Lastly, Niu et al. (2020) applied image mosaic, horizontal flipping, and image fusion for augmenting images of sanitary ceramics for training a Tiny YOLO model (Niu et al., 2020). In this study, hue, saturation, and exposure of training samples are changed within [-18…+18], [0.66…1.5], and [0.66…1.5], respectively as recommended by Bochkovskiy et al. (2020). Also, a Jitter (random image cropping and resizing by changing the aspect ratio) of 0.3 is implemented for data augmentation. The maximum jitter allowed in data augmentation is 0.3 (R. Hu et al., 2020; Ma et al., 2020). Moreover, 50% of images are flipped horizontally but no image is flipped vertically (R. Hu et al., 2020). Lastly, 50% of images are augmented with a mosaic by combining four different images into one image (Hao & Zhili, 2020).

Validating the Model

To prevent overfitting (i.e., a model that is exactly fitted to the training data, preventing it from correctly detecting new data), model performance is monitored on validation sets using a 5-fold cross validation approach (Browne, 2000; Islam et al., 2020; Lyons et al., 2018; Seyrfar et al., 2021). Using this approach, 160 photos are randomly drawn (without replacement) from the training set (20% of the total of 800 images in the training set) for

five times as validation sets, and the remaining photos are used for model training. The model is then trained on each training set for 4,000 iterations and validated on the corresponding validation set. The number of epochs is the number of iterations divided by the number of images over the batch size. With the batch size of 1, there are a total of 5 epochs in 4,000 iterations. During the training process, the highest mAPs on the validation sets along with the corresponding number of iterations are saved. Next, average performance is calculated as the average of obtained mAP values across all validation sets. The optimum number of iterations is also computed as the average of the best number of iterations (corresponding to the highest mAP) in all validation sets. In this study, the average mAP and average iteration numbers achieved in 5-fold cross validation are 97.04% and ~3,000 (since model weights are saved at every 1,000 iterations, the optimum number of iterations is rounded to 3,000 to be exact). This means that after 3,000 iterations, the model shows a tendency to overfit to the training data. Ultimately, the model is trained on the entire training and validation sets for the obtained optimum number of iterations (i.e., 3000), and the mAP at 3000^{th} iteration is reported. The set of network weights saved at this number of iterations is marked as optimum and used for testing the model. Table IV-5 shows the validation output of the trained model on each validation set.

Table IV-5 The highest average performance of the trained model on five validation sets using 5-fold cross validation (S: Stop sign; P: sign pole; S+P: stop sign and sign pole).

Metric	Class	Validation set 1	2	3	4	5	Average of 5 validation sets
Average IoU	S+P	83.74%	85.05%	86.82%	85.92%	84.75%	85.26%
Precision @ 0.25 conf	S+P	95.00%	97.00%	97.00%	96.00%	97.00%	96.40%
Recall @ 0.25 conf	S+P	94.00%	97.00%	96.00%	95.00%	94.00%	95.20%
AP	S	97.37%	97.37%	97.37%	97.37%	97.37%	97.37%
	P	97.37%	97.37%	97.37%	97.21%	94.20%	96.70%
mAP @ 0.50	S+P	97.37%	97.37%	97.37%	97.29%	95.78%	97.04%
No. of iterations	S+P	3,000	3,500	2,800	3,500	2,400	3,025

Tilt Correction

Over time or as a result of floodwater flow, traffic signs can be tilted in any direction, leading to the underestimation of the submerged pole height by the YOLOv4 model (since detected bounding boxes are not tilted), and eventually erroneous floodwater depth calculation. In cases where both pre- and post-flood photos are tilted by the same angle, floodwater depth calculation is not impacted by the tilt. However, if the degrees of tilt

differ between pre- and post-flood photos of the stop sign, pole length estimation should be adjusted prior to calculating the floodwater depth. In Figure IV-13, pre-flood and post-flood stop signs are presented with unequal tilt degrees (α degrees for pre-flood stop sign and β degree for post-flood stop sign). For each photo, the actual pole length is the reverse projection of the height of the detected bounding box (P and P') by the degree of tilt (α and β). Equation IV-9 presents the calculation of flood depth considering unequal degrees of tilt for a given paired stop sign photo.

$$W = P\left(\frac{\cos\alpha}{\cos\beta}\right) - P' \qquad \text{Equation IV-9}$$

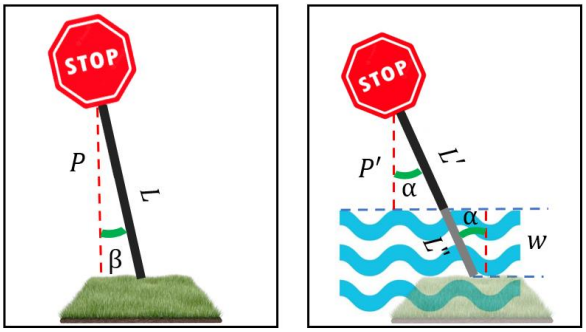

Figure IV-13 Adjusting flood depth estimation for pre-flood and post-flood stop signs with unequal degrees of tilt.

To automatically detect the degree of sideways tilt, a tilt correction technique is implemented and applied before stop sign and pole detection. By visually inspecting the photos in the dataset, it is observed that the maximum tilt does not exceed 25º. Thus, a range of [-25º…+25º] was selected for tilt correction. Next, as shown in Figure IV-14, the input image is rotated from 0 to -25º clockwise (in 5º intervals) and from 0 to +25º

counterclockwise (in 5º intervals). Generated images are then processed by the trained YOLO model for stop sign and pole detection. The image with the minimum width of the pole detection bounding box is ultimately selected as the one containing the most vertical pole. Consequently, the degree of tilt that was applied to the original image to generate this image is calculated as the tilt angle (β degrees for pre-flood stop sign and α degree for post-flood stop sign).

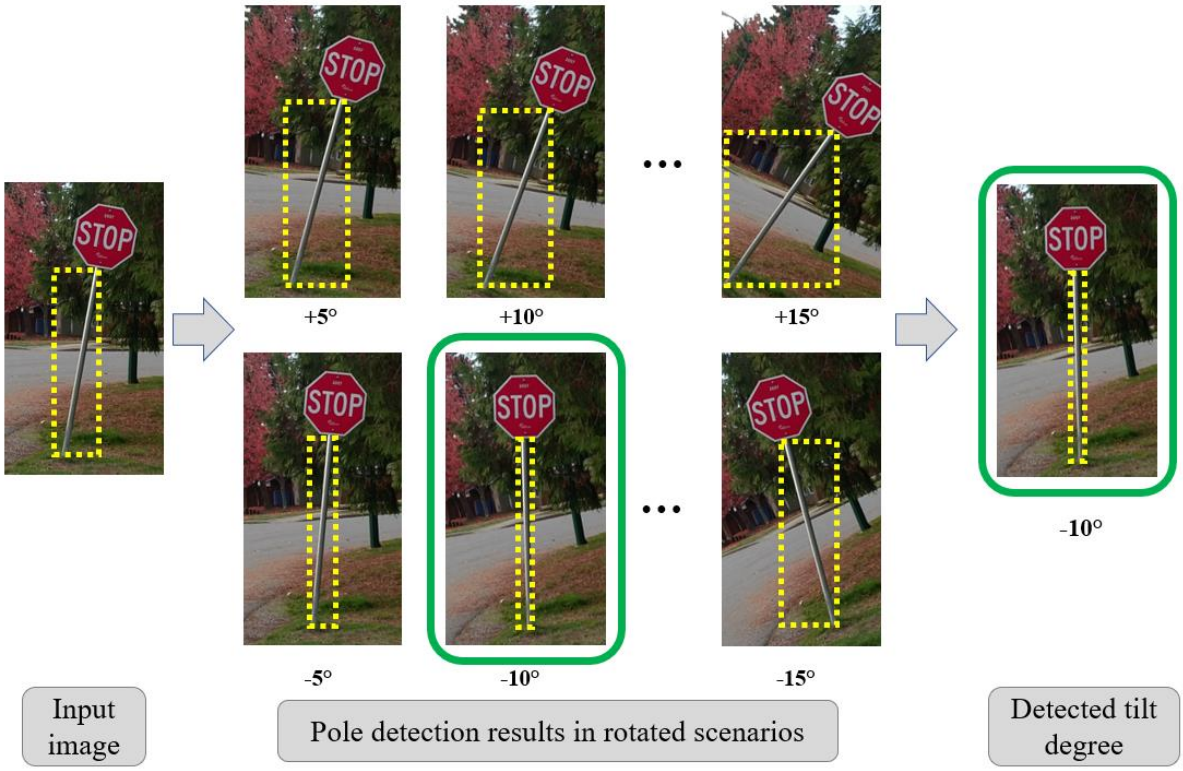

Figure IV-14 Tilt detection approach (base photo is courtesy of KjzPhotos/Shutterstock).

Model Performance

In object detection, a commonly used metric for measuring model performance is mAP (Ren et al., 2017; Turpin & Scholer, 2006). The basis of mAP calculation across all classes is the average precision for each individual class. In turn, the AP for any given class is measured using IoU (Javadi et al., 2021; Kido et al., 2020; Nath & Behzadan, 2020), which is calculated for each detection based on the overlap between the predicted bounding box (B') and the ground-truth bounding box (B) (Equation IV-10). Following this, the detected object is classified as correct (if the IoU is above a predefined threshold, typically 50%), or incorrect (if the IoU is below the threshold) (Nath & Behzadan, 2020; L. Zhu et al., 2021). Based on the correctness of the detected object, TP (correct classification to a class), FP (incorrect classification to a class), and FN (incorrect classification to other classes) cases are counted. Next, Equation IV-11 and Equation IV-12 are used to calculate precision (model's ability to detect only relevant objects) and recall (model's ability to detect all relevant classes) based on TP, FP and FN for each class (Guo et al., 2021; Mao et al., 2021; Padilla et al., 2020; Xu et al., 2021). It must be noted that true negative (TN) cases are not considered in object detection when measuring model performance, as there are countless number of objects (belonging to a large number of classes) that should not be detected in the input image (Padilla et al., 2020).

$$IoU = \frac{B' \cap B}{B' \cup B} \qquad \text{Equation IV-10}$$

$$Precision = \frac{TP}{TP+FP} \qquad \text{Equation IV-11}$$

$$Recall = \frac{TP}{TP+FN} \qquad \text{Equation IV-12}$$

To calculate the AP of any object class, all detections are initially sorted based on their confidence scores in descending order, and Equation IV-13 is then applied. In this Equation, N refers to the total number of detected bounding boxes, i refers the rank of a particular detection in the sorted list, P_i refers to the precision of the ith detection, and Δr is the change in recall between two consecutive detections ith and $(i+1)$th. Finally, mAP is calculated as the AP over all classes, as formulated by Equation IV-14 (Lyu et al., 2019; Nath & Behzadan, 2020).

$$AP = \frac{1}{N} \sum_{i=1}^{N} P_i \Delta r_i \qquad \text{Equation IV-13}$$

$$mAP = \sum_{i=1}^{N} AP_i \qquad \text{Equation IV-14}$$

Flood Depth Estimation

Flood depth is estimated using the YOLOv4 model trained on photos of stop signs taken before and after flood events. The general framework for detecting stop signs and their poles in pre- and post-flood photos and estimating flood depth is illustrated in Figure IV-15. As shown in this Figure, paired pre-flood and post-flood photos of a stop sign are processed by presenting them to the model as two separate inputs. The model then detects the stop sign and its pole in each image, and measures the length of the visible part of the detected poles using geometric calculations based on the size of stop signs. Next, the depth of floodwater at the location of the stop sign is estimated as the difference between pole lengths in pre- and post-flood photos.

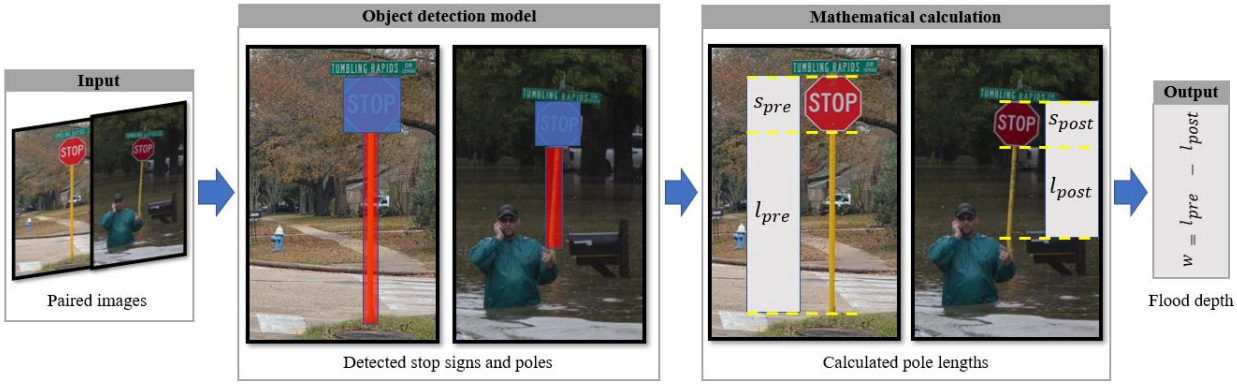

Figure IV-15 Workflow for estimating flood depth in a sample paired pre- and post-flood photos (base post-flood photo is courtesy of Erich Schlegel/Getty Image).

In addition to evaluating the model performance in stop sign and pole detection, its ability to estimate flood depth must be assessed. The literature in this field has used MAE as an informative metric to describe the discrepancy in flood depth estimation (Alizadeh & Behzadan, 2022; Alizadeh Kharazi & Behzadan, 2021a; Chaudhary et al., 2019; Cohen et al., 2019; Park et al., 2021). In this study, the error of pole detection in pre-flood and post-flood photos is determined as the difference between ground-truth pole length (l^g) and detected pole length (l^d). The absolute error in a single image is then calculated as the cumulative error in pre-flood and post-flood photos. Since the depth of flood is measured based on the difference between pole lengths in M paired pre- and post-flood photos, the MAE for flood depth estimation can be determined as the average of absolute errors in all paired photos (Equation IV-15).

$$MAE = \frac{1}{M}\sum_{1}^{M} \left| \left({l^g}_{pre} - {l^d}_{pre}\right) + \left({l^g}_{post} - {l^d}_{post}\right) \right| \qquad \text{Equation IV-15}$$

Data Description

Table IV-6 shows a detailed breakdown of the image datasets used to train and test the model. The data used for training the adopted YOLO model to detect stop signs and sign poles consists of two image datasets: pre-flood photos and post-flood photos (Blupix v.2021.2). Each dataset is described in detail in the following sections. The data used for testing the YOLO model comprises 176 pre-flood and 172 post-flood photos drawn from the Blupix v.2021.1 dataset (containing 224 pairs of pre- and post-flood photos, i.e., 448 photos in total), by filtering out photos with very low resolution or those in which entire poles are not captured. The Blupix v.2021.1 dataset is an expanded version of the Blupix v.2020.1 (Alizadeh Kharazi & Behzadan, 2021b) which contained 186 pairs of pre- and post-flood photos; i.e., 372 photos in total.

Table IV-6 Overview of the training and test datasets.

Dataset	Subset	Source	Language	Count	Total
Training set (Blupix v.2021.2)	Post-flood	Web-mining	English	196	800
			Spanish	6	
			French	55	
			Turkish	13	
		Synthetic	English	64	
		Non-labeled	English	61	
	Pre-flood	COCO	English, Spanish, French, Turkish, Arabic, etc.	334	
		Non-labeled	English	71	
Test set (Blupix v.2021.1)	Post-flood	Web-mining	English	164	348
			French	8	
	Pre-flood	Web-mining	English	168	
			French	8	

Pre-flood training dataset

There are publicly available large-scale datasets containing images of stop signs. The pre-flood training dataset is generated by extracting a subset of photos of stop signs with the entire stop sign poles in the photo from the Microsoft COCO dataset. Figure IV-16 shows examples of stop sign photos in different countries, with different forms and pole shapes, extracted from the Microsoft COCO dataset. Although all stop sign objects were already annotated in the Microsoft COCO dataset, it was found that some annotations were not as accurate as expected. For example, shapes of masks drawn over stop signs were not always octagonal. To resolve this problem, all extracted images were re-annotated by the author. Ground-truth bounding boxes were determined by manual labeling, e.g., outlining stop signs and poles by polygons using LabelMe software (Wada, 2016), which for each photo took approximately 45 seconds. Although annotating images with rectangular bounding boxes was sufficient for implementing the YOLO model, it was ultimately decided to annotate using masks to achieve more accurate shapes (octagonal masks over stop signs and quadrilateral masks over sign poles) and to facilitate the generalizability of the annotations for future studies. At the conclusion of the annotation step, all masks were converted to bounding boxes which is the required input format of the YOLO model. Sample annotated pre- and post-flood photos are shown in Figure IV-17. These photos depict a stop sign at the intersection of Tumbling Rapids Dr. and Hickory Downs Dr. in Houston, Texas. The post-flood photo was obtained via crowdsourcing after Hurricane Harvey (2017), and the pre-flood photo was taken by the authors on January 23, 2021.

Figure IV-16 Photos of various stop signs in different forms and languages available from the Microsoft COCO dataset.

Figure IV-17 Sample annotated (a) pre-flood photo, and (b) post-flood photo (base photo in (b) is courtesy of Erich Schlegel/Getty Images).

Post-flood training dataset

For post-flood photos, an in-house dataset is created which contains 270 web-mined photos of flooded stop signs. Web-mining is conducted using related keywords such as "flood stop sign", "flood warning sign", and their translations in three other languages (i.e., Spanish, French, Turkish). To increase the generalizability of the model, also photos taken from the back side of the sign, those depicting tilted poles or reflections in water, as well as photos taken in daylight or nighttime, photos with clear or noisy backgrounds, and photos taken in different weather conditions were included. Additionally, to minimize detection error, the dataset is further balanced by generating synthetic training data (FEINGERSH et al., 2007; T. Y. Hu et al., 2021; Shaghaghian & Yan, 2019; Tremblay et

al., 2018). In particular, a new set of post-flood photos depicting flooded traffic signs (other than stop signs) is imported in a photo editing tool where the depicted traffic signs are replaced with stop signs (keeping the pole unchanged). Using this method, 64 synthetic images are added to the dataset which results in a total of 334 post-flood photos.

Non-labeled objects

Since the model is trained on stop signs in different languages (with white text on a red octagonal shape), it could learn overly detailed features that may not be generalizable, resulting in potentially FP cases. To resolve this problem, the training set is further enriched with samples that are visually proximal to stop signs but are not stop signs, to force the model to learn distinctive characteristics specific to stop signs while avoiding FPs. In particular, 71 web-mined pre-flood photos and 61 web-mined post-flood photos of other traffic signs similar to stop signs (such as "Do Not Enter" signs) are added to the training dataset.

Results and Analysis

Performance of the trained model

In this section, the performance of the trained YOLOv4 model is evaluated on the test dataset, and results are discussed. For the test set, 176 pre-flood and 172 post-flood photos were extracted from the Blupix v.2021.1 dataset by filtering out photos with significantly low resolution or those in which parts of poles and/or stop signs were not visible. Of these pre- and post-flood photos, 163 photos are paired. Table IV-7 summarizes model performance with the optimum trained weights when tested on the test set. As shown in this Table, the AP calculated for stop sign and pole detection in pre-flood photos is 100%

and 99.41%, respectively. Similarly, the AP calculated for stop sign and pole detection in post-flood photos is 99.73%, and 98.73%, respectively. The mAP for pre- and post-flood photos is 99.70% and 99.23%, respectively. The relatively higher mAP for pre-flood photos can be attributed to less noise in these photos compared to post-flood photos. The average detection times for all detections in pre-flood and post-flood photos are 0.05 and 0.07 seconds, respectively, which is close to real-time.

Table IV-7 Performance of the trained model in detecting stop signs and poles in pre- and post-flood photos of the test set (S: Stop sign; P: sign pole; S+P: stop sign and sign pole).

Metric	Class	Pre-flood (*n* = 176)	Post-flood (*n* = 172)	All photos (*n* = 348)
Average IoU	S+P	93.85%	86.25%	90.05%
Precision @ 0.25 conf	S+P	0.99	0.94	0.96
Recall @ 0.25 conf	S+P	0.99	0.95	0.97
AP	S	100.00%	99.73%	99.84%
	P	99.41%	98.73%	99.16%
mAP @ 0.50	S+P	99.70%	99.23%	99.50%
F1-score	S+P	0.99	0.94	0.97
Average detection time (sec)	S+P	0.05	0.07	0.05

Without considering the uneven degrees of tilt for few paired photos, the model can calculate pole lengths in test images with an MAE of 1.856 in. and 2.882 in. for pre- and post-flood photos, respectively. The slightly higher error corresponding to post-flood photos can be primarily attributed to the presence of visual noise in post-flood scenes. To examine the tilt correction method, 37 images of stop signs in the test set with uneven pole tilt degrees in pre- and post-flood photos are identified. After implementing the tilt correction technique, the MAE of the trained YOLOv4 model on the Blupix v.2021.1 dataset is reduced to 1.723 in. and 2.846 in. for pre- and post-flood photos, respectively, showing a slight improvement in flood depth estimation outcome as a result of implementing the tilt correction technique. However, it is anticipated that with more paired photos depicting uneven degrees of tilt, the reduction in error becomes more significant. Table IV-8 summarizes model performance on the test set. To calculate the error of flood depth estimation, ground-truth floodwater depth (i.e., the difference between ground-truth pole lengths in paired pre- and post-flood photos) is compared with the estimated floodwater depth (i.e., the difference between detected pole lengths in paired pre- and post-flood photos). The MAE of the model for flood depth estimation on 163 paired photos were achieved as 4.737 in. and 4.710 in. before and after implementing the tilt correction technique, respectively.

Table IV-8 Performance of the trained model in estimating pole lengths in pre- and post-flood photos of the test before and after tilt correction.

Source	Metric	Pre-flood (*n* = 176)	Post-flood (*n* = 172)	Paired photos (*n* = 163)
Before tilt correction	RMSE (in.)	3.924	5.557	7.847
	MAE (in.)	1.856	2.882	4.737
	Average processing time (s)	0.05	0.08	0.08
After tilt correction	RMSE (in.)	3.355	5.544	7.857
	MAE (in.)	1.723	2.846	4.710
	Average processing time (s)	0.05	0.08	0.08

Model verification using baseline methods

In this section, the developed model is verified by comparing its performance with two baseline methods. Model verification is the process of checking that the model has been implemented correctly and that the calculations are accurate (Carson, 2003). In particular, this step helps verify whether the performance of the YOLOv4 model exceeds that of two intuitive baseline methods, referred to herein as dummy methods I and II, which return some average values given a set of pole length values. In dummy method I, for a given pre-flood (post-flood) test image, the model returns the average pole length of all pre-flood (post-flood) images in the training set. The average pole length for pre-flood and

post-flood photos in the training set is 76.98 in. (n = 334) and 53.38 in. (n = 395), respectively. Using dummy method I, the MAE for the pre-flood photos and post-flood photos in the test set is thus determined as 44.628 in. (n = 176) and 49.804 in. (n = 172). In dummy method II, for a given pre-flood (post-flood) test image, the model returns the running average pole length of all previously seen pre-flood (post-flood) images in the test set. Running average is a common method for extracting an overall trend from a list of values, by continuously updating an average value considering all data points in the set until the calculation point (Crager & Reitman, 1991; Du et al., 2008; PIERCE, 1971). To reduce the order effect and allowing for a thorough examination of the variability and accuracy of the model across a range of randomized data sets, pole length values are recorded in 100 iterations each containing a randomized order of test images. Consequently, the performance of dummy method II is calculated as the MAE of all 100 obtained running averages. The MAE achieved for dummy method II for pre-flood and post-flood photos is 13.271 in. and 20.469 in., respectively. Also, the minimum and maximum MAE achieved for pre-flood (post-flood) is found to be 0.056 in. and 42.830 in. (0.344 and 45.824), respectively. Our results show that dummy method II is able to reduce the pole length estimation error to less than 1 in. in only one randomized set. However, dummy method II outperforms dummy method I, yet is highly sensitive to the order of values. Comparing the MAE of the proposed YOLOv4 model, (i.e., 1.723 in. for pre-flood photos and 2.846 in. for post-flood photos) with the MAEs of dummy methods I and II, it is clear that our proposed model outperforms the two baseline methods. Table

IV-9 summarizes the MAE and root mean squared error (RSME) obtained using dummy methods I and II.

Table IV-9 Performance of dummy methods I and II on the test set.

Baseline method	Category (Test set)	MAE (in.)	RMSE (in.)
Dummy method I	Pre-flood (n = 176)	44.628	51.884
	Post-flood (n = 172)	49.804	60.165
Dummy method II	Pre-flood (n = 176)	13.271*	* MAE reported over 100 randomized iterations
	Post-flood (n = 172)	20.469*	

Impact of stop sign language on model performance

To analyze the performance of the model in different languages, MAE and RMSE values are calculated for various subsets of photos (after implementing tilt correction), with results summarized in Table IV-10. The analysis indicates that in pre-flood photos, the MAE for stop signs in French is 4.628 in., which is higher than the MAE of 1.585 in. for stop signs in English. On the other hand, in post-flood photos, the MAE for stop signs in French is 1.565 in., which is lower than the MAE of 2.908 in. for stop signs in English. Further investigation reveals that the MAE for pole length estimation is impacted by image quality rather than stop sign language. For example, web-mined post-flood photos of stop

signs in French language are in high-resolution (taken by professional cameras), thus lowering the corresponding MAE. In contrast, the quality of one of the French pre-flood photos was significantly low which led to a higher MAE for pole length estimation in the corresponding subset.

Table IV-10 The performance of the flood depth estimation model based on stop sign language.

Category	Language	MAE (in.)	RMSE (in.)
Pre-flood	English (168)	1.585	3.078
	French (8)	4.628	6.977
	Total (176)	1.723	3.355
Post-flood	English (164)	2.908	5.662
	French (8)	1.565	1.876
	Total (172)	2.846	5.544

Benchmarking

In this section, model validation (assessing how well the model represents the real-world phenomenon it is intended to model (Carson, 2003)) is conducted by benchmarking with similar research in this domain. As stated earlier, the model achieved an MAE of 4.710 in.

on 163 paired images in the test set after implementing tilt correction. By comparison, Cohen et al. (2019) obtained an average absolute difference of 18-31 cm (approximately 7-12 in.) for flood depth estimation in coastal and riverine areas, Chaudhary et al. (2019) reported an MAE of 10 cm (approximately 4 in.) in estimating flood depth based on comparing submerged objects in social media images with their predefined sizes, and Park et al. (2021) presented an MAE value of 6.49 cm (approximately 2.5 in.) by comparing visible parts of submerged vehicles with their estimated size. As summarized in Table IV-11, a comparison of the flood depth estimation error obtained in this research to previous studies indicates the reliability and generalizability of the developed technique in measuring floodwater depth with acceptable accuracy.

Table IV-11 Comparison of the results of this study with the literature on floodwater depth estimation.

Study	MAE	Method	Practical Considerations
Cohen et al. (2019)	18-31 cm (7-12 in.)	Augmenting DEM data for Coastal and riverine areas.	Challenges in obtaining high-spatial-resolution DEMs, high uncertainty in highly fragmented flooded areas.
Chaudhary et al. (2019)	10 cm (4 in.)	Submerged objects in social media images with their predefined sizes.	Assuming predefined sizes for different objects.
Park et al. (2021)	6.49 cm (2.5 in.)	Flooded vehicle images in ground-level view.	Finding submerged vehicles, assuming predefined sizes for different vehicles.
This study (Computer Vision Model I)	12.65 in. (32.13 cm)	Paired stop signs in crowdsourced photos, using pre-trained Mask R-CNN and line detection models. Tested on Blupix v.2020.1.	Computationally not efficient, challenges in pairing photos.

Table IV-11 Continued.

Study	MAE	Method	Practical Considerations
This study (Computer Vision Model II)	4.710 in. (11.96 cm) after tilt correction [4.737 in. (12.03 cm) before tilt correction]	Paired stop signs in crowdsourced photos, using a trained YOLOv4 model on an in-house dataset. Tested on Blupix v.2021.1 dataset.	Relies on citizen science as a means for data collection.

Model Validation on a Case Study

In this section, the model is validated in a case study of the 2021 flood in the Pacific Northwest was collected. During this flood event, the U.S. Geological Survey (USGS) stream gauge at Nooksack River in Ferndale, WA reported a peak stage height of 150.35 ft., indicating an increase of 5 ft. in water level (National Oceanic and Atmospheric Administration, 2021). The flood stage at the USGS Skagit River stream gauge near Mt. Vernon, WA was also rising above the major flood stage (32 ft.), logging 37 ft. of floodwater at this location (Center for western weather and water extremes, 2021), before being destroyed by flood debris (National Oceanic and Atmospheric Administration, 2021). To create the test set, 11 crowdsourced photos containing 3 stop signs in the U.S. state of Washington and 8 stop signs in the Canadian province of British Colombia are

web-mined. The locations of these stop signs are shown on the map in Figure IV-18. Each of the 11 post-flood images is first paired with its corresponding pre-flood photo (depicting the same stop sign), and then annotated with two classes of stop sign and pole. As stated before, the MAE for pole length estimation can be calculated as the average of the absolute difference between detected pole length and ground-truth pole length over N photos (including pre- and post-flood photos). The Computer Vision Model II obtains MAE of 3.916 in. and 6.769 in. for pole length estimation in pre- and post-flood photos of the test set, respectively. The MAE of flood depth estimation is 6.978 in. Table IV-12 shows the MAE achieved by the model for flood depth estimation for each photo in the test set.

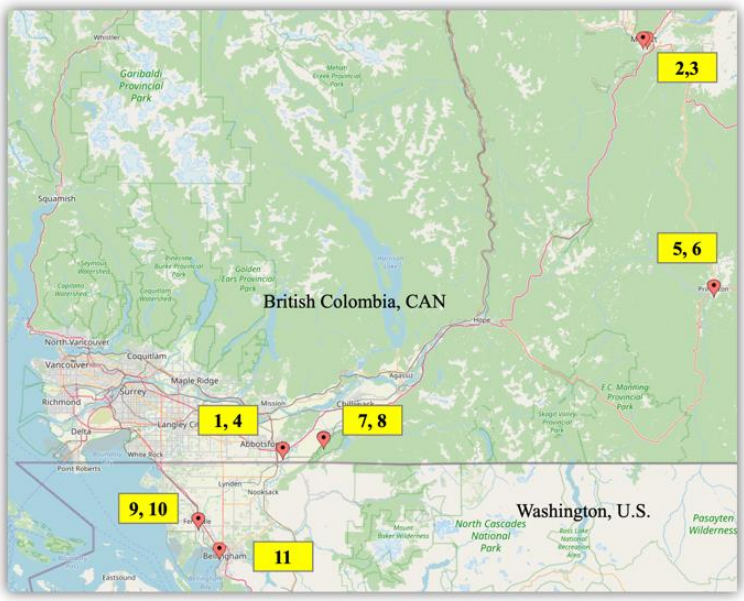

Figure IV-18 Map of 11 test data related to the 2021 Pacific Northwest flood (numbers refer to IDs shown in Table IV-12).

Table IV-12 Performance of the model on flood depth estimation.

ID	Location	Flood depth		
		Detection (in.)	Ground-truth (in.)	Δ (in.)
1	CAN/Abbotsford	25.486	27.162	-1.676
2	CAN/Merritt	13.949	9.759	4.190
3	CAN/Merritt	18.722	13.436	5.286
4	CAN/Abbotsford	20.292	20.157	0.135
5	CAN/Princeton	0.463	6.844	-6.381
6	CAN/Princeton	51.243	15.780	35.463
7	CAN/Abbotsford	4.871	3.968	0.903
8	CAN/Abbotsford	9.331	6.679	2.652
9	USA/Ferndale	44.342	41.342	3.000
10	USA/Ferndale	26.217	10.923	15.295
11	USA/Bellingham	9.820	8.038	1.782
	MAE			6.978

Techniques to Overcome Other Challenging Cases

Model training on street view images poses unique challenges that need to be addressed to improve the outcome. One such issue occurs when the model detects more than one stop sign in the input image, with one appearing closer to the viewpoint and other(s) at a

farther distance, as shown in Figure IV-19(a). While the object detection model is robust enough to detect multiple stop signs, the problem arises since each photo bears only a single geolocation tag which, by default, is used to map the detected stop sign. In the presence of multiple detected stop signs, however, this one-to-one correspondence will no longer be valid. To remedy this problem, when multiple stop signs are detected, the largest stop sign (appearing closest to the camera viewpoint) is selected as the target output. Among detected poles, the one with the closest center of x coordinates to the center of x coordinates of the candidate stop sign is then selected as the target pole.

(a)

(b)

text.

Figure IV-19 Demonstration of challenging cases in post-flood photos: (a) multiple detections (base photo courtesy of Steve Zumwalt/FEMA), and (b) reflection in water (base photo courtesy of TSGT Mike Moore, USAF).

Another challenge is reflection in water, which is a common problem in object detection. Simple solutions for reflection removal are based on the analysis of multiple input images, including pairs of images that are taken from different orientations, or with different polarizations (Naejin Kong et al., 2014; Sarel & Irani, 2004). By comparison, single-image reflection removal is more challenging. Wan et al. (2016) proposed a multi-scale depth of field (DoF) strategy to classify edge pixels and remove reflection in the image background (Wan et al., 2016). Fan et al. (2017) addressed the reflection issue using a deep learning model that extracts edge information to identify low-level vision tasks, and demonstrated high quality layer separation (Fan et al., 2017). Specifically in the post-flood image dataset, there are several cases where the stop sign is reflected in water, as shown in Figure IV-19 (b). To remedy this, the strategy is to not label the reflected stop sign and pole, thus forcing the model to learn from the difference between color intensity of pixels in actual and reflected objects.

Designing an Evacuation Decision Support Platform Based on the Identified Needs

To enable large scale crowdsource data collection, a crowdsourcing application was developed, named Blupix, using web-based GIS. The backbone of this platform is a CNN architecture that estimates the depth of floodwater in user-contributed photos by detecting stop signs and comparing pole lengths in pre- and post-flood photos of the same sign. Figure IV-20 illustrates the graphical user interface of Blupix, which gives users the ability to upload images of flooded stop signs, and view previously uploaded photos that are either paired (with corresponding pre-flood images of the same sign) or unpaired. Each photo pair also displays the calculated floodwater depth at the location of the stop sign.

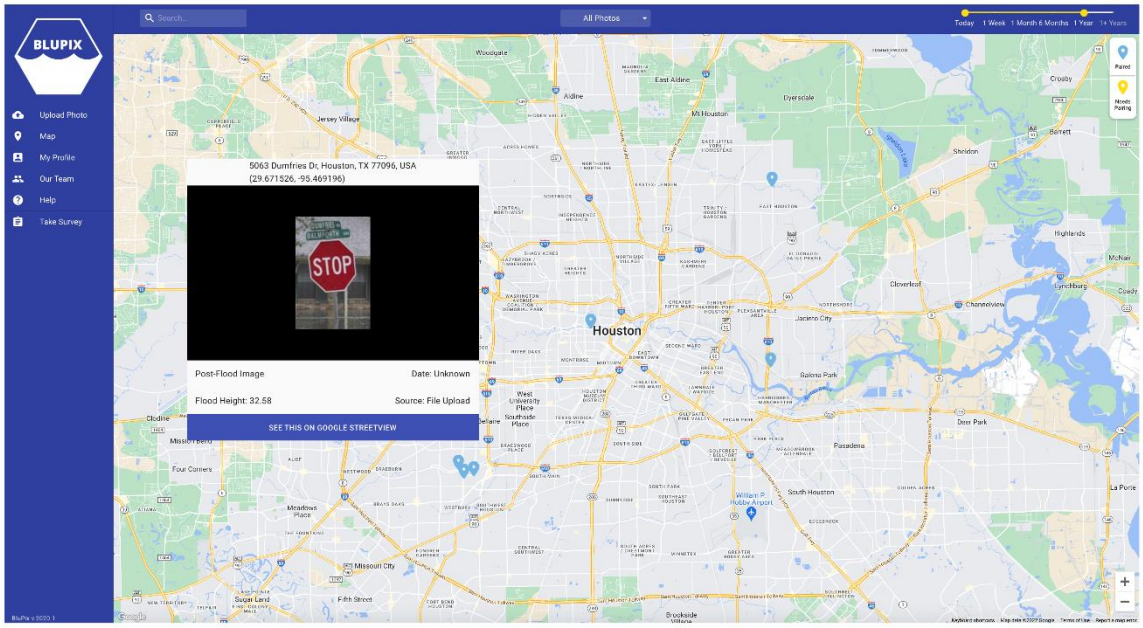

Figure IV-20 The graphical user interface of the Blupix crowdsourcing application.

To host the Blupix application, an advanced cyberinfrastructure was developed using container technology. As shown in Figure IV-21, the Model View Controller (MVC) software design pattern was used, where the *View* displays information (e.g., user profile, flood information, collected stop sign images), and the *Controller* processes the users' connection. The user interface is developed using a modern front-end framework named React J.S. (a.k.a., React). Once the React application is developed and ready to deploy, a Webpack middleware is designed to bundle the entire system to a set of static assets, significantly reducing loading time on the browser for viewing the application (Ruby et al., 2020). Unlike traditional web development technologies such as HTML and JavaScript, React supports large and complex web development with seamless data manipulation without subsequent page refreshes when users view dynamic pages (Aggarwal, 2018).

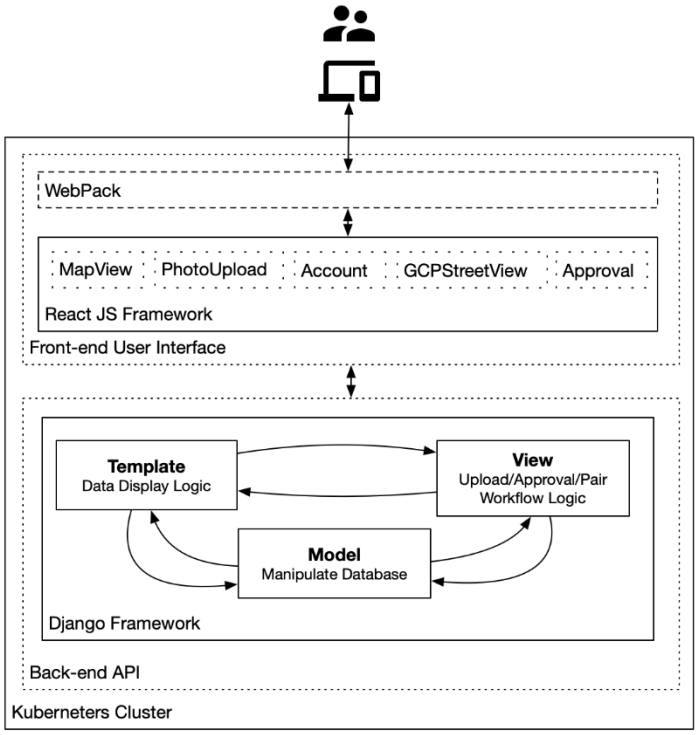

Figure IV-21 The Model View Controller (MVC) framework of the Blupix crowdsourcing application.

Except for back-end and front-end modules deployed on a Kubernetes Cluster, several cloud-native services were adopted to support the application development (Figure IV-22). The front-end components construct the requests made by users and send them to the Google Cloud Platform (GCP). Next, the components render the user interface based on the response received from GCP. A PostgreSQL database is designed to support a back-end server to store relational data (e.g., user profile, flood height, flood date). However, non-relational data in the image cannot be easily stored in PostgreSQL. Thus, after converting the image data to binary data, Microsoft Azure was integrated to store large amounts of unstructured pre-flood and post-flood data. The last part of this software

architecture consists of a Docker Hub to mount the code. With this image library, a development automation workflow was built to speed up the application deployment.

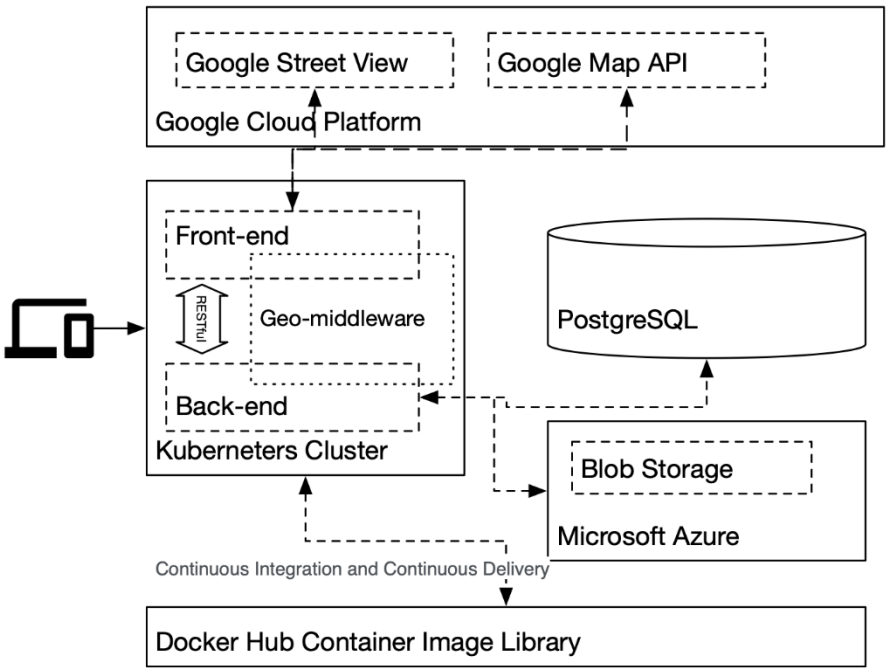

Figure IV-22 Illustration of the system architecture of the Blupix crowdsourcing application.

The Blupix app has the following pages: “Upload Photo”, “Map”, “Approval”, “My Profile”, “Our Team”, “Help”, and “Take Survey”. Using the “Upload Photo” page, users can upload a photo of a flooded traffic signs (post-flood photos). Figure IV-23 illustrates the process of uploading and pairing crowdsourced photos on the Blupix app. By knowing the location of the photo, user can find the same traffic sign (pre-flood photos) using the GSV API enabled in the app and pair it with the post-flood photo, and then upload it. The paired photo will be manually reviewed by admin (the author) to make sure the uploaded

data is appropriate and accurate (using the “Approval” page which is specifically available for the admins). Upon approval, the paired photo will be shown as a pin on the map (available in the “Map” page). Users can also create an account in the Blupix app (“My Profile” page) although it is not necessary to have one to be able to upload a photo. The “Help” page contains instructions on the photo requirements (stop sign in full view, waterline in view, and pole fully visible) and uploading process. More information about the Blupix team is also provided on the “Our Team” page. Lastly, using the “Take Survey” page, users will be guided to take the community needs assessment survey which was covered in Chapter III. Collected paired photos are analyzed using the developed Computer Vision Model II to estimate flood depth, and are added to the pins on the map to generate a flood depth map.

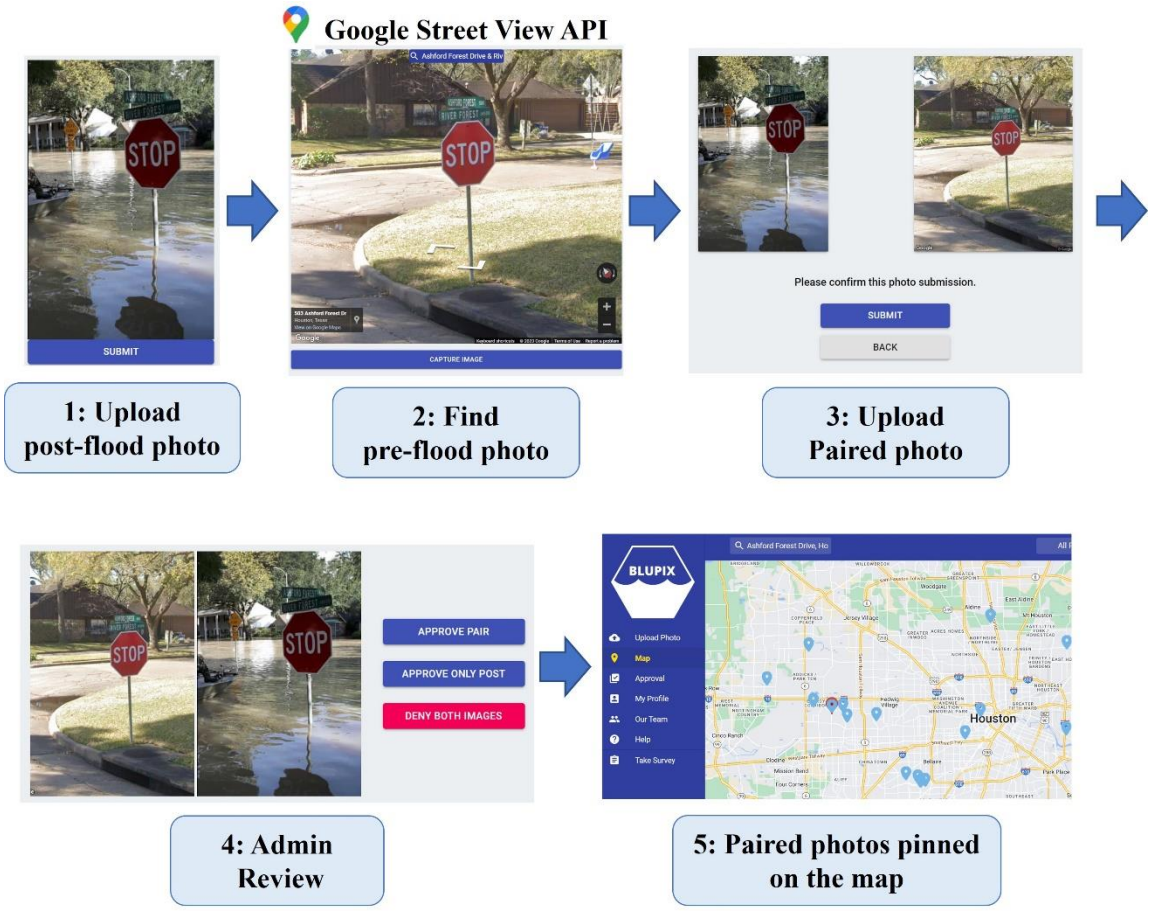

Figure IV-23 Uploading and pairing crowdsourced photos on the Blupix app.

Summary and Conclusion

Flooding is one of the most prevalent natural hazards that results in significant loss of life, and disrupts properties and infrastructure. Due to the constant change in water levels on the road network during a flood, reliable and real-time flood depth information at the street level is critical for decision-making in evacuation and rescue operations. Current methods of obtaining flood depth (including water gauges, DEMs, hydrological models, and SAR imagery) often suffer from shortage of data, inherent uncertainties, high installation and maintenance costs, and the need for heavy computing power. Recent advancements in

computer vision and AI have created new opportunities for remotely estimating the flood depth based on comparing submerged objects with their predefined sizes. In this part, a deep learning approach, based on the YOLOv4 architecture, was proposed for estimating floodwater depth in crowdsourced street photos using traffic signs. Since traffic signs have standardized sizes, the difference between pole lengths in paired pre- and post-flood photos of the same sign can be computed and used as the basis for estimating the depth of floodwater at the location of the sign. An in-house training set comprising web-mined photos and photos extracted from the Microsoft COCO dataset, was used for training the YOLOv4 model. To generate ground-truth information, all images were manually annotated by the author using an annotation software. However, in the future direction of this research, the annotation process itself can be also crowdsourced using online sources (e.g., Amazon Mechanical Turk (MTurk) or AI-enabled labeling software), to attain larger training sample size. The trained model was then validated using 5-fold cross validation, and subsequently tested for flood depth estimation on 163 paired photos from our in-house test set. Results indicate an MAE of 1.723 and 2.846 in. for pole length estimation in pre- and post-flood photos, respectively, and an MAE of 4.710 in. for floodwater depth estimation. Also, the performance of the proposed model surpassed that of two baseline approaches (dummy method I, which returns the average pole length of all images in the training set for each image in the test set; and dummy method II, which calculates the running average of pole lengths in all previously seen images in the test set). In addition, a tilt correction method was developed to minimize the pole length estimation error in paired photos of stop signs with uneven degrees of tilt. The model's performance was also

evaluated on 11 crowdsourced photos taken during the Pacific Northwest flood in 2021 which achieved the MAE of 6.978 in. To enable large-scale data collection, a crowdsourcing application (called Blupix) was designed. The Blupix app enables users to upload photos of flooded traffic signs and pair them with the same traffic sign before the flood using the built-in GSV API. Then all crowdsourced photos were analyzed with the Computer Vision Model II to estimate flood depth and used to generate a flood depth map.

CHAPTER V [5]

HUMAN-CENTERED FLOOD MAPPING AND INTELLIGENT ROUTING THROUGH AUGMENTING FLOOD GAUGE DATA WITH CROWDSOURCED STREET PHOTOS

The first motivation of this Chapter was to generate high spatial resolution flood maps for intelligent routing in and around residential neighborhoods by incorporating user-contributed flood photos. Two route optimization approaches were proposed in this Chapter and their effectiveness were assessed on sample test data. In the second approach (enhanced approach), floodwater depth data obtained through the visual analytics of crowdsourced photos were augmented with live stream flood gauge with the goal of improving the quality of evacuation routing optimization. In the second part of this Chapter, a mobile app was developed to calculate flood water depth using geolocated photos of submerged stop signs with the goal of providing ad-hoc situational awareness for people through a simple, reliable, and affordable mobile platform.

---

[5] Some of the materials presented in this chapter have been previously appeared in the following publications by the author:
Alizadeh, B., Li, D., Hillin, J., Meyer, M. A., Thompson, Courtney M., Zhang, Z., and Behzadan, A. H. (2022). Human-centered flood mapping and intelligent routing through augmenting flood gauge data with crowdsourced street photos. Advanced Engineering Informatics 54 (2022): 101730. https://doi.org/10.1016/j.aei.2022.101730
Alizadeh, B., & Behzadan, A. H. (2022). Blupix: citizen science for flood depth estimation in urban roads. In Proceedings of the 5th ACM SIGSPATIAL International Workshop on Advances in Resilient and Intelligent Cities 16-19. Seattle, Washington. https://doi.org/10.1145/3557916.3567824
Alizadeh, B., Li, D., Zhang, Z., & Behzadan, A. H. (2021). Feasibility study of urban flood mapping using traffic signs for route optimization. EG-ICE 2021 Workshop on Intelligent Computing in Engineering 572-581. https://doi.org/10.48550/arXiv.2109.11712

Route Optimization for Intelligent Wayfinding in Flood Events

Evacuation planning is a major component of flood management as it guides the movement of people and goods from at-risk places to safe areas (Cova & Johnson, 2003; Stepanov & Smith, 2009). In recent studies, optimization- and simulation-based models have been used for evacuation routing (Lim Jr et al., 2013). Flood evacuation has been increasingly recognized as being a critical component of disaster management adaptation to floods (M. He et al., 2021). Previous research has particularly focused on formalizing the evacuation process into different stages including the warning stage, withdrawal stage, and shelter stage, and finding separate solutions to each stage (Gomes & Straub, 2017; M. He et al., 2021). However, recent research by Insani et al. shows that complex evacuation solutions may not work well in no-notice or short-notice evacuation situations that could occur immediately after a disaster strikes (Insani et al., 2022). As there is only limited information (e.g., velocity and spread of floodwater movement) within a short response time, researchers have also considered interpolation techniques (Viavattene et al., 2022; X. Wang et al., 2017) or buffer decay function (X. Huang et al., 2018) to compensate for limited data and support large-scale flood mapping. To date, however, the literature on interpolation techniques for flood mapping in real-world route optimization scenarios is limited. Stepanov and Smith (Stepanov & Smith, 2009) utilized multi-objective route optimization and M/G/C/C state-dependent queuing networks to minimize travel time, distance, and traffic delays. In another study, single-objective optimization and evacuation simulation were used to maximize the number of evacuees and minimize travel time during flood events (Huibregtse et al., 2010). Researchers have also utilized route

optimization and CPLEX, a high-performance optimization software, to optimize evacuation time and route for no-notice evacuation of transit-dependent citizens (Sayyady & Eksioglu, 2010).

The routing problem is one of the most studied combinatorial optimization problems, first mentioned in 1959 as the "truck dispatching problem" to determine an optimal route for a fleet of gasoline delivery trucks between a terminal and several service stations (Dantzig & Ramser, 1959). One important variant of the routing problem is emergency evacuation planning (Lu, 2006), which aims to evacuate residents from a hazard-inundated region to a safe place in the shortest possible time and on the safest path. In this work, a flood depth map is generated using the stop sign flood depth data. To overcome data scarcity in the flood depth map generation, a distance decay function can be applied using a Gaussian buffering function to approximate floodwater depth in areas surrounding a point with field-verified floodwater depth reading (Alizadeh et al., 2021). Previous work has utilized various interpolation methods to map flood hazard. Berens et al (Berens et al., 2021), for instance, used the inverse distance weight method to plot the flood map in a riverine area. Another common way to plot a flood map is the kriging interpolation method (Chokmani & Ouarda, 2004; Marche et al., 1990; Sun et al., 2000). For example, Nezhad et al. (Nezhad et al., 2010) used residual kriging with flood gauge data to estimate regional flood frequency. In another study, Zhang et al. (K. Zhang et al., 2019) used empirical Bayesian kriging to interpolate ground pixels for mapping the digital terrain model (DTM) for flood vulnerability mapping.

Proposed Methodology for Using Enhanced Flood Depth Data for Risk-Informed Route Optimization

In this research initially a flood depth map is generated using AI-calculated flood depth using stop sign data and then an A* search algorithm is used for route optimization. Later, the flood depth map generation is improved by augmenting flood gauge data with AI-calculated flood depth data and then the Dijkstra route optimization is utilized for intelligence wayfinding.

Routing Approach I: Flood Depth Mapping Using Stop Sign Data and Route Optimization Using A Search Algorithm*

Simulate Flooded Areas Using GIS and Stop Sign Detection Results.

Volunteered Geographic Information (VGI) has been utilized in flood studies (Goodchild, 2009; X. Huang et al., 2018). Huang et al. (2018) used an inverse distance weighted height filter to build a probability index distribution (PID) layer from the high-resolution DEM data (X. Huang et al., 2018). Inspired by that work, a distance-decay function was used along with isohypse information to transform point-by-point floodwater depth data into area-wide flood inundation maps. Several forms of this function are widely used to describe systematic spatial variations where spatial information has the tendency to vanish with distance (Haining, 2001). In this research, a flooding confidence area is created around detected floodwater depth points to simulate flooded regions. In the future, this approach can be compared and validated using hydrological-based modeling (Y. Liu et al., 2006) to improve the accuracy of flood inundation mapping. Suppose an estimated flooded area A that is defined by a discrete point grid $\{X\_1, X\_2, \ldots, X\_i\ , \ldots, X\_j\}$. The

Gaussian buffering function shown in Equation V-1 is applied to approximate the depth of floodwater at point X_j in area A. In this Equation, X_0 is the detected floodwater depth at the center point of area A, I_0 is the elevation at the center point of area A, I_j is the elevation in point j, d_j is the geographic distance between the center point of area A and X_j, and b is a fixed bandwidth for the Gaussian function. As the distance d_j varies around area A, the estimated floodwater depth also changes with distance-decay and isohypse information. This approach is commonly used in GIS research such as social-media flood mapping (X. Huang et al., 2018) and distance-decay weight regression model (Gutiérrez et al., 2011).

$$X_j = X_0 \, exp\,[-1/2(d_j/b)^2] + (I_0 - I_j) \qquad \text{Equation V-1}$$

Description of The Routing Problem.

Given the flood inundation information, the routing problem from an origin to a destination point can be modeled as a multi-stage decision process, where each decision stage includes the location of the current decision point as well as the time needed to complete the remainder of the process. The designed optimization-based algorithm proposes a routing solution that avoids flood inundated areas and supports search and rescue operations during a flood event. The routing problem is further modified by including several decision objectives, and transforming the otherwise single-objective optimization into a multi-objective decision process. From the taxonomy of navigation for emergency response (Z. Wang & Zlatanova, 2013), this problem can be defined using $X = < X\_1, X\_2, X\_3, X\_4, \ldots >$, where X_i denotes an environment factor, and contains the quantity (one or many), and the type (e.g., destination, responder object, obstacle) of that

factor. For example, for a person whose goal is to go back home while avoiding flooded roads, the navigation route can be defined as $< \{one\ moving\ object\}, \{one\ static\ destination\}, \{one\ static\ obstacles\} >$. In this section, since the traditional Dijkstra algorithms may not work well for X that contains obstacle factors, using the A* search algorithm (Lerner et al., 2009; Russell & Norvig, 2002) was proposed. For this purpose, the following concepts are adopted before each iteration of the A* search algorithm were formalized as:

1. Search area: Given a prepared base map that contains spatial entities, each entity is represented as a graph node in the search area.
2. Open vs. closed list: All nearest nodes waiting to be searched are stored in an open list; and those already searched are stored in a closed list.
3. Path sorting: To define the direction of the next movement, a path sorting function was used, expressed by Equation V-2.

$$F(n) = G + H \qquad \text{Equation V-2}$$

In this Equation, H denotes a heuristic function, and G is the moving cost from the initial location to the next node in the open list. The heuristic function takes the Manhattan distance to calculate the cost of moving from each of the candidate next nodes in the open list to the final destination node. Figure V-1 presents the pseudo algorithm for the A* search. A demonstration of how this algorithm is used in a flooded area (routing with obstacles) is shown in Figure V-2. In this Figure, different shades of blue represent different floodwater depth values, diamonds stand for start and destination points, and orange pixels mark the simulated routing path. The cost value is displayed in each searched

pixel. This information is used as threshold conditions to check whether a vehicle can pass through a particular area.

```
Initialize open_list and close_list, start with initial point;
Add start node s to open_list;  F(s) = 0 (smallest);
If open_list is not Null, select node n with smallest F(n):
  If n is destination node:
    Find parent node from destination node to start node then return;
  If n is not destination node:
    Move n from open_list to close_list;
    Traverse eight nearest nodes of n:
      If nearest node m in close_list: continue;
      If nearest node not in open_list:
        Set parent node n for m; Update cost function; add m to open_list
Connect parent node from initial node and generate path;
```

Figure V-1 Pseudo algorithm for A* Search.

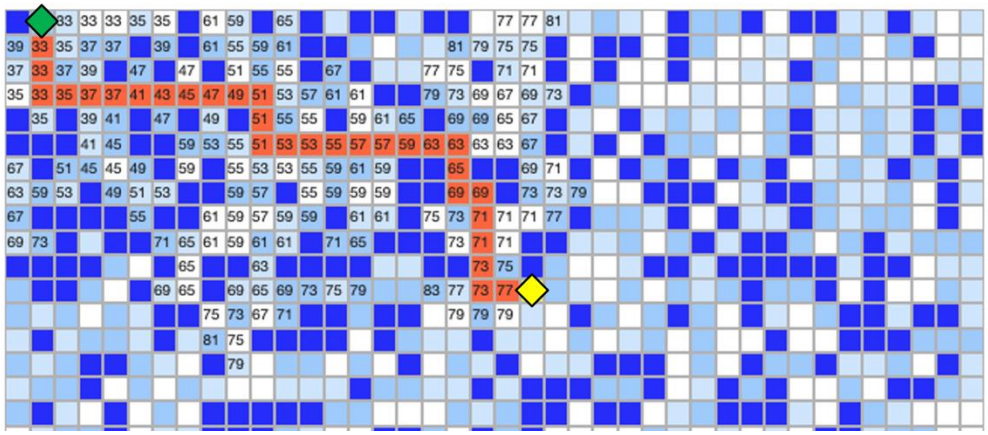

Figure V-2 sample output of A* Search algorithm with obstacles.

Results and Discussion

Case Study Description

As shown in Figure V-3, for the flood scenario presented in this part, six paired photos from the 2017 Hurricane Harvey in Houston, Texas, taken approximately on the same date in the month of September, are selected from BluPix v.2020.1, a crowdsourcing platform developed in this research to collect user-contributed photos of flooded stop signs.

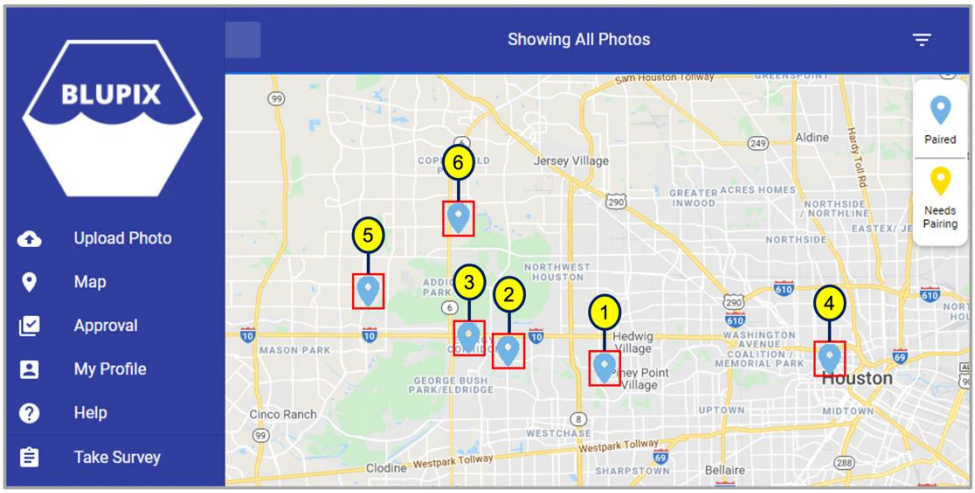

Figure V-3 locations of selected paired flood photos in Houston, TX after Hurricane Harvey (2017).

Calculation of Flood Depth Using Sample Photos of Stop Signs

Table V-1 shows a summary of floodwater depth calculations applied to pre- and post-flood photos. As shown in this Table, the RMSE of the flood depth estimation model on the six pairs of pre- and post-flood photos is 4.69 inches, and the average processing time for floodwater depth calculation is 11.6 seconds.

Table V-1 Performance of floodwater depth estimation on paired pre- and post-flood photos.

Calculation	Metric	Pre-flood photos (n = 6)	Post-flood photos (n = 6)
Stop sign detection	Intersection over union (IOU) %	96.73	95.24
	Precision %	100	100
	Recall %	100	100
	Average precision (AP) %	100	100
	Average processing time (s)	1.08	1.26
Pole detection	RMSE (in.)	2.64	5.80
	Average processing time (s)	0.13	0.10
Flood depth estimation	Average total processing time (s)	2.57	
	RMSE (in.)	4.69	

Implementation of Flood Depth Mapping and Route Optimization on Sample Photos

Floodwater depth estimates are subsequently used to generate a flood inundation map with depth grids. Figure V-4 demonstrates the application of A* search algorithm to calculate the shortest flood-free route. In this example, each of the previously selected six paired points is taken as the central point of a flooded area. To implement the distance-decay function (Equation V-1), elevation data is queried from Google Elevation API. The Graphhopper library (Karich & Schröder, 2014) is used for route search, and

Openrouteservice is utilized to overlay the base map with generated flooded areas. The basic spatial information for building the base map is taken from OpenStreetMap (Planet OpenStreetMap., 2021).

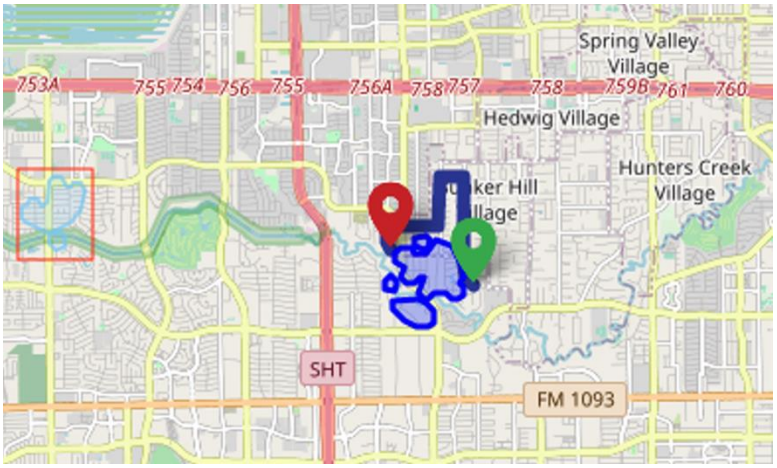

Figure V-4 Illustration of the routing algorithm using buffered points that represent estimate floodwater depths collected from inundated areas.

Routing Approach II: Flood Depth Mapping Using Augmented Stop Sign Data with Flood Gauge Data and Route Optimization Using Dijkstra Routing Algorithm

In this section, the Dijkstra routing algorithm (Dijkstra, 1959) is applied to calculate a flood-free evacuation route. To this end, a flood risk map is first built for route optimization by overlaying gauge data with floodwater depth data. Generally, values between two closely located points can be predicted through point interpolation. The accuracy of this interpolation, however, is affected by the sparseness of the interpolation points. Using stop sign points in addition to gauge data can enhance the density of interpolation observations. Empirical Bayesian Kriging (EBK) (Krivoruchko, 2012) was

used as a geospatial interpolation method to generate a flood risk map for route optimization. EBK is different from other kriging methods as it reduces the tendency to attain the overall mean value of variables and allows large deviations for predicted values over space (Gupta et al., 2017). Spatial autocorrelation (i.e., increasing similarity of spatial features with decreasing distance) is assumed in all geostatistical methods (Goodchild, 2009). Particularly, EBK was utilized with semivariogram to evaluate the diminishing similarity among flood data points over distance (Gupta et al., 2017). Equation V-3 is used to interpolate flood depth values for gauge points and stop sign points using the EBK method with a power semivariogram model. In this Equation, h is the distance, a and b are positive constant parameters, and n denotes the parameter of nugget effect as an intercept of variogram function. The parameters in Equation V-3 are estimated by restricted maximum likelihood (REML) (Krivoruchko, 2012).

$$\gamma(h) = n + b|h|^a \qquad \text{Equation V-3}$$

According to the EBK implementation by Krivoruchko et al. (Krivoruchko, 2012) the main kriging method can be simplified as in Equation V-4, where *K* denotes the number of observation points, z_i is the observation point in location s_i, $y(s_i)$ is the transformed Gaussian in the same location, ϵ_i is the normally distributed measurement error of z_i, and function $t(\cdot\,|\Theta)$ is a transformation to Gaussian process with parameter Θ. EBK estimates the semivariogram through repeated simulations of residuals (Giustini et al., 2019).

$$z_i = t^{-1}(y(s_i) + \epsilon_i|\Theta) = z(s_i) + {\epsilon_i}^2, \qquad i = 1 \dots K \qquad \text{Equation V-4}$$

Results and discussion

Case Study Description

To demonstrate the applicability of the proposed methodology, 20 paired photos is selected, uploaded on the Blupix app, that were taken during Hurricane Harvey (August 27 – September 1, 2017) in Houston, Texas. These photo pairs are then analyzed by Computer Vision Model II (the trained YOLOv4) model for floodwater depth estimation. In addition to stop sign data, gauge data are leveraged to compute flood depth for the areas without paired stop sign photos, and to demonstrate our interpolation method and routing algorithm. The gauge height (a.k.a., stage) is the height of the water in the stream above a reference point, and refers to the water surface elevation in the specific pool or low-lying terrain near the gauge station. For our experiment area, the gauge records in all 1,321 gauge stations in Texas are scraped via the National Weather Service (National Oceanic and Atmospheric Administration, 2022). The average gauge height is calculated by comparing the gauge heights during Hurricane Harvey and the annual mean gauge heights of other years during the same time period of August 27 to September 1, 2017.

Calculation of Flood Depth Using Sample Photos of Stop Signs

The mAP of the model on the validation set is calculated as 97.04%, by taking the average mAP in each of the five training sets. The optimum number of iterations obtained (when the highest mAP is achieved) is 3,000, which is equal to the average number of optimum iterations in the five training sets. The AP of the model on test data (20 paired photos) is calculated as 100% and 96.54% for the stop sign and pole classes, respectively. The MAE for floodwater depth estimation is 3.80 in. Results are summarized in Table V-2.

Table V-2 Performance of the trained YOLOv4 model on 20 selected paired photos in Hurricane Harvey (August 27 – September 1, 2017) in Houston, Texas (S=stop sign; P=pole).

Metric	Class	Pre-flood (*n* = 20)	Post-flood (*n* = 20)	All photos (*n* = 40)
Average IoU (%)	S+P	83.10	79.69	81.44
Precision @ 0.25 conf (%)	S+P	93	93	93
Recall @ 0.25 conf (%)	S+P	100	95	98
AP (%)	S	100	100	100
	P	100	92.30	96.54
mAP @ 0.50 (%)	S+P	100	96	98.27
Average detection time (sec)	S+P	0.10	0.10	0.10
MAE of pole length estimation (in.)	P	2.73	2.64	3.80

Flood Map augmentation Using Stop Sign Data and Gauge Data

Using ArcGIS API for Python (ArcGIS Developer, 2021), a comparison experiment is created with gauge only and gauge and stop sign floodwater depth data. Contour lines are used to represent variations in interpolated flood depth values. The changes between those contour line intervals are assumed to be consistent, where each class follows a geometric

series with approximately the same number of interpolated flood depths. Figure V-5 demonstrates the distribution of stop sign points and gauge points used in this experiment.

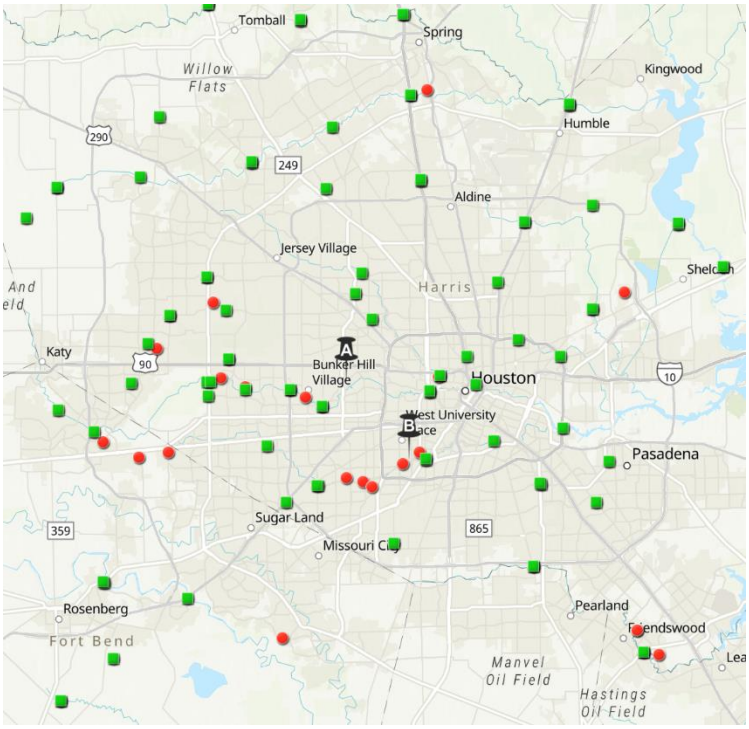

Figure V-5 Location of start and end points (black pins), flood gauges (green squares), and stop sign points (red circles) in the experiment area.

Figure V-6(a) shows the calculated route under the non-flood scenario obtained by regular Dijkstra routing, while Figure V-6 (b) and Figure V-6 (c) show optimized evacuation paths with flood depth consideration using EBK and Dijkstra algorithms simultaneously. For best comparison, Figure V-6 (b) is calculated with only flood gauge data, and Figure V-6 (c) shows the resulting route when stop sign data is added to flood gauge data. To ensure date/time consistency between flood gauge data and stop sign data, time information retrieved from metadata of flooded stop sign photos is used to query flood gauge data (National Weather Service Team, 2021). The highlighted blue polygons in Figure V-6

represent the estimated flooded area, and thick dark blue lines represent suggested routes under no-flood and flood scenarios. Using a 100-inch distance threshold for avoiding flooded areas, the optimized evacuation path with only gauge data, shown in Figure V-6 (b), conservatively detours several potentially high flood risk areas before reaching the destination safely. In contrast, the route shown in Figure V-6 (c) generated using the EBK method is a shorter (yet still safe) alternative. Table V-3 compares the three routes considering the estimated travel time (driving) and distance obtained using ArcGIS API. Each column represents a routing scenario corresponding to Figures V-6 (a), (b), and (c). As shown in this Table, using only gauge data will increase the user's travel time and distance, possibly exposing them to more flood risk over time (since floodwaters move).

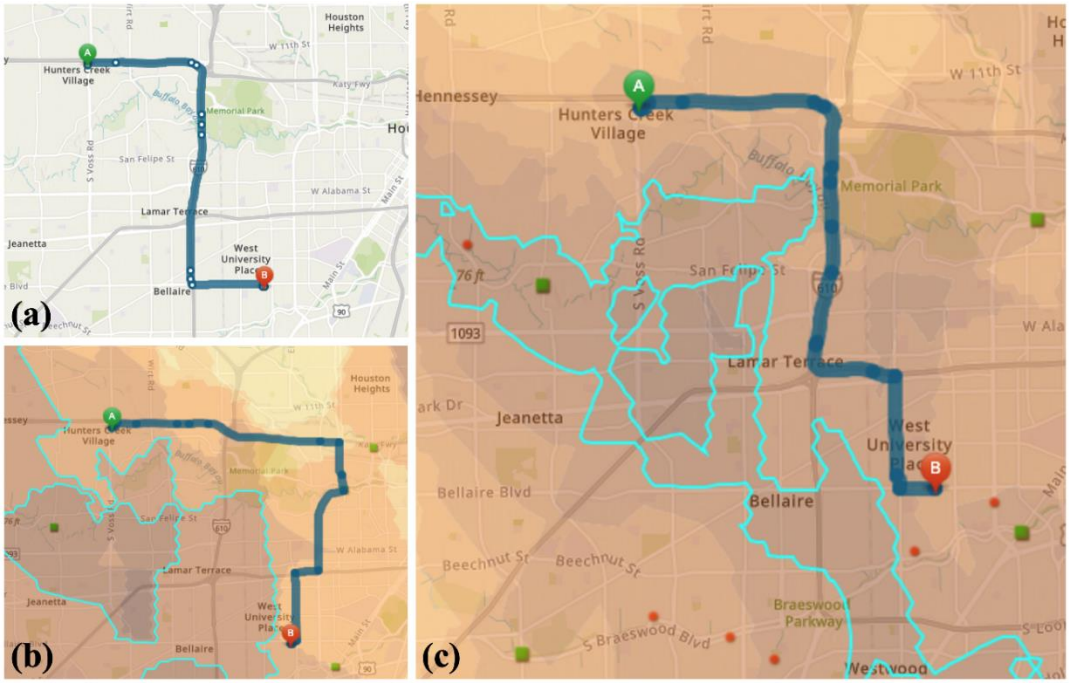

Figure V-6 Flood mapping and risk-informed evacuation route optimization using EBK and Dijkstra algorithms: (a) regular route planning with Dijkstra algorithm; (b) EBK method with Dijkstra algorithm using only flood gauge data; (c) EBK method with Dijkstra algorithm using flood gauge data and stop sign data.

Table V-3 Comparison of three routing scenarios in the experiment area.

Metric	A	B	C
Estimated travel time (driving) (min.)	22	26	22
Total travel distance (miles)	9.99	11.53	9.60

Mobile Device Implementation for Ad-hoc Situation Awareness.

Background

As mentioned earlier, citizen science and crowdsourcing have the potential to contribute to increasing the spatial and temporal availability of flood depth information for disaster response and management (See, 2019). Moreover, crowdsourced data collected in a flood event can be used to improve situational awareness, decrease response time, and assess the severity of the damage. Crowdsourcing or citizen science refers to the involvement of ordinary people in parts of a scientific process such as data collection (See, 2019). In recent disaster events, the public has already vastly utilized social media platforms such as Twitter and Facebook to share disaster-related information such as photos, videos, or texts (Saroj & Pal, 2020). Several researchers have developed customized crowdsourcing data collection platforms for disaster response and mitigation. GISCorps, for example, is a crowdsourcing platform for collecting and mapping photos of disaster-affected areas (Saroj & Pal, 2020). Crowd4Ems is another crowdsourcing platform that uses data mining to estimate the geolocation of social media photos and videos of areas affected by earthquakes, and validates them with the help of volunteer users (Ravi Shankar et al., 2019). Another example is Sahana, which allows users to share disaster-related information and request help (Careem et al., 2006).

Effective information and communication technology (ICT) solutions consider communities' most critical needs while providing a simple and easy-to-use interface for collecting valuable information required for analysis. Current disaster-related crowdsourcing platforms enable data sharing and provide functionalities for informing

first responders and communities; however, the majority of these solutions do not provide instantaneous, on-demand information to the users.

Using Convolutional Neural Networks for Stop Sign Detection

Since most mobile devices have limited computing power and memory, employing flood depth estimation models on these devices necessitates using a lightweight object detection model. Therefore, this study develops a flood depth estimation model by training an EfficientDet03 on an in-house training set. EfficientDet is a lightweight object detection model designed by the Google Brain specifically for resource constrained edge devices, and can achieve high accuracy (Tan et al., 2020). EfficientDet uses the backbone of EfficientNet (Tan & Le, 2019) for extracting features from input images and a weighted bi-directional feature pyramid network (BiFPN) as the fusion layer for extracting the context information from those features. Several studies have implemented different versions of the EfficientDet network on mobile devices for real-time object detection. For example, in a study (Ulil et al., 2021), EfficientDet0 was utilized to detect and calculate the final answer of a handwritten equation which achieved an mAP of 63.17%, and an average accuracy (AP) of 81.9%. In another study (Ayachi et al., 2021), researchers trained EfficientDet0 model to detect drivers' fatigue by detecting eye closure and mouth yawning, yielding 96.05% accuracy on the test data.

In this study, considering the accuracy and speed tradeoff, EfficientDet03 in the TensorFlow Model Zoo was used. EfficientDet03, achieves an AP of 47.2% on the COCO dataset and 25B floating point operations per second (FLOPs) (Tan et al., 2020). This network is pre-trained on the ImageNet dataset (Russakovsky et al., 2015) and re-trained

on an in-house training set of 800 photos of stop signs (334 pre-flood photos of stop signs from the COCO dataset, 334 web-mined post-flood photos of stop signs and 132 zero-label photos of other traffic signs). The network was trained for 50 epochs with a batch size of 8, using TensorFlow Model Maker Library, achieving a detection loss of 0.051 and a class loss of 0.038. The training process took approximately 35 hours on an HP ZBook 17 G6 with 7 cores, 9850H CPU, 64 GB RAM, and Nvidia Quadro RTX5000 GPU with 16 GB memory. Subsequently, the model was converted to a TensorFlow Lite which is optimized to run on mobile devices.

Using Google Street View to Obtain Pre-flood Imagery of a Test Photo

In the developed methodology, in order to estimate the floodwater depth, a submerged stop sign photo needs to be visually compared with a photo of the same stop sign before the flood. To this end, GSV is used to obtain the pre-flood photo of stop signs in the test phase, given the geographical location of the post-flood photo. GSV is a commonly used online service which began in 2007 and covers approximately 10,000,000 miles of roads and streets across 100 countries and territories (Google, 2022). GVS images have been used in several studies in computer vision applications. As an example, in a study (Campbell et al., 2019), GSV images were utilized for traffic sign detection using SSD MobileNet. In another study (Ning et al., 2022), aerial and GSV images were used for extracting sidewalks using a trained You Only Look at CoefficientTs (YOLACT) model.

Mobile Device Implementation

The Android Studio version 4.2 was subsequently used to develop an Android app in Kotlin programming language to automate the process of taking a post-flood photo of a stop sign, geolocating the captured sign and finding its pre-flood view in GSV, running object detection on the photo pair, and estimating the floodwater depth at the location of the stop sign. In the developed app, when a user captures a camera image, the GPS location (longitude and latitude) and the azimuth angles (pitch and roll) of the mobile device are also obtained from the built-in accelerometer and magnitude sensors. The user is then directed to a GSV screen that displays an interactive view of the location of the sign, considering the GPS and angle readings of the camera device. As the user navigates in this scene by moving or rotating the view, or searches for a specific location, the latest positional information is queried from GSV and replaces the previously stored location of the camera. The Static API of GSV enables the user to capture a snapshot of the stop sign from the most desirable location and angle.

The next step is to determine the sign pole length in both pre- and post-flood images using the trained EfficientDet03. For each image, there are three APIs to load and run the object detection model: (1) Preparing the image (Tensor image), (2) Creating a detector object, and (3) Connecting 1 and 2. The captured image is decoded into the Bitmap format and passed to the object detection model. Using the Bitmap image as input, the object detector returns a list of detection results. The outcome is then filtered to retain only the detected stop sign and pole with a detection confidence higher than 50% threshold.

Next, using the “Calculate” button, the user will be asked to enter the real-world size of the stop sign (in a residential area, the user will enter 30 in., and in a non-residential area, the user will enter 36 in.). Giving this flexibility to the user in this version of the app will guarantee that the correct real-world size is used for calculating the inch-to-pixel ratio. Then, two pole lengths (one in the pre-flood photo and another one in the post-flood photo) are calculated and compared, to obtain an approximation of the floodwater depth. If stop signs or poles are not detected in either of the photos, the app will show the message: “Stop sign or pole is not detected.”. To avoid inaccurate results, if the pole is completely submerged in water, the app will not generate any outcome. Figure V-7 illustrates the schematic representation of the proposed approach. Figure V-8 demonstrates the Blupix mobile app interface along with a real example of flood depth estimation on a sample photo in Houston, Texas during Hurricane Harvey (2017) which calculated the flood depth of 20.79 inches.

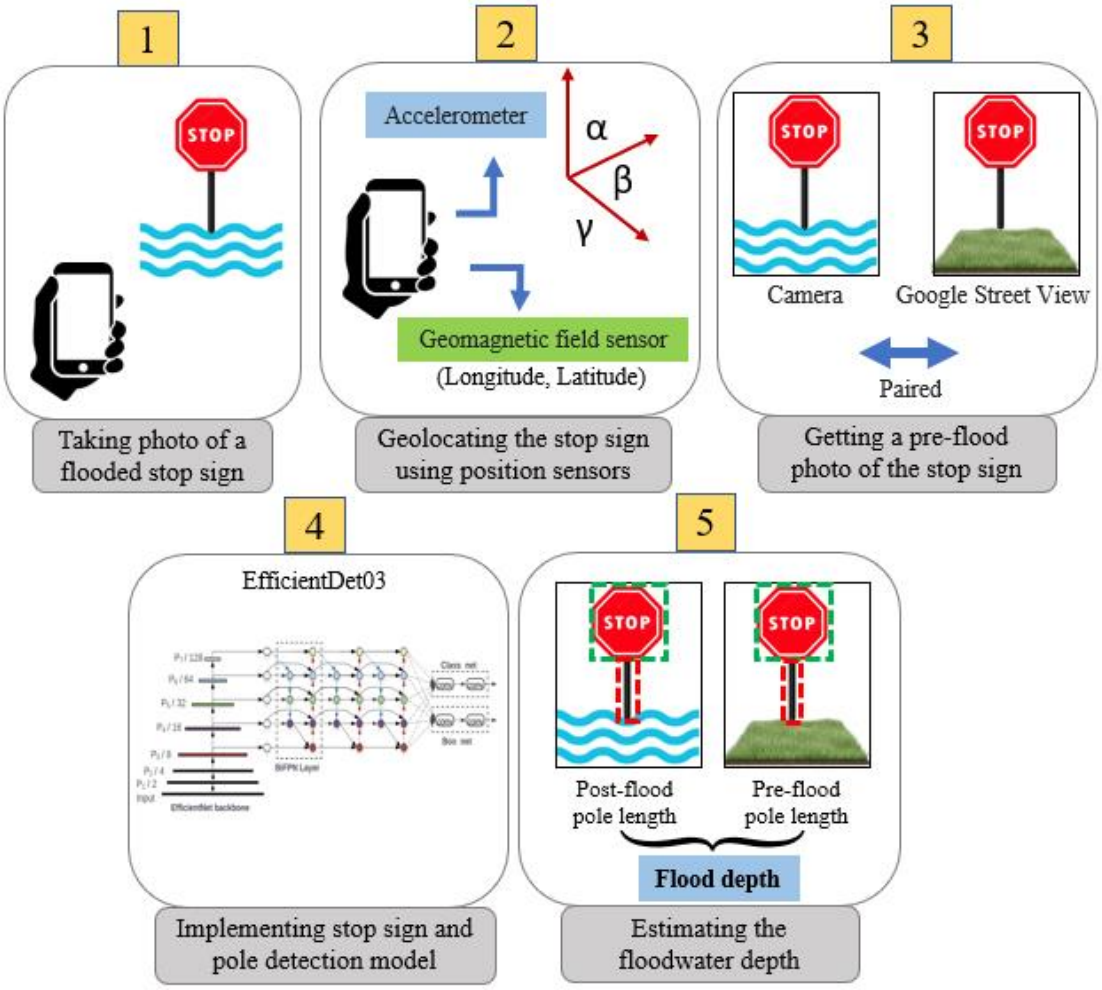

Figure V-7 Schematic representation of the Blupix app.

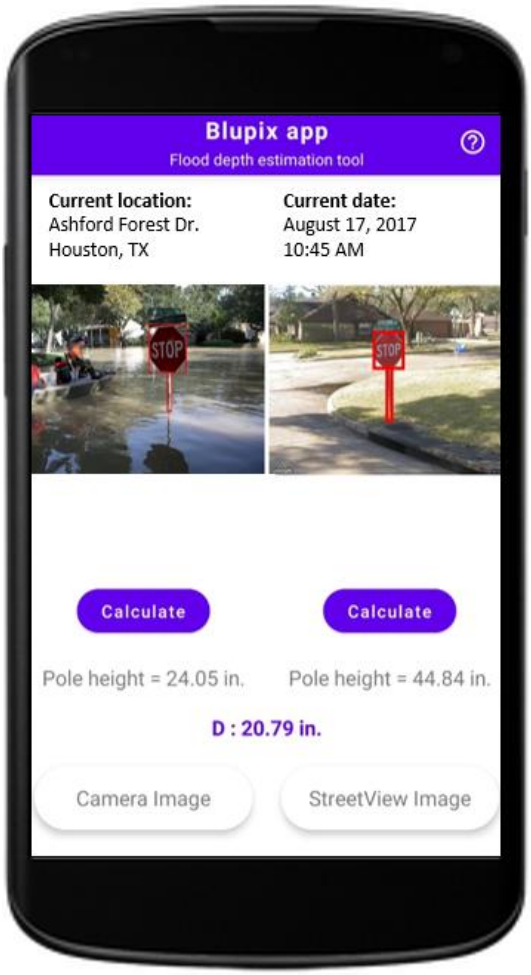

Figure V-8 Sample flood depth estimation on the Blupix app.

Blupix Preflood Crowdsourcing Platform

Following a few of the community meetings, it was identified that people have concerns about areas without GSV data and also mobile data connectivity interruption during floods. Thus, to enable the Blupix app to be implemented in offline mode, an additional crowdsourcing platform (called Blupix Preflood) was created specifically for the collection of pre-flood photos of stop signs. This platform allows users to upload photos of stop signs in their immediate surroundings which are then mapped onto the Blupix app's

map as crowdsourced pre-flood photos. The crowdsourced pre-flood photos are then used in combination with photos of flooded stop signs that are uploaded to the app when a flood occurs. This allows the app to pair the pre-flood photos with the newly uploaded flooded photos and instantly calculate the flood depth even in offline mode. The platform was designed with the aim of increasing the reliability of the app by eliminating the reliance on mobile data and enabling the app to function effectively even in areas with low or no network connectivity. This approach helps to ensure that the app can be used during flood emergencies, when mobile network connectivity is often disrupted or limited. Figure V-9 presents the interface of the designed crowdsourcing platform.

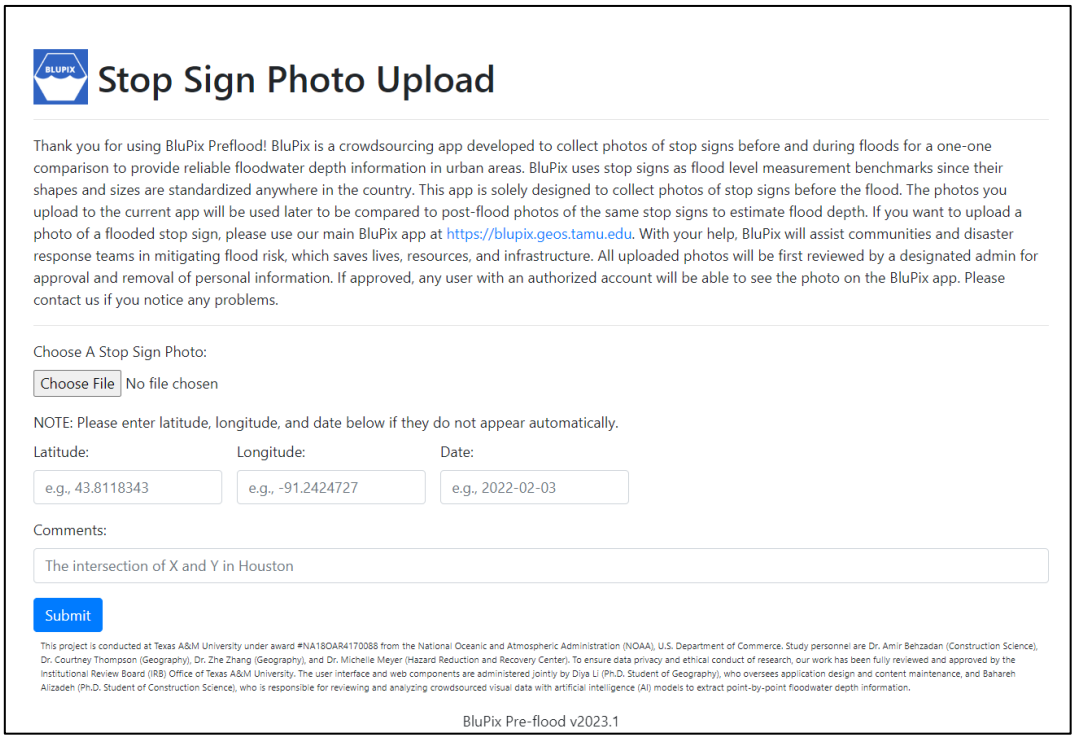

Figure V-9 The interface of the Blupix Preflood crowdsourcing application.

The Connection Between Blupix App, Blupix Mobile App, and Blupix Preflood App

This study developed three crowdsourcing platforms: Blupix, Blupix Preflood, and Blupix Mobile. Figure V-10 illustrates the connection between these three platforms. In this design, the Blupix app serves as the main platform, accessible via a dedicated website (https://blupix.geos.tamu.edu/), where people can upload photos of flooded traffic signs using their mobile devices or computers. Users can manually pair uploaded photos with corresponding pre-flood photos by entering the location of the traffic sign in GSV. The app admin reviews uploaded photos, and subsequently feeds them to a computer vision model for further analysis. The output of this step is the estimate of flood depth, which is also reported on the map alongside the pre- and post-flood photos of the stop sign. Given an uploaded photo pair, if only the post-flood photo is approved by the admin, only the post-flood photo will be pinned on the map which can be paired with the correct pre-flood photo later by the same or other users.

Blupix Mobile, on the other hand, is a mobile app that enables users to take a photo of a flooded traffic sign while the app automatically pairs it with the GSV view of the same traffic sign using GPS and accelerometer data of the mobile device. Upon the completion of the pairing process (which takes only a few seconds), the mobile app provides instant flood depth information through its built-in computer vision model. Users can also upload their paired photo with the calculated flood depth to a cloud database, which is then reviewed by the admin and pinned on the map. The Blupix Mobile app is available for

Android devices and can be downloaded from the research lab's GitHub page (https://github.com/ciber-lab/blupix).

Finally, Blupix Preflood is a crowdsourcing app for collecting pre-flood photos of stop signs prior to a flood event, accessible via a website (https://blupix-image.geos.tamu.edu/). Collecting pre-flood photos is useful for future pairing with post-flood photos in locations with limited GSV data or mobile data connectivity interruptions during floods. User-uploaded photos on this app are stored on a cloud database and pinned on the map as pre-flood photos. The app extracts the geospatial metadata of the uploaded photo (if any) to automatically populate the location field. If the metadata is not available, users should enter the location of the photo in the app. The app admin reviews all uploaded photos before they are pinned on the map.

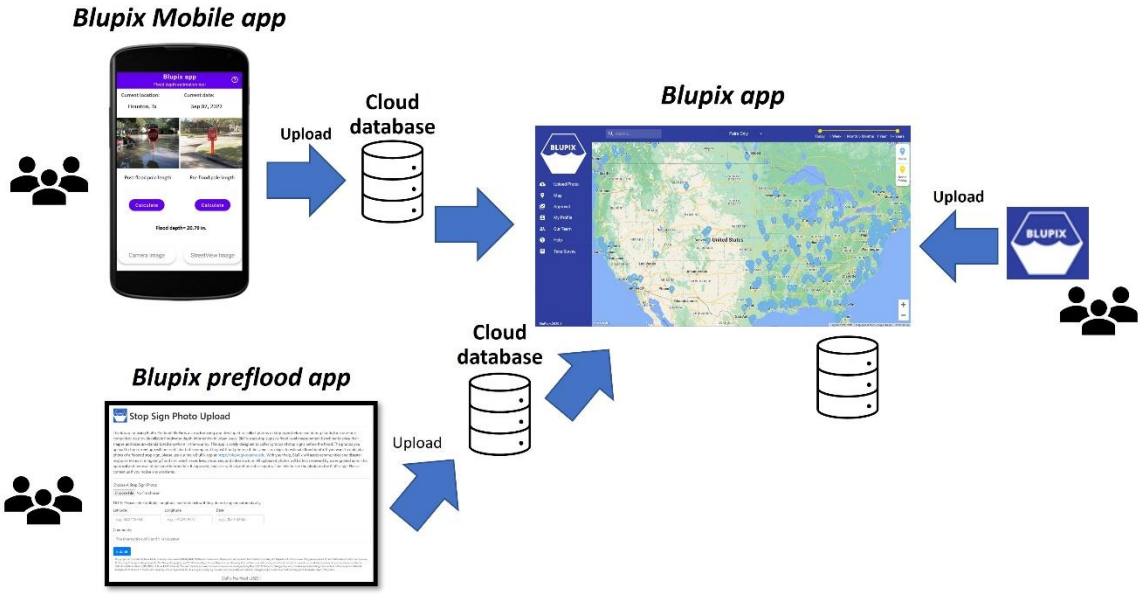

Figure V-10 The relationship and information flow between the Blupix app, Blupix Mobile app, and Blupix Preflood app.

CHAPTER VI

FLOOD RISK PERCEPTION ASSESSMENT USING VIRTUAL REALITY

Introduction

Informed decision-making during flood evacuation, search and rescue, and sheltering depends on the availability of reliable information about the depth of floodwater in affected areas. While underestimating the water depth can be catastrophic, overestimating it may severely delay the deployment of goods and services. To better understand the ways in which individuals perceive flood risk and make decisions related to evacuation, in this section a user study is conducted using survey questionnaires and a simulated flooded town in a VR environment. Findings of this study provide valuable insights into the challenges that people face when making decisions related to flood risk and evacuation, and can inform the development of more effective communication strategies and evacuation planning protocols.

Risks Associated with Floodwater Depth

A series of laboratory-based experimental studies have investigated human stability with respect to water level and flow (Abt et al., 1989; Cox, 2004; Cox, 2010). According to Cox et al. (2010) the stability of individuals in floodways is influenced by multiple factors, with flow depth and velocity being the most crucial. A high flow depth increases buoyancy and decreases friction, leading to a higher likelihood of tumbling failure. On the other hand, low flow depth with high velocity may result in sliding instability. The study by Cox et al. in 2004 indicates that high flow depth and low velocity can be even more hazardous,

as it increases the chances of being swept away and drowned. The study by Cox et al. in 2010 indicates that the low hazard range for untrained and equipped adults (with a height and mass product of more than 50) exists for water depth lower than 1.2 meters (~3 ft and 11 inch) and maximum velocity of 0.3 m/s.

Flood Risk Perception

The risk assessment process involves the measurement of actual risk by experts, taking into account factors such as hazard, community exposure, sensitivities, and capacities (Aerts et al., 2018; Rana & Routray, 2018). On the other hand, perceived risk is determined by various factors, including exposure, previous experiences, community/individual understanding, cognitive thinking, and socio-political influences (Wachinger, 2010). Flood risk perception refers to the way in which individuals, communities, and organizations understand and respond to the risk of flooding (GREEN et al., 1991). Perceptions of flood risk vary among people, influencing their exposure to risk. In light of this, local and national agencies are paying increasing attention to the role of risk perception in order to navigate the development of new policies and technologies (Sjöberg & Wåhlberg, 2002). Studies on risk perception have proposed two approaches: rationalism and constructivism. The rationalist approach views risk perception as a cognitive process through which individuals assess the benefits and costs of a decision by using their mental construct of risk to arrive at a decision. The two theories of heuristics and psychometric paradigm are established under rationalism approach (Birkholz et al., 2014; Slovic, 2000). The heuristics theory sheds light on the decision-making processes used by individuals in uncertain situations, taking into account the potential gains and losses (Bustillos Ardaya

et al., 2017). Conversely, the psychometric paradigm focuses on the individual's cognitive variables and how they influence risk perception (Birkholz et al., 2014). These two theories provide a complementary perspective on how individuals form their opinions and make decisions regarding risk, offering insight into the complexities of risk perception. In contrast, the constructivism approach considers risk perception from a sociological perspective (Wachinger, 2010). The theories established under the constructivism approach include social construction of risk (the influence of socio-political factors on risk perception) and cultural theory (the impact of social structure and cultures on risk perception) (Ren et al., 2017; Short, 1984).Few studies have found a correlation between flood risk perception and socioeconomic factors including past flood experience (Botzen et al., 2009; M. K. Lindell & Hwang, 2008; O'Neill et al., 2016; Rana & Routray, 2018), age and gender (Babcicky & Seebauer, 2017; Siegrist & Gutscher, 2006), education and knowledge (Qasim et al., 2015), income and occupation (Peacock et al., 2005; Sullivan-Wiley & Short Gianotti, 2017). Previous research has primarily examined how various demographic factors influence risk perception. Nevertheless, to the author's best knowledge, immersive flood evacuation environments have been widely investigated to examine flood depth perception by humans. Furthermore, there is a dearth of research on using urban landmarks to estimate flood depth when flood gauges are not present. To address this gap, a user study was conducted in a virtual reality environment by simulating a flooded town to evaluate human perception of flood risk.

Disaster Risk Assessment Using Virtual Reality

With the advancements in VR technology, researchers have utilized it for improving disaster preparedness and response. By creating a simulated environment that accurately replicates the experience of being in a flooded area, VR can provide a safe and controlled space for individuals to develop a better understanding of the challenges and risks associated with different natural hazards. Also, unlike traditional tabletop experiments, by immersing individuals in a realistic flood scenario, VR can help convey the severity of the situation and increase awareness of the potential consequences of flood-related hazards. Several researchers have utilized VR in the field of disaster preparedness and response. For example, Ooi et al. (2019) developed a VR-based educational training system focusing on fire disasters and concluded that participants' fire extinguishing start time was reduced by 10 seconds using this system (Ooi et al., 2019). Nakamoto et al. (2017) proposed a VR-based disaster experience system to improve disaster consciousness for people (Nakamoto et al., 2017). As a disaster material, Ryu et al. (2007) developed a real-disaster video by combining real-time physical simulation and VR (Ryu & Ohno, 2007). Xi et al. (2014) enhanced the realism of VR-based fire evacuation training using gaming technology (Xi & Smith, 2014). Sermet and Demir (2019) developed a multi-player and voice-enabled VR gaming framework (called Flood Action VR) for improving flood risk awareness (Sermet & Demir, 2019). Mol et al. (2022) utilized immersive VR to explore whether exposure to a simulated disaster can motivate individuals to invest in risk reduction measures for flooding, and found that participants who experienced the virtual flood, invested significantly more in a designed flood risk investment game (Mol et al., 2022).

Methodology

VR Environment

First a virtual town was simulated in Unity (a game engine commonly known as Unity3D) (Figure VI-1). The environment was programmed in C Sharp. To facilitate an immersive VR experience, a background noise of relaxing water flow was played in low volume through the Oculus Rift headphones. A map was also provided in the VR environment which helped the participants to locate themselves in the virtual town. The red dot on the map (Figure VI-1) was set as the starting point of the VR experiment. In the virtual town, 5 types of urban landmarks (e.g., cars, buildings, stop signs, fire hydrants, and trees) were simulated and placed in various locations. Furthermore, standing water was simulated to submerge the virtual town. The VR equipment consisted of an Oculus Rift headset with internal headphones and controllers (Figure VI-2). Figure VI-3 presents a screenshot of the first-person view of the VR environment using the VR headset.

Figure VI-1 The simulated town in Unity.

Figure VI-2 Virtual reality headset (Oculus) and controllers.

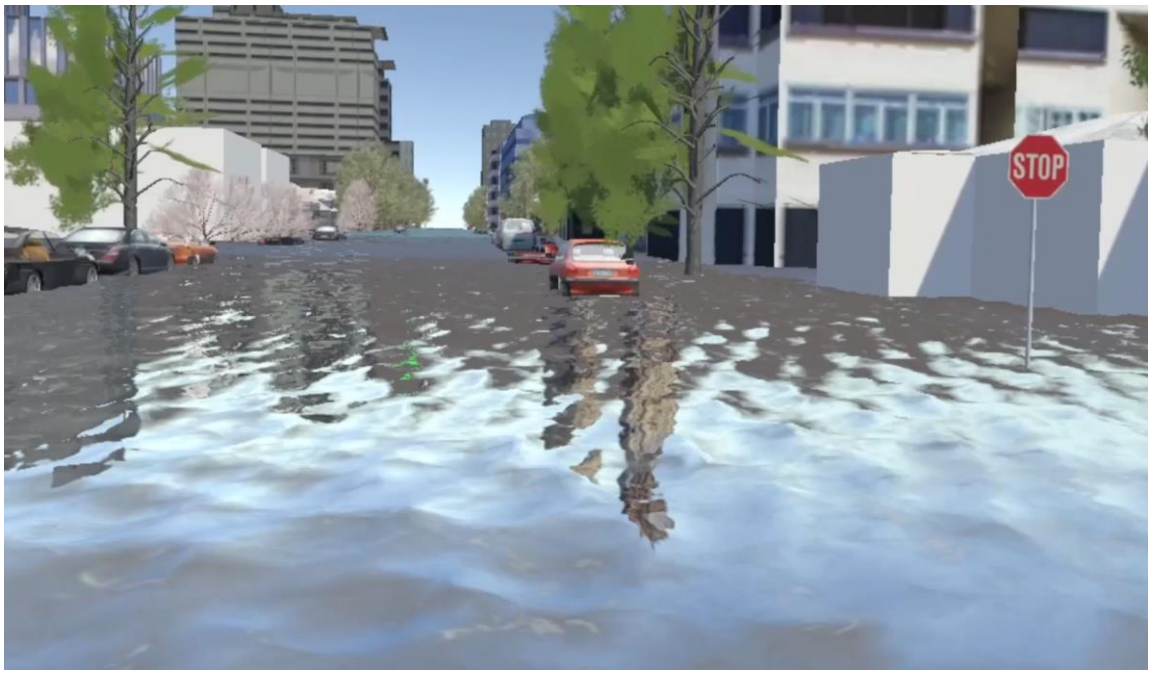

Figure VI-3 First-person view of the VR environment using the VR headset.

Participants

Participants were recruited from Texas A&M University using university-wide emails and advertisements. This selection restricted participation to respondents who have access to

the university email. Moreover, the survey included an informed consent form and excluded respondents under 18 years old. After sending the campus-wide email, 62 people expressed initial interest, and 47 people participated in the study. A reminder was sent to the participants 1 day prior to the experiment. Data collection in the lab started on 3 February 2023 and the last participant was scheduled for 28 February 2023. All participants completed all the three parts of the study (the pre-survey, the VR experiment, and the post-survey).

Procedure

The study protocol was approved by the Texas A&M Institutional Review Board (IRB). All surveys and lab experiments were conducted in the Department of Construction Science (Francis Hall) at Texas A&M University. At the beginning of the study, participants were seated behind a laptop computer to fill in the pre-survey (Appendix B), available in the online supplemental material. The pre-survey included questions on their demographic factors (e.g., age, gender, ethnicity, and zip code), their past flood experience, pas flood evacuation form, sources of information used to get flood depth, whether they have a mobile device, and whether they experience a major interruption in the mobile data during floods. Lastly, they were asked to provide their opinion on required features for computer/mobile apps for personal evacuation navigation or flood rescue operation. Participants completed the pre-survey in approximately 10 minutes.

After completing the pre-survey, the VR experiment was conducted. First, participants received instructions on how to operate the VR equipment for approximately two minutes. In the practice phase, participants found themselves in a virtual flooded town, where they

were instructed to walk and look around in the environment using the VR headset and the controllers. After the practice phase, the VR experiment re-started, and participants found themselves in the starting point. Participants were asked to walk freely in the VR environment and explore the areas. Then, at random locations, participant was asked to stop and report an estimate of water depth at their location. The number and locations of the points were selected randomly by the study personnel for each individual. The study personnel logged each reported water depth with its corresponding location on the map in a data collection sheet. Participants were also said that they can use any urban landmark in the environment (e.g., trees, buildings, stop signs, fire hydrants, vehicles) for estimating water depth at their location. Figure VI-4 shows sample photographs of the VR experiments performed in the user studies. After five minutes of the VR experiment, the study personnel announced the end of the VR experiment and helped the participant to remove the VR headset and controllers. After the VR intervention, participants were seated behind a laptop computer to fill in the post-survey (Appendix B), and were asked to rank the urban landmarks (trees, buildings, stop signs, fire hydrants, vehicles) based on their visibility in the environment and also based on their frequency of use as a benchmark for water depth estimation.

Figure VI-4 Virtual reality experiments in the user studies.

Preliminary Results

Pre-survey Results

The pre-survey results showed that the age of participants ranged from 18 to 62 years old, with 62.5% falling equal or between 20 and 30 years old. Gender distribution was almost equal among participants, with 43.75% female and 54.17% male (2.08% did not disclose their gender). In terms of ethnicity 43.75% of participants identified as White/Caucasian, 6.25% as Black or African American, 43.75%, as Asian/Pacific Islander, and 4.17% as multiple ethnicity/other, and 2.08% did not disclose their ethnicity. Only 25% of participants reported prior first-hand experience with flood events, while the majority (72.92%) had no prior experience, and 2.08% of participants did not remember. Past flood experiences included Hurricane Harvey (2017), Hurricane Ike (2008), a flood in Miami, flash floods in College Station and Amarillo, and Ontario, a 2021 flood in Maharashtra (India), a Typhoon Mangkhut in Hong Kong, a 2021 flood in Namur (Belgium), a flood in Mumbai (India), floods in Baton Rouge, Mandeville (Louisiana) between 1970 and 2001, and a flood in Guadalajara (Mexico). Of those who evacuated, 5 participants did so on foot, 4 used some type of boat, 2 used trucks, and 2 used cars. Participants used various methods to obtain information about flood depth, including watching news (N = 16), flood gauges (N = 7), local measurements (N = 7), social media (N = 9), and FEMA flood maps (N = 5), highlighting that watching news and social media were among the most used sources for accessing flood information. Also, 7 participants did not obtain any information about flood depth, while 1 participant relied on their pre-existing knowledge of flooded areas. All participants had mobile devices. Among those with past flood

experience, 50% reported experiencing major interruption in mobile data connectivity during their most recent first-hand flood experience, while 50% did not experience any interruption.

Post-survey Results

Based on the results of the post-survey, on a 5-point Likert scale, cars received the highest score of 4.43 in terms of being recognized in the environment by participants. Next on the list were stop signs with a score of 3.36, buildings with a score of 2.96, trees with a score of 2.25 and fire hydrants with a score of 1.70. The same survey also revealed that participants most frequently used cars as a benchmark to estimate flood depth (score of 4.57) likely due to their prominence and familiarity with their shapes and sizes. Stop signs were the second most utilized object (score of 3.19), likely because they were also highly noticeable in participants' routes. In contrast, fire hydrants were the least frequently used objects (score of 2.00) mostly due to their limited visibility in high flooded areas. Table VI-1 presents the recognizability and the frequency of use of the urban landmarks by the participants.

Table VI-1 Results of the post-survey on a 5-point Likert scale.

Object	Car	Stop Sign	Fire Hydrant	Building	Tree
Most recognized	4.43	3.36	1.70	2.96	2.25
Most used	4.57	3.19	2.00	2.60	2.64

Distribution of Data in Different Groups

According to the data, participants under 25 years old achieved the mean absolute water depth estimation error of 0.359 m. (14.161 in.) while participants above 25 years old achieved 0.362 m. (14.269 in.). With respect to gender, the average absolute error for flood depth estimation achieved as 0.352 m. (13.877 in.) and 0.374 m. (14.743 in.) for male and female, respectively. Also, the analysis of collected data indicates that the average water depth estimation error for White or Caucasian was 0.340 m. (13.383 in.), for Black or African American was 0.450 m. (17.718 in.), for Asian or Pacific Islander was 0.371 m. (14.610 in.), and for Multiethnicity or Other was 0.380 m. (14.979 in.). Average absolute water depth estimation based on the most used object achieved 0.372 m. (14.651 in.) for cars, 0.249 (11.220 in.) for stop signs, 0.330 (12.992 in.) for buildings, and 0.404 (15.906) for fire hydrants. With respect to past flood experience, the average absolute error for flood depth estimation was achieved as 0.315 m. (12.386 in.) and 0.379 m. (14.930 in.) for with and without past flood experience, respectively. The average absolute flood depth estimation error for those participated in the VR experiment with low average water level (less than 1 meter) was 0.413 m. (16.260 in.), and for those with medium average water level (between 1 and 1.15 meters) 0.343 m. (13.504 in.), and for those with high average water level (more than 1.15 meters) 0.352 m. (13.858 in.). The flood depth estimation error was calculated as the difference between ground-truth flood depth and estimated flood depth, which was logged in range of -1.725 m. and +1.350 m. with average of 0.119 m and MAE of 0.361 m. Positive flood depth estimation error value indicates underestimation while negative value refers to overestimation.

Difference Between Flood Depth Estimation Error Between Various Groups

Further statistical analysis was conducted (using SPSS software) on parameters including age, gender, ethnicity, past flood experience, the most used object (to estimate flood depth), average flood level, and flood depth estimation error. The normality test was conducted on flood depth estimation error using skewness and kurtosis test as well as graphical test using histogram normal curve indicate that data is normal as skewness is within -1 and +1 (Hair, 2010) and kurtosis within -2 and +2 (Garson, 2012), and majority of the data was dispersed under normal/bell curve in histogram (Field, 2013). Pearson correlations were performed to determine the relationship between flood depth estimation error and other variables, which indicates that mathematically there is a high correlation between flood depth estimation error the two variables of ethnicity and most used object ($P<0.01$). Also, there is a correlation between flood depth estimation error and gender ($P<0.05$).

Table VI-2 Pearson correlations.

		Age	Gender	Ethnicity	Past flood exp.	Most used object	Average flood level
Flood depth est. error	Pearson Correlation	0.005	0.040	0.051	-1.04*	-0.024	0.066
	Sig. (2-tailed)	.927	.419	.316	.036	.626	.0.186
	N	406	406	389	406	406	406

* Correlation is significant at the 0.05 level (2-tailed).

The *t*-test was implemented to determine whether there was any difference in absolute flood depth estimation error between groups of age, gender, and past flood experience. The ANOVA test was performed to determine whether there was any difference in absolute flood depth estimation between groups of ethnicity, most used objects, and average flood level. At 95% confidence level ($\alpha = 0.05$), no significant difference was found in flood depth estimation error for age under 25 ($mean = 14.161\ in., SD = 11.552$) and age above 25 ($mean = 14.268\ in., SD = 12.056\ in.$) no significant difference was observed ($p = 0.849$). At 95% confidence level ($\alpha = 0.05$), no significant difference was found in flood depth estimation error for male ($mean = 13.878\ in., SD = 11.223$) and female ($mean = 14.744, SD = 12.683\ in.$) no significant difference was observed ($p = 0.188$). Meanwhile, at 95% confidence level ($\alpha = 0.05$), no significant difference can be observed in flood depth estimation error between ethnicity groups, e.g., White or Caucasian ($mean = 13.382\ in., SD = 11.567\ in.$), Black or African American ($mean = 17.720\ in., SD = 3.825\ in.$), Asian or Pacific Islander ($mean = 14.610\ in., SD = 0.827\ in.$), and Multiethnicity or Other ($mean = 14.980\ in., 2.606\ in.$) ($p = 0.429$). Among different most used objects of cars ($mean = 14.650\ in., SD = 12.041\ in.$), stop signs ($mean = 9.787\ in., SD = 9.357\ in.$), buildings ($mean = 12.976\ in., SD = 6.290\ in.$), and fire hydrants ($mean = 15.898\ in., SD = 14.825\ in.$), no significant difference was obtained in terms of flood depth estimation error ($p = 0.116$). Although participants who mostly used stop signs as a measurement benchmark had made lower flood depth estimation errors, the statistical analysis did not indicate any significant difference among these groups. Further analysis

is conducted by separating groups of participants into three groups: over-estimators, under-estimators, and none (neither under-estimator nor over-estimator). To do so, participants who mostly over-estimated flood depth (negative error) were grouped as over-estimators, and participants who mostly under-estimated flood depth were grouped as under-estimators (positive error), and each group were analyzed separately. Results indicate that there is no significant difference in flood depth estimation error with respect to most used object for none of the three groups.

Additionally, participants with no flood experience ($mean = 14.929\ in., SD = 12.466\ in.$) reported higher flood depth estimation error compared to those with past flood experience ($mean = 12.386\ in., SD = 9.741$), and there is a significant difference between these two groups ($p = 0.014$). Also, no significant difference was obtained in terms of flood depth estimation error with respect to average ground-truth flood depth (one value per participant) of less than 1 m. (39.37 in.) ($mean = 4.677\ in., SD = 18.622\ in.$) and equal or above 1 m. (39.37 in.) ($mean = 17.362\ in., SD = 1.142\ in.$) ($P = 0.307$). Table VI-3 presents the results of the tests in determining significant difference between flood depth estimation errors with respect to other variables.

Table VI-3 Results of identifying significant difference between flood depth estimation errors with respect to variables.

	Variable	Groups	*N*	Asymp. Sig.
T-test	Age	Under 25	181	0.849
		Above 25	225	
T-test	Gender	Male	226	0.188
		Female	172	
ANOVA test	Ethnicity	White or Caucasian	168	0.429
		Black or African American	18	
		Asian or Pacific Islander	186	
		Multiple ethnicities or Other	17	
T-test	Past flood experience	No	300	0.014*
		Yes	97	
ANOVA test	Most used object	Car	328	0.116
		Traffic sign	34	
		Building	22	
		Fire Hydrant	22	

* Indicates $p < 0.05$

Table VI-3 Continued.

	Variable	Groups	*N*	Asymp. Sig.
ANOVA test	Average flood level	Less than 1 m. (39.37 inch.)	178	0.307
		More than 1 m. (39.37 inch.)	228	

Summary and Conclusions

Previous research has focused on how demographics affect risk perception, but there is little research on how immersive flood evacuation environments and urban landmarks can affect human perception of flood risk. In this section immersive VR was utilized to simulate a flooded environment to assess human's perception of flood risk. Simulating a flooded region in a VR environment mimic risks and consequences in a controlled lab experiment which can improve individuals flood risk perception as discussed by (Mol et al., 2022). At the beginning of the study, participants were asked to fill out a pre-survey, asking participants' demographic information and past flood experience. Then a 5-minutes VR experiment was conducted in which participants were asked to walk in a virtual flooded town and estimate water depth at random locations. Participants were guided to use any of the benchmarking objects in their surroundings (e.g., cars, stop signs, buildings, fire hydrants, and trees). Upon the completion of the VR experiment, participants were asked to fill out a post-survey in which they had to rank the benchmarking objects in terms of their visibility and their frequency of use for water depth estimation.

The objective of the VR experiment was twofold: first, to identify the primary benchmarking object used by participants to estimate flood depth, and secondly, to examine the impact of various factors on flood risk perception during the evacuation process in the absence of additional decision support tools. The results indicated that the majority of participants used cars as their primary benchmarking object due to their familiarity with their sizes and shapes. However, using cars as a benchmarking object may not be the best option since they may not be readily visible in all places, can easily float away in floods, and their sizes can vary. The statistical analysis found no significant difference in the estimation errors made when using different objects to estimate flood depth. These findings suggest that visually estimating flood depth using a benchmarking object alone may not be sufficient, thus justifying the need for a reliable and accurate decision support tool to estimate flood depth on urban roads.

Moreover, the study also found a significant difference in flood depth estimation errors between participants with past flood experience and those without such experience. Specifically, individuals with past flood experience made fewer errors in flood depth estimation than those without such experience. Consequently, it can be inferred that exposing participants to virtual flood events has the potential to enhance their flood risk perception in the real world. In conclusion, this VR experiment highlights the importance of having access to decision support tools for flood depth estimation and the potential benefits of exposure to flood events to improve flood risk perception. The statistical analysis revealed a significant difference in flood depth estimation errors with respect to past flood experience, and indicate that participants with past flood experience had lower

flood depth estimation error. Thus, it can be inferred that exposing participants to virtual flood events has the potential to enhance their flood risk perception in the real world. Due to time constraint only limited preliminary analysis is done, and more data should be collected to improve the generalizability of the results. In general, with more data collected, findings of the study can be used to assess human's perception of flood risk with the goal of informing the development of flood risk communication strategies to improve stakeholder perceptions of flood risks. In addition, conducting this experiment with a larger number of community participants (outside the university setting) will allow a more rigorous analysis with respect to certain confounding factors such as proximity to disasters, level of education, and socioeconomic status. In the current study, all participants were either students or faculties in a university setting, which may not be representative of the broader population. Therefore, by involving a larger and more diverse sample of participants in future direction of this study, it could better assess the impact of these factors on flood perception and provide more reliable insights into how different groups may perceive and respond to flood risks.

CHAPTER VII

CONCLUSION

Summary

The number and intensity of flood events is expected to increase globally due to asymmetric urbanization, growing coastal population, and climate change. During urban floods, emergency managers, search and rescue teams, and evacuees make decisions based on available data, which may not necessarily represent how floodwaters move in the surrounding areas, especially in and around residential neighborhoods. With the goal of improving the quality of decisions made during flood events to evacuate people or move goods and services while avoiding flooded areas, this study first conducted a community needs assessment that highlighted the need for (near) real-time data on floodwater conditions, risk-informed evacuation plans, and safe and shortest transit routes.

Based on the results of the community survey and according to many studies, knowing the depth of floodwater during flood events, is of critical importance to first responders, emergency managers, and ordinary people involved in search and rescue operations and community evacuation. This information, however, is not readily available or shared in many jurisdictions particularly in the immediate flood aftermath when it is most needed. Additionally, current flood mapping methods such as those relying on DEMs fail to capture reshaped surface topography and microtopographic variations in flat terrain especially in urban areas, leading to large vertical errors. New digital media capture and data exchange platforms coupled with advancements in ML, image processing, and

computer vision for object detection have created new opportunities for remotely estimating water level depth in flooded areas. However, Effective information and communication technology solutions consider communities' most critical needs while providing a simple and easy-to-use interface for collecting valuable information required for analysis. The goal of the community survey in this study was to inform the design of technology and ensure that the final outcome serves the needs of people who are affected by floods.

Next, a novel flood depth estimation method was developed using visual analysis of crowdsourced photos of submerged stop signs and comparing them with photos of the same signs before the flood (using GSV) to estimate flood depth in real-time. Since traffic signs have standard sizes, the difference between pole lengths in paired pre- and post-flood photos of the same sign can be computed and used as the basis for estimating the depth of floodwater at the location of the sign. Also, the advantage of using stop signs as measurement benchmarks is that their shapes and sizes are standardized, and a large number of these signs are installed and easily recognizable in urban areas (compared to the relatively fewer number of conventional flood gauges). Next, two computer vision models (Computer Vision Model I and Computer Vision Model II) were developed and validated for estimating floodwater depth in street photos using stop signs as measurement benchmark. In the first part of the methodology development, Computer Vision Model I was developed which consists of Mask R-CNN for detecting the octagon shape of stop signs, and the Canny edge detection and probabilistic Hough transform for detecting vertical edges and discovering potential pole candidates. An in-house dataset, named

BluPix v.2020.1 consisting of paired web-mined photos of submerged stop signs across 10 FEMA regions (for U.S. locations) and Canada was generated and used to test the performance of Computer Vision Model I. To limit the error in pole length detection, a tilt correction method was designed and applied to all photos to ensure poles are in near vertical position prior to the application of Hough line transform. Overall, pole length was estimated with and RMSE of 17.43 and 8.61 inches in pre- and post-flood photos, respectively, leading to an MAE of 12.63 inches in floodwater depth estimation. Then, a route optimization algorithm was implemented based on the generated inundation map to determine the shortest flood-free evacuation route.

Next, in the second part of the study, the Computer Vision Model II was developed by training a YOLOv4 model on an in-house dataset of annotated stop signs and poles. An in-house training set comprising web-mined photos and photos extracted from the Microsoft COCO dataset, were used for training the YOLOv4 model (Blupix v.2021.2). The trained model was then validated using 5-fold cross validation, and subsequently tested for flood depth estimation on 147 paired photos from our in-house test set (Blupix v.2022.1). Results indicate MAE of 1.723 and 2.846 in. for pole length estimation in pre- and post-flood photos, respectively, and an MAE of 4.710 in. in flood depth estimation which shows a significant improvement compared to the previous model.

To evaluate the efficacy of the flood depth estimation using photos of stop signs, 20 paired pre- and post-flood photos of stop signs from Hurricane Harvey (2017), in Houston, Texas were selected. In the first part, the A* search route optimization was implemented on the generated flood depth map using interpolated stop sign data. In the next part, the flood

depth map was generated using Computer Vision Model II and augmented by USGS gauges flood depth data during Hurricane Harvey and the route optimization was implemented using Dijkstra's algorithm. Both results indicated the effectiveness of the proposed methods in determining shorter transit routes during flood events compared to the routes generated based on gauge data only. However, the second approach proposed a more accurate and reliable method for flood depth mapping and route planning.

To enable crowdsourced data collection, a web application, called Blupix, was designed and launched. A key challenge in using crowdsourced data for flood mapping is that technology users might upload incorrect photos (Garcia-Molina et al., 2016). In this study, to remedy potential cases where user-contributed photos are not of expected quality, all image uploads were initially inspected by trained project personnel (a.k.a., app admin), prior to being approved or rejected. Only approved photos were shown on the map. To facilitate data collection at large scale, and provide ad-hoc information for people to gain situational awareness during flood events, a mobile application with a built-in TensorFlow Lite EfficientDet model (trained on the in-house dataset of annotated stop signs and poles) was developed for estimating flood water depth using geolocated photos of submerged stop signs. The main goal of developing this app was to provide a simple, reliable, and affordable mobile platform for the general public to access real-time flood depth data in their surrounding area. The use of this app is scalable to most geographical locations (even in data deserts) with GSV data. To ensure the functionality of the developed app in offline mode, an additional crowdsourcing platform was developed to collect pre-flood photos of stop signs. This platform enables users to upload photos of stop signs in their local

environment, which are then mapped on the Blupix app map as crowdsourced pre-flood photos. When a flood occurs, users can upload photos of flooded stop signs to the app, which can be paired with the crowdsourced pre-flood photos to instantly estimate the flood depth, even in offline mode. Lastly, immersive VR was utilized to reconstruct urban flood scenes and conduct a series of user studies to assess the human perception of flood risk on urban roads during an evacuation process. The user study included a pre-survey (asking about demographic questions), a 5-minutes VR experiment, and a post-survey (asking about the recognizability of the urban landmarks (e.g., cars, stop signs, buildings, fire hydrants, and trees) and their frequency of use as a reference point for flood depth estimation). The study found that cars were the most commonly used benchmarking object, but may not be the best option due to limitations such as visibility and size variability. Also, statistical analysis of results revealed that relying solely on visual estimation is insufficient, and there is a need for accurate decision support tools to estimate flood depth on urban roads. Preliminary results of the user study indicated that there was a significant difference for flood depth estimation error with respect to past flood experience, indicating that participants with past flood experience had lower absolute flood depth estimation error on average. Therefore, exposing participants to flood evacuation experience using immersive VR has the potential to improve flood risk perception. In order to more accurately assess the impact of various factors on flood perception and gain more reliable insights into how different groups may perceive and respond to flood risks, future directions of this study should involve a larger and more diverse sample of participants.

In summary, the proposed decision support system in this research, proposed a simple, reliable, and affordable tool for both first responders and regular citizens to access real-time and accurate flood depth information in their surroundings and find the shortest flood-free route during flood events to the target destination. The crowdsource based data collection in the developed approach enables large scale and timely data collection when a disaster strikes, and the collected flood depth data can be utilized to generate high spatial resolution flood maps. The proposed system works in undeveloped areas, data deserts, and low-income communities when FEMA flood maps or flood sensors are not available. A major benefit of the developed app is that it is not limited to any geographical location and does not require large scale installation and maintenance of physical sensors.

Collectively, these processes can provide an end-to-end platform for obtaining floodwater depth information and conducting intelligent wayfinding. Ultimately, users will be able to instantly estimate flood depth in and around their locations using the Blupix Mobile app, and inform others by uploading flood photos from their neighborhoods to the Blupix app.

Research Contributions

Technical Contributions

This study has made significant contributions in several key areas. First, a user study was conducted to assess the community's needs during flood events (Chapter III). The study then developed a method to use traffic signs as standard flood depth sensing stations for accurate street-level flood depth estimation by comparing sign's pole length in a photo of a traffic sign before (from GSV) and after a flood (crowdsourced photo) (Chapter IV). Additionally, two computer vision models (Computer Vision Model I and Computer

Vision Model II) were developed using traditional image processing techniques and CNNs to estimate flood depths using photos of traffic signs (Chapter IV). To enable human-centered and large-scale data collection, a crowdsourcing platform (called Blupix) was designed and developed to collect photos of flooded traffic signs (Chapter IV). Furthermore, an additional crowdsourcing platform was designed and developed (called Blupix Preflood) to collect pre-flood photos of traffic signs, which enables offline access to the flood depth data in any geographical location even when GSV data is not available (Chapter IV). Then, a high spatial resolution flood depth map was generated by combining USGS flood gauge data with crowdsourced data (Chapter V). The study also developed two risk-informed decision support systems for intelligent wayfinding in flood events using two route optimization algorithms (Chapter V). Additionally, the study developed a mobile app with a built-in computer vision model for estimating real-time flood depth estimation and providing ad-hoc situational awareness of floods for communities (Chapter V). Lastly, the study conducted a user study to understand human's perception of risk in a controlled environment by simulating a flooded town in a VR setting (Chapter VI). As a result of this research, so far four journal papers and three conference papers have been published and two additional journal papers and two conference paper are in preparation. Also, three crowdsourcing apps were developed, e.g., Blupix, Blupix Mobile, and Blupix Preflood. Moreover, three publicly available datasets (namely, Blupix datasets) of annotated photos of stop signs before and after floods are created (https://github.com/ciber-lab/blupix)

Societal Contributions

Numbers show that 75% of FEMA flood maps are older than 5 years, and 11% date back to the 1970s and 80s (Eby, 2019). This poses a significant challenge to communities that reside in and around floodplains and flood-prone areas. To address this issue, this study developed an affordable and reliable tool that can be utilized by community members to access real-time flood depth information at their location and also inform other communities and first responders by sharing this information on the Blupix platform. Continuous community engagement throughout the study helped identify community's real needs which in turn informed the technology development process. Members of the community were involved in several aspects of the study, which spanned over three years. Input was actively sought from the community during the development, testing, and launch phases of the Blupix app. For example, findings from the community needs assessment survey (Chapter III) were used in the development of the Blupix app to provide essential user functionalities. During the testing phase, community meetings provided feedback that led to specific improvements such as enabling Blupix to work in offline mode by adding the option for users to upload pre-flood photos of stop signs prior to a flood event (thus, eliminating the need to connect to the internet during a flood event to access GSV). Community engagement efforts continued in the post-development phase to collect feedback on the functionality and usability of the app during its launch phase, and identify areas for improvement. For example, during a community meeting with a disaster non-profit organization, participants requested the addition of voice recognition to the Blupix app. This feature would enable them to use the app while wearing gloves or with

wet hands, and is one of the future directions of this research. Additionally, studies show that people are becoming more complacent regarding natural hazards, leading them stay or to move into high-risk areas (Colten & Sumpter, 2009; Tellman et al., 2021). This study recognized this challenge and engaged with communities to increase public awareness of future flood risks, by helping them access reliable tools to get information about flood risk at their locations during a flood event. As an example, a community partner in Port Arthur volunteered its constituents to help identify and prioritize their specific needs, as well as collect and share photos of stop signs in flood-prone spots in their neighborhoods. This collaboration ensured that the developed tool was tailored to the 'community's expectations, leading to an improved overall flood risk assessment and management process. Overall, the design of the technology was justified by an actual societal need, and moving forward, the implementation and improvements to this technology will continue to benefit from continuous engagement with the members of the general public, disaster-related practitioners, and policymakers. Figure VII-1, Figure VII-2, and Figure VII-3 are examples of various community engagements (including crowdsourced data collection, involvement in the design and testing phases of the technology, and raising public awareness of floods). Overall, the true value of this study goes beyond the mere design of a tool, rather, it will facilitate and encourage the inclusion of different population groups (e.g., homeowners, policymakers, disaster professionals, researchers) in a conversation that aims to improve the status quo of disaster resilience in U.S. communities. This will also open the gate for people to work hand in hand with professionals to make impactful disaster policy changes.

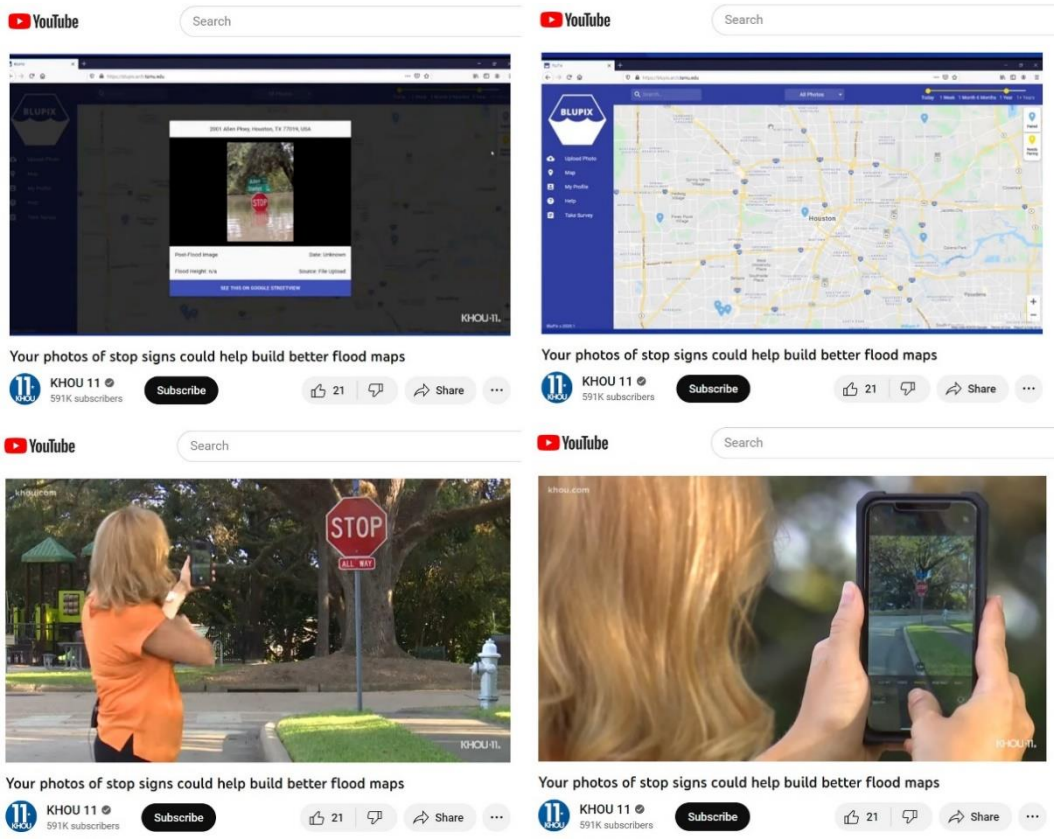

Figure VII-1 Screenshots of KHOU (CBS Houston) news segment covering the Blupix app (August 2020) (KHOU 11, 2020).

Figure VII-2 Community meetings with students from Port Arthur, Texas, who carried out tabletop experiments using the Blupix app to estimate floodwater depth (March 2022).

Figure VII-3 Community data collection in Port Arthur, Texas (November 2022).

Practical Limitations and Future Work

Standardized Urban Landmarks as Flood Depth Sensing Stations.

To enhance the applicability and generalizability of the AI-based flood depth estimation model, the computer vision model should be trained on all standardized traffic signs, including but not limited to yield signs, one-way signs, and parking signs. By training the model to detect traffic signs, and knowing their sizes in inches, it can locate them on GSV images and estimate the water depth around them. Additionally, the model can be trained to detect and analyze other standardized urban landmarks for flood depth estimation, such as fire hydrants, traffic lights, bridges, lights, etc. These landmarks can be used as reference points to estimate flood depth accurately in a given area. The comprehensive model will be capable of estimating flood water depth in any area close to these standardized urban landmarks with known sizes.

Data Augmentation Using Various Resources.

To enhance the density of interpolation observations, various forms of data can be converted to a single format and overlayed. In fact, incorporating different types of data, such as satellite imagery, weather data, and historical flood data, and crowdsourced data can enhance the accuracy and generalizability of flood depth maps. In this study, augmentation of crowdsourced photos with flood gage data was explored. Flood gauges mostly provide information on the rural flood-prone areas. However, in future direction of work, researchers should explore incorporating different sources of data, such as satellite imagery, DEMs, LiDAR data, with crowdsourced photos to generate a high spatial resolution flood depth map (McDougall & Temple-Watts, 2012). Satellite imagery

can provide an overview of the flood-affected area (Cian et al., 2018), while DEMs can be used to estimate the topography of the region (Hawker et al., 2018). However, these sources may not provide precise information about flood depth in specific locations. On the other hand, crowdsourced images and data can be analyzed to generate flood depth in areas where none of the previously mentioned measurements are available. By incorporating data analyzed by computer vision from crowdsourced photos with data from other resources, the model can provide a high spatial resolution flood depth map in urban and rural areas, predict flooding patterns and potential flood zones, making it an essential tool for emergency response and planning. Moreover, other than visual analysis of the crowdsourcing photos, relevant data can be extracted from social media contents. It is noteworthy to say that data integration from multiple sources pose certain challenges in terms of data formats, data quality, and data management systems which makes it difficult to combine and analyze the data effectively (Li et al., 2018; Meesuk et al., 2017). To address these challenges, a standardized data format and data management system should be developed to be utilized across different sources of data.

Water Level Change and Flowing Water

The developed model in this study provides static flood depth information at one location at the time of capturing image. In case of flowing water or rapid water change due to drainage system or permeable surfaces, the flood estimated flood depth may change. In fact, the developed model is mostly applicable in the aftermath of a flood event in urban areas with standing water over impermeable surfaces, which helps users to utilize access the real-time flood depth information during the evacuation process. As a part of future

work, terrain data and hydrological modeling can be incorporated with the developed model to predict floodwater depth in areas with varying surface permeability, such as rural or natural areas, as well as predicting the floodwater level in downstream areas (Campana & Tucci, 2001). To predict the downstream condition from the upstream flood depth, terrain data (such as DEMs) can be used to provide information on the elevation and slope of the land, as well as the location of waterways and other natural features. These models take into account the terrain and the topography of the area, as well as other factors such as the presence of structures or other obstructions that may affect the flow of water. Moreover, hydrological models can simulate the flow of water through a given area (Kenward, 2000). By inputting flood depth information obtained upstream into these models, flood conditions downstream can be predicted. Combining the real-time flood depth estimation models with DEM and hydrological models can be particularly useful for emergency response and flood planning, as it allows for the prediction of flood conditions in areas that may be downstream from a flood event.

Human-Technology Interaction

This study has developed crowdsourcing web applications (Blupix and Blupix Preflood) hosted on a cyberinfrastructure for collecting crowdsourced photos of traffic signs and generate a flood depth map as well as a mobile app (Blupix Mobile) to provide real-time flood depth information. The success of these software depends on their user interface and functionality, which in turn, relies on the principles of Human-Computer Interaction (HCI). In the future, it is important to explore the user interface and functionality of these apps from the perspective of HCI, which includes evaluating the usability of the apps,

their user-friendliness, and the overall experience of users interacting with them (Marincioni, 2007; Thüring & Mahlke, 2007). HCI for the three developed apps in this study can be investigated by conducting usability tests and user surveys, which will provide valuable feedback on the current design of the apps and suggestions for improvements, which will help in identifying new features that can enhance the overall functionality and usefulness of the apps. For example, incorporating augmented reality features that can overlay flood depth information on top of the camera view can be a useful addition to the mobile app. Additionally, integrating voice commands to input and receive information on the app can improve accessibility and ease of use for users.

Citizen Science

Citizen science has been recognized as a cost-effective approach to collect large-scale data; however, it also presents certain limitations. For instance, the accuracy and reliability of the data collected through citizen science can be affected by various factors, such as user bias, user error, and differences in data collection techniques. To address this challenge, the developed tool in this study incorporates a review process by Blupix app administrators to ensure data quality. Nevertheless, to operate the tool in real-time during flood events, an automatic review process using AI algorithms should be implemented to expedite the data cleaning process. This can improve the speed and efficiency of the tool and ultimately enhance the reliability of the collected data. Another challenge is the reliability of the model on crowdsourced data from citizens. To increase the spatial resolution of the flood depth map, the model relies on the availability of a larger and more diverse dataset. As the number of crowdsourced images increases, the accuracy and

precision of the generated flood depth map can be enhanced, providing a more detailed representation of the flood event. To overcome this challenge, crowdsourced data collection can be conducted using different tools. For example, installing cameras on emergency vehicles or flood sensors at strategic locations can provide more crowdsourced images of urban roads. By integrating data from multiple sources, the spatial resolution of the flood depth map can be increased, and the accuracy of the flood depth estimates can be improved.

The Effect of Drainage Systems on Flood Depth Mapping

The limited intake capacity of a drainage system may result in the partial flow of the water through the pipes, leading to a large volume of runoff flowing on the surface during and after heavy rainfall (Palla et al., 2018). In instances where the pipe system's capacity is insufficient, the water in the pipes may return to the street system, leading to surface flooding caused by the flow of water from the pipe system to the street system. The drainage system is an important factor in flood depth mapping as it can significantly affect the accuracy of the flood depth information (Mark et al., 2004). The developed app provides real-time flood depth information that can be useful in monitoring the impact of drainage systems on flood depth. By comparing photos of the same traffic signs taken at different times, the functionality of the drainage system can be assessed. However, relying solely on crowdsourced data and citizen science can limit the accuracy and reliability of the flood depth mapping results. Therefore, it is important to incorporate additional urban elements into the flood depth mapping process, such as the physical characteristics of buildings, roads, and infrastructure. This approach can provide a more comprehensive and

accurate representation of the flood depth in urban areas, which can aid in the development of effective flood management strategies.

Human Perception of Risk

Chapter VI contained preliminary results of a use study on human's perception of flood risk using VR. While a user study using VR can provide valuable insights into human perception of flood risks, it also has several limitations. For example, VR may not accurately replicate the real-world experience of a flood event, and participants may not react to virtual scenarios in the same way they would to a real flood event. Assessing the realisticness of a simulated environment in a user study using VR is needed to ensure that the study provides accurate and reliable results (Yadav et al., 2019). There are several ways to assess the realisticness of the simulated environment. One common approach is to assess participants' subjective perception of the simulated environment. This can be done by asking participants to rate the simulated environment's realisticness or by using physiological measures such as heart rate and skin conductance to assess participants' emotional responses to the simulated environment (Yadav et al., 2019). Furthermore, the study may not reflect the diversity of experiences and perceptions across different populations and geographic regions. Despite these limitations, the study highlights the importance of understanding human risk perception during flood events and opens doors for further research on this domain for future researchers.

REFERENCES

Abt, S. R., Wittier, R. J., Taylor, A., & Love, D. J. (1989). HUMAN STABILITY IN A HIGH FLOOD HAZARD ZONE. *Journal of the American Water Resources Association*, *25*(4), 881–890. https://doi.org/10.1111/j.1752-1688.1989.tb05404.x

AECOM. (2013). *The impact of climate change and population growth on the National Flood Insurance Program through 2100*.

Aerts, J. C. J. H., Botzen, W. J., Clarke, K. C., Cutter, S. L., Hall, J. W., Merz, B., Michel-Kerjan, E., Mysiak, J., Surminski, S., & Kunreuther, H. (2018). Integrating human behaviour dynamics into flood disaster risk assessment. *Nature Climate Change*, *8*(3), 193–199. https://doi.org/10.1038/s41558-018-0085-1

Aggarwal, S. (2018). Modern web-development using ReactJS. *International Journal of Recent Research Aspects*, *5*(1), 133–137.

Alfieri, L., Bisselink, B., Dottori, F., Naumann, G., de Roo, A., Salamon, P., Wyser, K., & Feyen, L. (2017). Global projections of river flood risk in a warmer world. *Earth's Future*, *5*(2), 171–182. https://doi.org/10.1002/2016EF000485

Alizadeh, B., & Behzadan, A. (2022, July 24). *Crowdsourced-based deep convolutional networks for urban flood depth mapping*. https://doi.org/10.35490/EC3.2022.145

Alizadeh, B., Li, D., Zhang, Z., & Behzadan, A. H. (2021). Feasibility study of urban flood mapping using traffic signs for route optimization. *Proceeding of EG-ICE 2021 Workshop on Intelligent Computing in Engineering*.

Alizadeh Kharazi, B., & Behzadan, A. H. (2021a). Flood depth mapping in street photos with image processing and deep neural networks. *Computers, Environment and Urban Systems*, *88*, 101628. https://doi.org/10.1016/j.compenvurbsys.2021.101628

Alizadeh Kharazi, B., & Behzadan, A. H. (2021b). Flood depth mapping in street photos with image processing and deep neural networks. *Computers, Environment and Urban Systems*, *88*, 101628. https://doi.org/10.1016/j.compenvurbsys.2021.101628

Alsnih, R., & Stopher, P. R. (2004). Review of Procedures Associated with Devising Emergency Evacuation Plans. *Transportation Research Record: Journal of the Transportation Research Board*, *1865*(1), 89–97. https://doi.org/10.3141/1865-13

Altay, N. (20085). *Issues in disaster relief logistics: Large-scale disasters: Prediction, control, and mitigation*.

American Climate. (2019). *An inside climate news project, Deaths & major events*.

Annelli, J. F. (2006). The National Incident Management System: a multi-agency approach to emergency response in the United States of America. *Revue Scientifique et Technique*, *25*(1), 223–231.

ArcGIS Developer. (2021). *ArcGIS API for Python*.

Arnell, N. W., & Lloyd-Hughes, B. (2014). The global-scale impacts of climate change on water resources and flooding under new climate and socio-economic scenarios. *Climatic Change*, *122*(1–2), 127–140. https://doi.org/10.1007/s10584-013-0948-4

Ayachi, R., Afif, M., Said, Y., & ben Abdelali, A. (2021). Drivers Fatigue Detection Using EfficientDet In Advanced Driver Assistance Systems. *2021 18th*

International Multi-Conference on Systems, Signals & Devices (SSD), 738–742. https://doi.org/10.1109/SSD52085.2021.9429294

Babcicky, P., & Seebauer, S. (2017). The two faces of social capital in private flood mitigation: opposing effects on risk perception, self-efficacy and coping capacity. *Journal of Risk Research*, *20*(8), 1017–1037. https://doi.org/10.1080/13669877.2016.1147489

Barz, B., Schröter, K., Münch, M., Yang, B., Unger, A., Dransch, D., & Denzler, J. (2018). Enhancing Flood Impact Analysis using Interactive Retrieval of Social Media Images. *KIT Scientific Publishing*, *5*(1), A06, 21 S.

Baugh, C. A., Bates, P. D., Schumann, G., & Trigg, M. A. (2013). SRTM vegetation removal and hydrodynamic modeling accuracy. *Water Resources Research*, *49*(9), 5276–5289. https://doi.org/10.1002/wrcr.20412

Becker, J., Johnston, D., Coomer, M., & Ronan, K. (2008). Flood risk perceptions, education and warning in four communities in the Hawkesbury-Nepean Valley, New South Wales, Australia : results of a questionnaire survey, February 2006. *GNS Science Report.*, *2008*(2), 1–58.

Beggs, J. C. (2018). Applications. In *Disaster Epidemiology* (pp. 163–169). Elsevier. https://doi.org/10.1016/B978-0-12-809318-4.00022-8

Bennett, P., Calman, K., Curtis, sarah, & Fischbacher-Smith, D. (2010). *Risk Communication and Public Health* (P. Bennett, K. Calman, S. Curtis, & D. Fischbacher-Smith, Eds.). Oxford University PressOxford. https://doi.org/10.1093/acprof:oso/9780199562848.001.0001

Berens, A. S., Palmer, T., Dutton, N. D., Lavery, A., & Moore, M. (2021). Using search-constrained inverse distance weight modeling for near real-time riverine flood modeling: Harris County, Texas, USA before, during, and after Hurricane Harvey. *Natural Hazards*, *105*(1), 277–292. https://doi.org/10.1007/s11069-020-04309-w

Birkholz, S., Muro, M., Jeffrey, P., & Smith, H. M. (2014). Rethinking the relationship between flood risk perception and flood management. *Science of The Total Environment*, *478*, 12–20. https://doi.org/10.1016/j.scitotenv.2014.01.061

Bjorvatn, K. (2000). Urban Infrastructure and Industrialization. *Journal of Urban Economics*, *48*(2), 205–218. https://doi.org/10.1006/juec.1999.2162

Blum, S. C., Silver, R. C., & Poulin, M. J. (2014). Perceiving risk in a dangerous world: Associations between life experiences and risk perceptions. *Social Cognition*, *32*(3), 297.

Bochkovskiy, A. (2020). *Darknet: Open Source Neural Networks in Python.* GitHub.

Bochkovskiy, A., Wang, C. Y., & Liao, H. Y. M. (2020). Yolov4: Optimal speed and accuracy of object detection. *ArXiv Preprint*.

Boeing, G. (2020). A multi-scale analysis of 27,000 urban street networks: Every US city, town, urbanized area, and Zillow neighborhood. *Environment and Planning B: Urban Analytics and City Science*, *47*(4), 590–608. https://doi.org/10.1177/2399808318784595

Botzen, W. J. W., Aerts, J. C. J. H., & van den Bergh, J. C. J. M. (2009). Dependence of flood risk perceptions on socioeconomic and objective risk factors. *Water Resources Research*, *45*(10). https://doi.org/10.1029/2009WR007743

Bradbury, J. A. (1994). Risk Communication in Environmental Restoration Programs. *Risk Analysis*, *14*(3), 357–363. https://doi.org/10.1111/j.1539-6924.1994.tb00252.x

Brown, P., Daigneault, A. J., Tjernström, E., & Zou, W. (2018). Natural disasters, social protection, and risk perceptions. *World Development*, *104*, 310–325. https://doi.org/10.1016/j.worlddev.2017.12.002

Browne, M. W. (2000). Cross-Validation Methods. *Journal of Mathematical Psychology*, *44*(1), 108–132. https://doi.org/10.1006/jmps.1999.1279

Buchecker, M., Salvini, G., di Baldassarre, G., Semenzin, E., Maidl, E., & Marcomini, A. (2013). The role of risk perception in making flood risk management more effective. *Natural Hazards and Earth System Sciences*, *13*(11), 3013–3030. https://doi.org/10.5194/nhess-13-3013-2013

Bustillos Ardaya, A., Evers, M., & Ribbe, L. (2017). What influences disaster risk perception? Intervention measures, flood and landslide risk perception of the population living in flood risk areas in Rio de Janeiro state, Brazil. *International Journal of Disaster Risk Reduction*, *25*, 227–237. https://doi.org/10.1016/j.ijdrr.2017.09.006

Campana, N. A., & Tucci, C. E. M. (2001). Predicting floods from urban development scenarios: case study of the Dilúvio Basin, Porto Alegre, Brazil. *Urban Water*, *3*(1–2), 113–124. https://doi.org/10.1016/S1462-0758(01)00004-8

Campbell, A., Both, A., & Sun, Q. (Chayn). (2019). Detecting and mapping traffic signs from Google Street View images using deep learning and GIS. *Computers,*

Environment and Urban Systems, *77*, 101350. https://doi.org/10.1016/j.compenvurbsys.2019.101350

Careem, M., de Silva, C., de Silva, R., Raschid, L., & Weerawarana, S. (2006). Sahana: Overview of a Disaster Management System. *2006 International Conference on Information and Automation*, 361–366. https://doi.org/10.1109/ICINFA.2006.374152

Carson, J. S. (2003). Model verification and validation. *Proceedings of the Winter Simulation Conference*, 52–58. https://doi.org/10.1109/WSC.2002.1172868

Center for western weather and water extremes. (2021). *CW3E Event Summary: 10-16 November 2021*.

Chaudhary, P., D'Aronco, S., Moy de Vitry, M., Leitão, J. P., & Wegner, J. D. (2019). Flood-water level estimation from social media images. *ISPRS Annals of the Photogrammetry, Remote Sensing and Spatial Information Sciences*, *4*(2/W5), 5–12.

Chetpattananondh, K., Tapoanoi, T., Phukpattaranont, P., & Jindapetch, N. (2014). A self-calibration water level measurement using an interdigital capacitive sensor. *Sensors and Actuators A: Physical*, *209*, 175–182. https://doi.org/10.1016/j.sna.2014.01.040

Chikoto, G. L., Sadiq, A.-A., & Fordyce, E. (2013). Disaster Mitigation and Preparedness. *Nonprofit and Voluntary Sector Quarterly*, *42*(2), 391–410. https://doi.org/10.1177/0899764012452042

Chokmani, K., & Ouarda, T. B. M. J. (2004). Physiographical space-based kriging for regional flood frequency estimation at ungauged sites. *Water Resources Research*, *40*(12). https://doi.org/10.1029/2003WR002983

Church, J. A., & White, N. J. (2011). Sea-Level Rise from the Late 19th to the Early 21st Century. *Surveys in Geophysics*, *32*(4–5), 585–602. https://doi.org/10.1007/s10712-011-9119-1

Cian, F., Marconcini, M., Ceccato, P., & Giupponi, C. (2018). Flood depth estimation by means of high-resolution SAR images and lidar data. *Natural Hazards and Earth System Sciences*, *18*(11), 3063–3084. https://doi.org/10.5194/nhess-18-3063-2018

Cohen, S., Raney, A., Munasinghe, D., Loftis, J. D., Molthan, A., Bell, J., Rogers, L., Galantowicz, J., Brakenridge, G. R., Kettner, A. J., Huang, Y.-F., & Tsang, Y.-P. (2019). The Floodwater Depth Estimation Tool (FwDET v2.0) for improved remote sensing analysis of coastal flooding. *Natural Hazards and Earth System Sciences*, *19*(9), 2053–2065. https://doi.org/10.5194/nhess-19-2053-2019

Colten, C. E., & Sumpter, A. R. (2009). Social memory and resilience in New Orleans. *Natural Hazards*, *48*(3), 355–364. https://doi.org/10.1007/s11069-008-9267-x

Cortes, C., & Vapnik, V. (1995). Support-vector networks. *Machine Learning*, *20*(3), 273–297. https://doi.org/10.1007/BF00994018

Cova, T. J., & Johnson, J. P. (2003). A network flow model for lane-based evacuation routing. *Transportation Research Part A: Policy and Practice*, *37*(7), 579–604. https://doi.org/10.1016/S0965-8564(03)00007-7

Cox, R. , Y. M. , & B. J. E. (2004). Safety of people in flooded streets and floodways. *In National Conference on Hydraulics in Water Engineering*.

Cox, R. J. , S. T. D. , & B. M. J. (2010). *Australian Rainfall & Runoff revision project 10: appropriate safety criteria for people.* (No. 978).

Crager, M. R., & Reitman, M. A. (1991). Running Average Analysis of Clinical Trial Ambulatory Blood Pressure Data. *Biometrics*, *47*(1), 129. https://doi.org/10.2307/2532501

Cutnell, J., & Johnson, K. (1998). *Physics* (2nd ed.). Wiley.

Cvetkovic, V. M., & Martinović, J. (2020). Innovative Solutions for Flood Risk Management. *International Journal of Disaster Risk Management*, *2*(2), 71–99. https://doi.org/10.18485/ijdrm.2020.2.2.5

Dantzig, G. B., & Ramser, J. H. (1959). The Truck Dispatching Problem. *Management Science*, *6*(1), 80–91. https://doi.org/10.1287/mnsc.6.1.80

de Silva, F. N., & Eglese, R. W. (2000). Integrating simulation modelling and GIS: spatial decision support systems for evacuation planning. *Journal of the Operational Research Society*, *51*(4), 423–430. https://doi.org/10.1057/palgrave.jors.2600879

Delgado, D. F. M. (n.d.). *The promotion of instability of a highly-deformed plate under fluid loading and its transition to oscillatory motion*. Cornell University.

Department of Homeland Security, O. of I. G. (2017). *FEMA needs to improve management of its flood mapping programs*.

Dijkstra, E. W. (1959). A note on two problems in connexion with graphs. *Numerische Mathematik, 1*(1), 269–271.

Dong, S., Yu, T., Farahmand, H., & Mostafavi, A. (2020). Bayesian modeling of flood control networks for failure cascade characterization and vulnerability assessment. *Computer-Aided Civil and Infrastructure Engineering*, *35*(7), 668–684. https://doi.org/10.1111/mice.12527

Du, Z.-L., Wang, H.-N., & Zhang, L.-Y. (2008). A Running Average Method for Predicting the Size and Length of a Solar Cycle. *Chinese Journal of Astronomy and Astrophysics*, *8*(4), 477–488. https://doi.org/10.1088/1009-9271/8/4/12

Dunham, M. H. (2006). *Data mining: Introductory and advanced topics.* Pearson Education India.

Dwyer, I., & Owen, C. (2009). Emergency Incident Management: An Evolving Incident Control System Framework. *Journal of Pacific Rim Psychology*, *3*(2), 66–75. https://doi.org/10.1375/prp.3.2.66

Eby, M. (2019, March 21). Understanding FEMA Flood Maps and Limitations. *First Street Foundation*.

Eller, W., Gerber, B. J., & Branch, L. E. (2015). Voluntary Nonprofit Organizations and Disaster Management: Identifying the Nature of Inter-Sector Coordination and Collaboration in Disaster Service Assistance Provision. *Risk, Hazards & Crisis in Public Policy*, *6*(2), 223–238. https://doi.org/10.1002/rhc3.12081

Everingham, M., van Gool, L., Williams, C. K. I., Winn, J., & Zisserman, A. (2010). The Pascal Visual Object Classes (VOC) Challenge. *International Journal of Computer Vision*, *88*(2), 303–338. https://doi.org/10.1007/s11263-009-0275-4

Fan, Q., Yang, J., Hua, G., Chen, B., & Wipf, D. (2017). A generic deep architecture for single image reflection removal and image smoothing. . *The IEEE International Conference on Computer Vision*, 3238–3247.

Farras A. W. (2020). *Auto-thresholding canny edge detection, MATLAB Central File Exchange*.

Federal Emergency Management Agency. (2010). *Are you ready guide*.

Federal Emergency Management Agency. (2016). *Pre-Disaster Recovery Planning Guide for State Governments*.

Federal Highway Administration. (2004). *Manual of Uniform Traffic Control Devices (MUTCD) : Standard Highway Signs.* .

Federal Highway Administration. (2009). *Stop Signs*.

FEINGERSH, T., BENDOR, E., & PORTUGALI, J. (2007). Construction of synthetic spectral reflectance of remotely sensed imagery for planning purposes. *Environmental Modelling & Software*, *22*(3), 335–348. https://doi.org/10.1016/j.envsoft.2005.11.005

Field, A. (2013). *Discovering statistics using SPSS.* Sage Publications.

First Street Foundation. (2019). *FEMA flood maps and limitations*.

Fitzpatrick-Lewis, D., Yost, J., Ciliska, D., & Krishnaratne, S. (2010). Communication about environmental health risks: A systematic review. *Environmental Health*, *9*(1), 67. https://doi.org/10.1186/1476-069X-9-67

Flanagan, J. (2014). Joint Emergency Services Interoperability Programme: working together saving lives. *Journal of Paramedic Practice*, *6*(6), 284–287. https://doi.org/10.12968/jpar.2014.6.6.284

Ford, A., Barr, S., Dawson, R., Virgo, J., Batty, M., & Hall, J. (2019). A multi-scale urban integrated assessment framework for climate change studies: A flooding application. *Computers, Environment and Urban Systems*, *75*, 229–243. https://doi.org/10.1016/j.compenvurbsys.2019.02.005

Forzieri, G., Cescatti, A., e Silva, F. B., & Feyen, L. (2017). Increasing risk over time of weather-related hazards to the European population: a data-driven prognostic study. *The Lancet Planetary Health*, *1*(5), e200–e208. https://doi.org/10.1016/S2542-5196(17)30082-7

Fu, C. Y., Liu, W., Ranga, A., Tyagi, A., & Berg, A. C. (2017). Dssd: Deconvolutional single shot detector. *Arxiv Preprint*.

Fuchs, S., Karagiorgos, K., Kitikidou, K., Maris, F., Paparrizos, S., & Thaler, T. (2017). Flood risk perception and adaptation capacity: a contribution to the socio-hydrology debate. *Hydrology and Earth System Sciences*, *21*(6), 3183–3198. https://doi.org/10.5194/hess-21-3183-2017

Galloway, G. E., Reilly, A., Ryoo, S., Riley, A., Haslam, M., Brody, S., Highfield, W., Gunn, J., Rainey, J., & Parker, S. (2018). *The growing threat of urban flooding: A national challenge.*

Gao, Y., & Mosalam, K. M. (2018). Deep Transfer Learning for Image-Based Structural Damage Recognition. *Computer-Aided Civil and Infrastructure Engineering*, *33*(9), 748–768. https://doi.org/10.1111/mice.12363

Garcia-Molina, H., Joglekar, M., Marcus, A., Parameswaran, A., & Verroios, V. (2016). Challenges in Data Crowdsourcing. *IEEE Transactions on Knowledge and Data Engineering*, *28*(4), 901–911. https://doi.org/10.1109/TKDE.2016.2518669

Garson, G. D. (2012). *Testing statistical assumptions* (2012th ed.). Testing statistical assumptions.

Gebrehiwot, A., Hashemi-Beni, L., Thompson, G., Kordjamshidi, P., & Langan, T. (2019). Deep Convolutional Neural Network for Flood Extent Mapping Using Unmanned Aerial Vehicles Data. *Sensors*, *19*(7), 1486. https://doi.org/10.3390/s19071486

Girshick, R., Donahue, J., Darrell, T., & Malik, J. (2014). Rich Feature Hierarchies for Accurate Object Detection and Semantic Segmentation. *2014 IEEE Conference on Computer Vision and Pattern Recognition*, 580–587. https://doi.org/10.1109/CVPR.2014.81

Giustini, F., Ciotoli, G., Rinaldini, A., Ruggiero, L., & Voltaggio, M. (2019). Mapping the geogenic radon potential and radon risk by using Empirical Bayesian Kriging

regression: A case study from a volcanic area of central Italy. *Science of The Total Environment, 661*, 449–464. https://doi.org/10.1016/j.scitotenv.2019.01.146

Gomes, R., & Straub, J. (2017). *Genetic algorithm for flood detection and evacuation route planning* (M. Velez-Reyes & D. W. Messinger, Eds.; p. 1019816). https://doi.org/10.1117/12.2266474

Goodchild, M. F. (2009). What Problem? Spatial Autocorrelation and Geographic Information Science. *Geographical Analysis*, *41*(4), 411–417. https://doi.org/10.1111/j.1538-4632.2009.00769.x

Google. (2022). *Google Street View*.

GREEN, C. H., TUNSTALL, S. M., & FORDHAM, M. H. (1991). The Risks from Flooding: Which Risks and Whose Perception? *Disasters*, *15*(3), 227–236. https://doi.org/10.1111/j.1467-7717.1991.tb00456.x

Gulli, A., & Pal, S. (2017). *Deep learning with Keras.* (Vols. 978-1-78712-842–2). Packt Publishing Ltd.

Guo, H., Shi, Q., Marinoni, A., Du, B., & Zhang, L. (2021). Deep building footprint update network: A semi-supervised method for updating existing building footprint from bi-temporal remote sensing images. *Remote Sensing of Environment*, *264*, 112589. https://doi.org/10.1016/j.rse.2021.112589

Gupta, A., Kamble, T., & Machiwal, D. (2017). Comparison of ordinary and Bayesian kriging techniques in depicting rainfall variability in arid and semi-arid regions of north-west India. *Environmental Earth Sciences*, *76*(15), 512. https://doi.org/10.1007/s12665-017-6814-3

Haining, R. P. (2001). Spatial Sampling. *International Encyclopedia of the Social and Behavioral Sciences. Oxford: Pergamon.* .

Hair, J. F. , B. W. C. , B. B. J. , & A. R. E. (2010). *Multivariate data analysis: A global perspective*. Prentice Hall.

Han, D., Liu, Q., & Fan, W. (2018). A new image classification method using CNN transfer learning and web data augmentation. *Expert Systems with Applications*, *95*, 43–56. https://doi.org/10.1016/j.eswa.2017.11.028

Hao, W., & Zhili, S. (2020). Improved Mosaic: Algorithms for more Complex Images. *Journal of Physics: Conference Series*, *1684*(1), 012094. https://doi.org/10.1088/1742-6596/1684/1/012094

Hauer, M. E., Evans, J. M., & Mishra, D. R. (2016). Millions projected to be at risk from sea-level rise in the continental United States. *Nature Climate Change*, *6*(7), 691–695. https://doi.org/10.1038/nclimate2961

Hawker, L., Bates, P., Neal, J., & Rougier, J. (2018). Perspectives on Digital Elevation Model (DEM) Simulation for Flood Modeling in the Absence of a High-Accuracy Open Access Global DEM. *Frontiers in Earth Science*, *6*. https://doi.org/10.3389/feart.2018.00233

He, K., Gkioxari, G., Dollár, P., & Girshick, R. (2017a). Mask r-cnnR-CNN. *The IEEE International Conference on Computer Vision.*, 2961–2969.

He, K., Gkioxari, G., Dollár, P., & Girshick, R. (2017b). Mask R-CNN. *ArXiv Preprint*.

He, K., Zhang, X., Ren, S., & Sun, J. (2015). Spatial Pyramid Pooling in Deep Convolutional Networks for Visual Recognition. *IEEE Transactions on Pattern*

Analysis and Machine Intelligence, *37*(9), 1904–1916. https://doi.org/10.1109/TPAMI.2015.2389824

He, M., Chen, C., Zheng, F., Chen, Q., Zhang, J., Yan, H., & Lin, Y. (2021). An efficient dynamic route optimization for urban flooding evacuation based on Cellular Automata. *Computers, Environment and Urban Systems*, *87*, 101622. https://doi.org/10.1016/j.compenvurbsys.2021.101622

Hernández, J. Z., & Serrano, J. M. (2001). Knowledge-based models for emergency management systems. *Expert Systems with Applications*, *20*(2), 173–186. https://doi.org/10.1016/S0957-4174(00)00057-9

Hu, R., Zhang, S., Wang, P., Xu, G., Wang, D., & Qian, Y. (2020). The identification of corn leaf diseases based on transfer learning and data augmentation. *Proceedings of the 2020 3rd International Conference on Computer Science and Software Engineering*, 58–65. https://doi.org/10.1145/3403746.3403905

Hu, T. Y., Armandpour, M., Shrivastava, A., Chang, J. H. R., Koppula, H., & Tuzel, O. (2021). . Synt++: Utilizing Imperfect Synthetic Data to Improve Speech Recognition. *ArXiv Preprint* .

Huang, S., Krysanova, V., & Hattermann, F. (2015). Projections of climate change impacts on floods and droughts in Germany using an ensemble of climate change scenarios. *Regional Environmental Change*, *15*(3), 461–473. https://doi.org/10.1007/s10113-014-0606-z

Huang, X., Wang, C., & Li, Z. (2018). A near real-time flood-mapping approach by integrating social media and post-event satellite imagery. *Annals of GIS*, *24*(2), 113–123. https://doi.org/10.1080/19475683.2018.1450787

Huang, Z., Huang, L., Gong, Y., Huang, C., & Wang, X. (2019). Mask scoring Scoring r-cnnR-CNN. *The IEEE Conference on Computer Vision and Pattern Recognition*, 6409–6418.

Hudson, P., Botzen, W. J. W., & Aerts, J. C. J. H. (2019). Flood insurance arrangements in the European Union for future flood risk under climate and socioeconomic change. *Global Environmental Change*, *58*, 101966. https://doi.org/10.1016/j.gloenvcha.2019.101966

Huibregtse, O. L., Bliemer, M. C. J., & Hoogendoorn, S. P. (2010). Analysis of near-optimal evacuation instructions. *Procedia Engineering*, *3*, 189–203. https://doi.org/10.1016/j.proeng.2010.07.018

Hussain, M., Bird, J. J., & Faria, D. R. (2019). *A Study on CNN Transfer Learning for Image Classification* (pp. 191–202). https://doi.org/10.1007/978-3-319-97982-3_16

Incetas, M. O., Demirci, R., & Yavuzcan, H. G. (2019). Automatic color edge detection with similarity transformation. . *Gazi University Journal of Science*, *32*(2).

Insani, N., Akman, D., Taheri, S., & Hearne, J. (2022). Short-notice flood evacuation plan under dynamic demand in high populated areas. *International Journal of Disaster Risk Reduction*, *74*, 102844. https://doi.org/10.1016/j.ijdrr.2022.102844

Insurance Bureau of Canada. (2021). *British Columbia floods cause $450 million in insured damage*.

Islam, R., Lee, Y., Jaloli, M., Muhammad, I., Zhu, D., Rad, P., Huang, Y., & Quarles, J. (2020). Automatic Detection and Prediction of Cybersickness Severity using Deep Neural Networks from user's Physiological Signals. *2020 IEEE International Symposium on Mixed and Augmented Reality (ISMAR)*, 400–411. https://doi.org/10.1109/ISMAR50242.2020.00066

Javadi, S., Maghami, A., & Hosseini, S. M. (2021). A deep learning approach based on a data-driven tool for classification and prediction of thermoelastic wave's band structures for phononic crystals. *Mechanics of Advanced Materials and Structures*, 1–14. https://doi.org/10.1080/15376494.2021.1983088

Ju, Luo, Wang, Hui, & Chang. (2019). The Application of Improved YOLO V3 in Multi-Scale Target Detection. *Applied Sciences*, *9*(18), 3775. https://doi.org/10.3390/app9183775

Kang, L.-W., Wang, I.-S., Chou, K.-L., Chen, S.-Y., & Chang, C.-Y. (2019). Image-Based Real-Time Fire Detection using Deep Learning with Data Augmentation for Vision-Based Surveillance Applications. *2019 16th IEEE International Conference on Advanced Video and Signal Based Surveillance (AVSS)*, 1–4. https://doi.org/10.1109/AVSS.2019.8909899

Kankanamge, N., Yigitcanlar, T., Goonetilleke, A., & Kamruzzaman, M. (2019). Can volunteer crowdsourcing reduce disaster risk? A systematic review of the literature. *International Journal of Disaster Risk Reduction*, *35*, 101097. https://doi.org/10.1016/j.ijdrr.2019.101097

Karich, P., & Schröder, S. (2014). *Graphhopper*.

Kenward, T. (2000). Effects of Digital Elevation Model Accuracy on Hydrologic Predictions. *Remote Sensing of Environment*, *74*(3), 432–444. https://doi.org/10.1016/S0034-4257(00)00136-X

KHOU 11. (2020, August). *Your photos of stop signs could help build better flood maps*. YouTube.

Kido, D., Fukuda, T., & Yabuki, N. (2020). Diminished reality system with real-time object detection using deep learning for onsite landscape simulation during redevelopment. *Environmental Modelling & Software*, *131*, 104759. https://doi.org/10.1016/j.envsoft.2020.104759

Kingma, D. P., & Ba, J. (2014). Adam: A method for stochastic optimization. *ArXiv Preprint*.

Koirala, A., Walsh, K. B., Wang, Z., & McCarthy, C. (2019). Deep learning for real-time fruit detection and orchard fruit load estimation: benchmarking of 'MangoYOLO.' *Precision Agriculture*, *20*(6), 1107–1135. https://doi.org/10.1007/s11119-019-09642-0

Krivoruchko, K. (2012). Empirical Bayesian kriging. *ArcUser Fall*, *6*(10).

Kulp, S. A., & Strauss, B. H. (2019). New elevation data triple estimates of global vulnerability to sea-level rise and coastal flooding. *Nature Communications*, *10*(1), 4844. https://doi.org/10.1038/s41467-019-12808-z

Kwan, M.-P., & Ransberger, D. M. (2010). LiDAR assisted emergency response: Detection of transport network obstructions caused by major disasters. *Computers,*

Environment and Urban Systems, *34*(3), 179–188. https://doi.org/10.1016/j.compenvurbsys.2010.02.001

Lerner, J., Wagner, D., & Zweig, K. (2009). *Algorithmics of Large and Complex Networks: Design, Analysis, and Simulation: Vol. LNCS 5515*. Springer.

Li, T., Xie, N., Zeng, C., Zhou, W., Zheng, L., Jiang, Y., Yang, Y., Ha, H.-Y., Xue, W., Huang, Y., Chen, S.-C., Navlakha, J., & Iyengar, S. S. (2018). Data-Driven Techniques in Disaster Information Management. *ACM Computing Surveys*, *50*(1), 1–45. https://doi.org/10.1145/3017678

Li, X., Yin, P., Zhi, Y., & Duan, C. (2020). Vertical Lane Line Detection Technology Based on Hough Transform. *IOP Conference Series: Earth and Environmental Science*, *440*(3), 032126. https://doi.org/10.1088/1755-1315/440/3/032126

Li, Z., Wang, C., Emrich, C. T., & Guo, D. (2018). A novel approach to leveraging social media for rapid flood mapping: a case study of the 2015 South Carolina floods. *Cartography and Geographic Information Science*, *45*(2), 97–110. https://doi.org/10.1080/15230406.2016.1271356

Liang, J. (2020). *Canny edge detector tutorial*.

Lim Jr, H., Lim, M. B., & PIANTANAKULCHAI, M. (2013). A review of recent studies on flood evacuation planning. *Journal of the Eastern Asia Society for Transportation Studies , 10*, 147–162.

Lin, T. Y., Dollár, P., Girshick, R., He, K., Hariharan, B., & & Belongie, S. (2017). Feature pyramid networks for object detection. *The IEEE Conference on Computer Vision and Pattern Recognition*, 2117–2125.

Lin, T.-Y., Maire, M., Belongie, S., Hays, J., Perona, P., Ramanan, D., Dollár, P., & Zitnick, C. L. (2014). *Microsoft COCO: Common Objects in Context* (pp. 740–755). https://doi.org/10.1007/978-3-319-10602-1_48

Lindell, M. K., & Hwang, S. N. (2008). Households' Perceived Personal Risk and Responses in a Multihazard Environment. *Risk Analysis*, *28*(2), 539–556. https://doi.org/10.1111/j.1539-6924.2008.01032.x

Lindell, M., & Perry, R. (2004). *Communicating Environmental Risk in Multiethnic Communities*. SAGE Publications, Inc. https://doi.org/10.4135/9781452229188

Liu S., Qi L., Qin H., Shi J., & Jia J. (2018). Path Aggregation Network for Instance Segmentation. *Arxiv Preprint*.

Liu, W., Anguelov, D., Erhan, D., Szegedy, C., Reed, S., Fu, C.-Y., & Berg, A. C. (2016). *SSD: Single Shot MultiBox Detector* (pp. 21–37). https://doi.org/10.1007/978-3-319-46448-0_2

Liu, Y., Hatayama, M., & Okada, N. (2006). Development of an adaptive evacuation route algorithm under flood disaster. *49 Th Annuals of Disaster Prevention Research Institute*, 189–195.

Long, J., Shelhamer, E., & Darrell, T. (2015a). Fully convolutional networks for semantic segmentation. *The IEEE Conference on Computer Vision and Pattern Recognition*, 3431–3440.

Long, J., Shelhamer, E., & Darrell, T. (2015b). Fully convolutional networks for semantic segmentation. *Proceedings of the IEEE Conference on Computer Vision and Pattern Recognition*.

Lu, Q. (2006). *Capacity constrained routing algorithms for evacuation route planning*.

Lyons, M. B., Keith, D. A., Phinn, S. R., Mason, T. J., & Elith, J. (2018). A comparison of resampling methods for remote sensing classification and accuracy assessment. *Remote Sensing of Environment, 208,* 145–153. https://doi.org/10.1016/j.rse.2018.02.026

Lyu, Y., Bai, L., & Huang, X. (2019). Road Segmentation using CNN and Distributed LSTM. *2019 IEEE International Symposium on Circuits and Systems (ISCAS)*, 1–5. https://doi.org/10.1109/ISCAS.2019.8702174

Ma, J., Duan, S., Zhang, Y., Wang, J., Wang, Z., Li, R., Li, Y., Zhang, L., & Ma, H. (2020). Efficient Deep Learning Architecture for Detection and Recognition of Thyroid Nodules. *Computational Intelligence and Neuroscience, 2020,* 1–15. https://doi.org/10.1155/2020/1242781

Mai, T., Mushtaq, S., Reardon-Smith, K., Webb, P., Stone, R., Kath, J., & An-Vo, D.-A. (2020). Defining flood risk management strategies: A systems approach. *International Journal of Disaster Risk Reduction, 47,* 101550. https://doi.org/10.1016/j.ijdrr.2020.101550

Mao, X., Chow, J. K., Su, Z., Wang, Y.-H., Li, J., Wu, T., & Li, T. (2021). Deep learning-enhanced extraction of drainage networks from digital elevation models. *Environmental Modelling & Software, 144,* 105135. https://doi.org/10.1016/j.envsoft.2021.105135

Marche, C., Lessard, G., & el Gharbi, B. (1990). Kriging technique for river flood representation. *Journal of Hydraulic Research*, *28*(5), 629–643. https://doi.org/10.1080/00221689009499051

Marincioni, F. (2007). Information technologies and the sharing of disaster knowledge: the critical role of professional culture. *Disasters*, *31*(4), 459–476. https://doi.org/10.1111/j.1467-7717.2007.01019.x

Mark, O., Weesakul, S., Apirumanekul, C., Aroonnet, S. B., & Djordjević, S. (2004). Potential and limitations of 1D modelling of urban flooding. *Journal of Hydrology*, *299*(3–4), 284–299. https://doi.org/10.1016/j.jhydrol.2004.08.014

McCoy, M. D. (2017). Geospatial Big Data and archaeology: Prospects and problems too great to ignore. *Journal of Archaeological Science*, *84*, 74–94. https://doi.org/10.1016/j.jas.2017.06.003

McDougall, K., & Temple-Watts, P. (2012, July 16). The use of LiDAR and volunteered geographic information to map flood extents and inundation. *ISPRS Annals of the Photogrammetry, Remote Sensing and Spatial Information Sciences*.

Meesuk, V., Vojinovic, Z., & Mynett, A. E. (2017). Extracting inundation patterns from flood watermarks with remote sensing SfM technique to enhance urban flood simulation: The case of Ayutthaya, Thailand. *Computers, Environment and Urban Systems*, *64*, 239–253. https://doi.org/10.1016/j.compenvurbsys.2017.03.004

Mehta, A. M., Bruns, A., & Newton, J. (2017). Trust, but verify: social media models for disaster management. *Disasters*, *41*(3), 549–565. https://doi.org/10.1111/disa.12218

Mihunov, V. v., Lam, N. S. N., Zou, L., Wang, Z., & Wang, K. (2020). Use of Twitter in disaster rescue: lessons learned from Hurricane Harvey. *International Journal of Digital Earth*, *13*(12), 1454–1466. https://doi.org/10.1080/17538947.2020.1729879

Mills, E. (2005). Insurance in a Climate of Change. *Science*, *309*(5737), 1040–1044. https://doi.org/10.1126/science.1112121

Mishra, A., Mukherjee, S., Merz, B., Singh, V. P., Wright, D. B., Villarini, G., Paul, S., Kumar, D. N., Khedun, C. P., Niyogi, D., Schumann, G., & Stedinger, J. R. (2022). An Overview of Flood Concepts, Challenges, and Future Directions. *Journal of Hydrologic Engineering*, *27*(6). https://doi.org/10.1061/(ASCE)HE.1943-5584.0002164

Mizutori, M., & Guha-Sapir, D. (2018). *Economic losses, poverty and disasters 1998–2017*.

Mol, J. M., Botzen, W. J. W., & Blasch, J. E. (2022). After the virtual flood: Risk perceptions and flood preparedness after virtual reality risk communication. *Judgment and Decision Making*, *17*(1), 189–214. https://doi.org/10.1017/S1930297500009074

Naejin Kong, Yu-Wing Tai, & Shin, J. S. (2014). A Physically-Based Approach to Reflection Separation: From Physical Modeling to Constrained Optimization. *IEEE Transactions on Pattern Analysis and Machine Intelligence*, *36*(2), 209–221. https://doi.org/10.1109/TPAMI.2013.45

Nakamoto, S., Tanioka, R., & Yoshino, T. (2017). Proposal of Disaster Preparedness Education System by Repeated Disaster Experiences and Countermeasures Using Virtual Reality. *IPSJ Kansai*, 6.

Nath, N. D., & Behzadan, A. H. (2020). Deep Convolutional Networks for Construction Object Detection Under Different Visual Conditions. *Frontiers in Built Environment*, *6*. https://doi.org/10.3389/fbuil.2020.00097

National Oceanic and Atmospheric Administration. (2021). *National Oceanic And Atmospheric Administration's National Weather Service*.

National Oceanic and Atmospheric Administration. (2022, October 24). *National Weather Service*.

National Weather Service Team. (2021). *National weather service central region supplement 02-2002. Applicable to NWSI 10-922*. Weather Forecast Office Hydrologic Products Specification.

Nezhad, M. K., Chokmani, K., Ouarda, T. B. M. J., Barbet, M., & Bruneau, P. (2010). Regional flood frequency analysis using residual kriging in physiographical space. *Hydrological Processes*, n/a-n/a. https://doi.org/10.1002/hyp.7631

Ning, H., Li, Z., Ye, X., Wang, S., Wang, W., & Huang, X. (2022). Exploring the vertical dimension of street view image based on deep learning: a case study on lowest floor elevation estimation. *International Journal of Geographical Information Science*, *36*(7), 1317–1342. https://doi.org/10.1080/13658816.2021.1981334

Niu, J., Chen, Y., Yu, X., Li, Z., & Gao, H. (2020). Data Augmentation on Defect Detection of Sanitary Ceramics. *IECON 2020 The 46th Annual Conference of the IEEE Industrial Electronics Society*, 5317–5322. https://doi.org/10.1109/IECON43393.2020.9254518

Nunn, P. D., Aalbersberg, W., Lata, S., & Gwilliam, M. (2014). Beyond the core: community governance for climate-change adaptation in peripheral parts of Pacific Island Countries. *Regional Environmental Change*, *14*(1), 221–235. https://doi.org/10.1007/s10113-013-0486-7

Odli, Z. S. M., Izhar, T. N. T., Razak, A. R. A., Yusuf, S. Y., Zakarya, I. A., Saad, F. N. M., & Nor, M. Z. M. (2016). Development of portable water level sensor for flood management system. *ARPN Journal of Engineering and Applied Sciences*, *11*(8), 5352–5357.

O'Loughlin, F. E., Paiva, R. C. D., Durand, M., Alsdorf, D. E., & Bates, P. D. (2016). A multi-sensor approach towards a global vegetation corrected SRTM DEM product. *Remote Sensing of Environment*, *182*, 49–59. https://doi.org/10.1016/j.rse.2016.04.018

O'Neill, E., Brereton, F., Shahumyan, H., & Clinch, J. P. (2016). The Impact of Perceived Flood Exposure on Flood-Risk Perception: The Role of Distance. *Risk Analysis*, *36*(11), 2158–2186. https://doi.org/10.1111/risa.12597

Ooi, S., Tanimoto, T., & Sano, M. (2019). Virtual Reality Fire Disaster Training System for Improving Disaster Awareness. *Proceedings of the 2019 8th International*

Conference on Educational and Information Technology, 301–307. https://doi.org/10.1145/3318396.3318431

OpenCV Dev Team. (2019). *Canny edge detector*. .

Padilla, R., Netto, S. L., & da Silva, E. A. B. (2020). A Survey on Performance Metrics for Object-Detection Algorithms. *2020 International Conference on Systems, Signals and Image Processing (IWSSIP)*, 237–242. https://doi.org/10.1109/IWSSIP48289.2020.9145130

Palla, A., Colli, M., Candela, A., Aronica, G. T., & Lanza, L. G. (2018). Pluvial flooding in urban areas: the role of surface drainage efficiency. *Journal of Flood Risk Management*, *11*, S663–S676. https://doi.org/10.1111/jfr3.12246

Pan, J., Yin, Y., Xiong, J., Luo, W., Gui, G., & Sari, H. (2018). Deep Learning-Based Unmanned Surveillance Systems for Observing Water Levels. *IEEE Access*, *6*, 73561–73571. https://doi.org/10.1109/ACCESS.2018.2883702

Park, S., Baek, F., Sohn, J., & Kim, H. (2021). Computer Vision–Based Estimation of Flood Depth in Flooded-Vehicle Images. *Journal of Computing in Civil Engineering*, *35*(2). https://doi.org/10.1061/(ASCE)CP.1943-5487.0000956

Peacock, W. G., Brody, S. D., & Highfield, W. (2005). Hurricane risk perceptions among Florida's single family homeowners. *Landscape and Urban Planning*, *73*(2–3), 120–135. https://doi.org/10.1016/j.landurbplan.2004.11.004

Pedersini, F., Sarti, A., & Tubaro, S. (1997). Estimation and compensation of subpixel edge localization error. *IEEE Transactions on Pattern Analysis and Machine Intelligence*, *19*(11), 1278–1284. https://doi.org/10.1109/34.632986

Pei-Yung Hsiao, Chia-Hsiung Chen, Shin-Shian Chou, Le-Tien Li, & Sao-Jie Chen. (2006). A parameterizable digital-approximated 2D Gaussian smoothing filter for edge detection in noisy image. *2006 IEEE International Symposium on Circuits and Systems*, 4. https://doi.org/10.1109/ISCAS.2006.1693303

Pi, Y., Nath, N. D., & Behzadan, A. H. (2020a). Convolutional neural networks for object detection in aerial imagery for disaster response and recovery. *Advanced Engineering Informatics*, *43*, 101009. https://doi.org/10.1016/j.aei.2019.101009

Pi, Y., Nath, N. D., & Behzadan, A. H. (2020b). Convolutional neural networks for object detection in aerial imagery for disaster response and recovery. *Advanced Engineering Informatics*, *43*, 101009. https://doi.org/10.1016/j.aei.2019.101009

PIERCE, D. A. (1971). Least squares estimation in the regression model with autoregressive-moving average errors. *Biometrika*, *58*(2), 299–312. https://doi.org/10.1093/biomet/58.2.299

Planet OpenStreetMap. (2021). *Planet dump [Data file from June 4th. 2017 dumps]*.

Powers, D. M. W. (2011). Evaluation: from precision, recall and F-measure to ROC, informedness, markedness and correlation. *ArXiv Preprint*.

Public Safety Canada. (2010). *Emergency management planning guide 2010–2011*.

Puttinaovarat, S., & Horkaew, P. (2020). Flood Forecasting System Based on Integrated Big and Crowdsource Data by Using Machine Learning Techniques. *IEEE Access*, *8*, 5885–5905. https://doi.org/10.1109/ACCESS.2019.2963819

Qasim, S., Nawaz Khan, A., Prasad Shrestha, R., & Qasim, M. (2015). Risk perception of the people in the flood prone Khyber Pukhthunkhwa province of Pakistan.

International Journal of Disaster Risk Reduction, *14*, 373–378. https://doi.org/10.1016/j.ijdrr.2015.09.001

Rachel, C. (2013). *Overwhelming risk: Rethinking flood insurance in a world of rising seas*.

Rana, I. A., & Routray, J. K. (2018). Integrated methodology for flood risk assessment and application in urban communities of Pakistan. *Natural Hazards*, *91*(1), 239–266. https://doi.org/10.1007/s11069-017-3124-8

Ravi Shankar, A., Fernandez-Marquez, J. L., Pernici, B., Scalia, G., Mondardini, M. R., & Serugendo, G. (2019). CROWD4EMS: A CROWDSOURCING PLATFORM FOR GATHERING AND GEOLOCATING SOCIAL MEDIA CONTENT IN DISASTER RESPONSE. *The International Archives of the Photogrammetry, Remote Sensing and Spatial Information Sciences, XLII-3/W8*, 331–340. https://doi.org/10.5194/isprs-archives-XLII-3-W8-331-2019

Redmon, J., & Farhadi, A. (2018). YOLOv3: An incremental improvement. *ArXiv Preprint*.

Ren, S., He, K., Girshick, R., & Sun, J. (2015). Faster r-cnnR-CNN: Towards real-time object detection with region proposal networks. . *Advances in Neural Information Processing Systems*, 91–99. https://doi.org/http://refhub.elsevier.com/S1474-0346(19)30582-8/h0115.

Ren, S., He, K., Girshick, R., & Sun, J. (2017). Faster R-CNN: Towards Real-Time Object Detection with Region Proposal Networks. *IEEE Transactions on Pattern*

Analysis and Machine Intelligence, *39*(6), 1137–1149. https://doi.org/10.1109/TPAMI.2016.2577031

Rentschler, J., & Salhab, M. (2020). *People in Harm's Way : Flood Exposure and Poverty in 189 Countries* (No. 9447; Policy Research Working Paper).

Reser, J., Bradley, G. L., Glendon, Ian., Ellul, M., & Challaghan, R. (2012). *Public risk perceptions, understandings and responses to climate change*.

Rodriguez Castro, D., Roucour, S., Archambeau, P., Cools, M., Erpicum, S., Habchi, I., Hardy, J., Pirotton, M., Weber, L., Teller, J., & Dewals, B. (2022). Modelling direct flood losses: what can we learn from the July 2021 flood in the Meuse basin (Belgium)? *KAHR Science Conference*.

Rong, W., Li, Z., Zhang, W., & Sun, L. (2014). An improved Canny edge detection algorithm. *2014 IEEE International Conference on Mechatronics and Automation*, 577–582. https://doi.org/10.1109/ICMA.2014.6885761

Ruby, S., Copeland, D. B., & Thomas, D. (2020). *Agile web development with rails 6*. Pragmatic Bookshelf.

Russakovsky, O., Deng, J., Su, H., Krause, J., Satheesh, S., Ma, S., Huang, Z., Karpathy, A., Khosla, A., Bernstein, M., Berg, A. C., & Fei-Fei, L. (2015). ImageNet Large Scale Visual Recognition Challenge. *International Journal of Computer Vision*, *115*(3), 211–252. https://doi.org/10.1007/s11263-015-0816-y

Russell, S., & Norvig, P. (2002). *Artificial Intelligence. A Modern Approach* (Second Edition).

Ryu, J., & Ohno, R. (2007). A Novel Room Re-Layout Design Tool for Preparedness of Earthquake Disaster Using Real-Time Physics Simulation and Force-Feedback Interface. In *Computer-Aided Architectural Design Futures (CAADFutures) 2007* (pp. 541–554). Springer Netherlands. https://doi.org/10.1007/978-1-4020-6528-6_40

Sahin, V., & Hall, M. J. (1996). The effects of afforestation and deforestation on water yields. *Journal of Hydrology*, *178*(1–4), 293–309. https://doi.org/10.1016/0022-1694(95)02825-0

Saldaña, J. (2021). *The coding manual for qualitative researchers.* (Third Edition). Sage Publications Ltd.

Salmonsson, A. (2015). *MIKE 21 FM in Urban Flood Risk Analysis: A comparative study relating to the MIKE 21 Classic model* [Division of River Engineering]. Royal Institute of Technology (KTH).

Salmoral, G., Rivas Casado, M., Muthusamy, M., Butler, D., Menon, P., & Leinster, P. (2020). Guidelines for the Use of Unmanned Aerial Systems in Flood Emergency Response. *Water*, *12*(2), 521. https://doi.org/10.3390/w12020521

Sansom, G. T., Aarvig, K., Sansom, L., Thompson, C., Fawkes, L., & Katare, A. (2021). Understanding Risk Communication and Willingness to Follow Emergency Recommendations Following Anthropogenic Disasters. *Environmental Justice*, *14*(2), 159–167. https://doi.org/10.1089/env.2020.0050

Sarel, B., & Irani, M. (2004). *Separating Transparent Layers through Layer Information Exchange* (pp. 328–341). https://doi.org/10.1007/978-3-540-24673-2_27

Saroj, A., & Pal, S. (2020). Use of social media in crisis management: A survey. *International Journal of Disaster Risk Reduction*, *48*, 101584. https://doi.org/10.1016/j.ijdrr.2020.101584

Sayyady, F., & Eksioglu, S. D. (2010). Optimizing the use of public transit system during no-notice evacuation of urban areas. *Computers & Industrial Engineering*, *59*(4), 488–495. https://doi.org/10.1016/j.cie.2010.06.001

Sazara, C., Cetin, M., & Iftekharuddin, K. M. (2019). Detecting floodwater on roadways from image data with handcrafted features and deep transfer learning. *2019 IEEE Intelligent Transportation Systems Conference (ITSC)*, 804–809. https://doi.org/10.1109/ITSC.2019.8917368

Schumann, G. J.-P. (2014). Fight floods on a global scale. *Nature*, *507*(7491), 169–169. https://doi.org/10.1038/507169e

See, L. (2019). A Review of Citizen Science and Crowdsourcing in Applications of Pluvial Flooding. *Frontiers in Earth Science*, *7*. https://doi.org/10.3389/feart.2019.00044

Sermet, Y., & Demir, I. (2019). Flood action VR. *ACM SIGGRAPH 2019 Posters*, 1–2. https://doi.org/10.1145/3306214.3338550

Seyrfar, A., Ataei, H., Movahedi, A., & Derrible, S. (2021). Data-Driven Approach for Evaluating the Energy Efficiency in Multifamily Residential Buildings. *Practice Periodical on Structural Design and Construction*, *26*(2). https://doi.org/10.1061/(ASCE)SC.1943-5576.0000555

Shaghaghian, Z., & Yan, W. (2019). Application of Deep Learning in Generating Desired Design Options: Experiments Using Synthetic Training Dataset. *ArXiv Preprint*.

Shinar, D., Dewar, R. E., Summala, H., & Zakowska, L. (2003). Traffic sign symbol comprehension: a cross-cultural study. *Ergonomics*, *46*(15), 1549–1565. https://doi.org/10.1080/0014013032000121615

Short, J. F. (1984). The Social Fabric at Risk: Toward the Social Transformation of Risk Analysis. *American Sociological Review*, *49*(6), 711. https://doi.org/10.2307/2095526

Siegrist, M., & Gutscher, H. (2006). Flooding Risks: A Comparison of Lay People's Perceptions and Expert's Assessments in Switzerland. *Risk Analysis*, *26*(4), 971–979. https://doi.org/10.1111/j.1539-6924.2006.00792.x

Simonyan, K., & Zisserman, A. (2014). Very deep convolutional networks for large-scale image recognition. *ArXiv Preprint*.

Siswanto, T., Shofiati, R., & Hartini, H. (2018). Acceptance and Utilization of Technology (UTAUT) as a Method of Technology Acceptance Model of Mitigation Disaster Website. *IOP Conference Series: Earth and Environmental Science*, *106*, 012011. https://doi.org/10.1088/1755-1315/106/1/012011

Sjöberg, L., & Wåhlberg, A. af. (2002). Risk Perception and New Age Beliefs. *Risk Analysis*, *22*(4), 751–764. https://doi.org/10.1111/0272-4332.00066

Slovic, P. (2000). The perception of risk. *Earthscan Publications*.

Smith, A. B. (2020a). *2010-2019: A landmark decade of US billion-dollar weather and climate disasters.* .

Smith, A. B. (2020b). *2010-2019: A landmark decade of US billion-dollar weather and climate disasters*.

Sobel, I. (1978). Neighborhood coding of binary images for fast contour following and general binary array processing. *Computer Graphics and Image Processing*, *8*(1), 127–135. https://doi.org/10.1016/S0146-664X(78)80020-3

Song, Z., Zhang, H., & Dolan, C. (2020). Promoting Disaster Resilience: Operation Mechanisms and Self-Organizing Processes of Crowdsourcing. *Sustainability*, *12*(5), 1862. https://doi.org/10.3390/su12051862

Stahl, B. C., Schroeder, D., & Rodrigues, R. (2023). *AI for Good and the SDGs* (pp. 95–106). https://doi.org/10.1007/978-3-031-17040-9_8

Stepanov, A., & Smith, J. M. (2009). Multi-objective evacuation routing in transportation networks. *European Journal of Operational Research*, *198*(2), 435–446. https://doi.org/10.1016/j.ejor.2008.08.025

Sullivan-Wiley, K. A., & Short Gianotti, A. G. (2017). Risk Perception in a Multi-Hazard Environment. *World Development*, *97*, 138–152. https://doi.org/10.1016/j.worlddev.2017.04.002

Sun, X., Mein, R. G., Keenan, T. D., & Elliott, J. F. (2000). Flood estimation using radar and raingauge data. *Journal of Hydrology*, *239*(1–4), 4–18. https://doi.org/10.1016/S0022-1694(00)00350-4

Tammina, S. (2019). Transfer learning using VGG-16 with Deep Convolutional Neural Network for Classifying Images. *International Journal of Scientific and Research Publications (IJSRP), 9*(10), p9420. https://doi.org/10.29322/IJSRP.9.10.2019.p9420

Tan, M., & Le, Q. (2019). Efficientnet: Rethinking model scaling for convolutional neural networks. *International Conference on Machine Learning*, 6105–6114.

Tan, M., Pang, R., & Le, Q. V. (2020). Efficientdet: Scalable and efficient object detection. *Proceedings of the IEEE/CVF Conference on Computer Vision and Pattern Recognition*.

Tanyeri, U., Kılıçaslan, M., & Demirci, R. (2019). Canny edge detector with half entropy. *2019 3rd International Symposium on Multidisciplinary Studies and Innovative Technologies (ISMSIT). IEEE.*, 1–4.

Tellman, B., Sullivan, J. A., Kuhn, C., Kettner, A. J., Doyle, C. S., Brakenridge, G. R., Erickson, T. A., & Slayback, D. A. (2021). Satellite imaging reveals increased proportion of population exposed to floods. *Nature*, *596*(7870), 80–86. https://doi.org/10.1038/s41586-021-03695-w

Texas General Land Office. (2021). *State of Texas CDBG mitigation (CDBG-MIT) action plan: Building stronger for a resilient future*.

The Texas Water Development Board (TWDB). (2020, April 9). *Flood Planning*.

Thompson, S., Altay, N., III, W. G. G., & Lapetina, J. (2006). Improving disaster response efforts with decision support systems. *International Journal of Emergency Management*, *3*(4), 250. https://doi.org/10.1504/IJEM.2006.011295

Thüring, M., & Mahlke, S. (2007). Usability, aesthetics and emotions in human–technology interaction. *International Journal of Psychology, 42*(4), 253–264. https://doi.org/10.1080/00207590701396674

Töyrä, J., Pietroniro, A., Martz, L. W., & Prowse, T. D. (2002). A multi-sensor approach to wetland flood monitoring. *Hydrological Processes, 16*(8), 1569–1581. https://doi.org/10.1002/hyp.1021

Tremblay, J., Prakash, A., Acuna, D., Brophy, M., Jampani, V., Anil, C., & Birchfield, S. (2018). Training deep networks with synthetic data: Bridging the reality gap by domain randomization. *The IEEE Conference on Computer Vision and Pattern Recognition Workshops*, 969–977.

Turpin, A., & Scholer, F. (2006). User performance versus precision measures for simple search tasks. *Proceedings of the 29th Annual International ACM SIGIR Conference on Research and Development in Information Retrieval - SIGIR '06*, 11. https://doi.org/10.1145/1148170.1148176

Tyler, J., & Sadiq, A.-A. (2018). Friends and family vs. government: who does the public rely on more to prepare for natural disasters? *Environmental Hazards, 17*(3), 234–250. https://doi.org/10.1080/17477891.2018.1425204

Ulil, M., Kamal, A., Suciati, N., & Hidayati S. C. (2021). Calculation of Handwriting Mathematics Expressions on Mobile Devices Using Efficientdet-Lite0 And Reverse Polish Notation. *Journal on Machine Learning and Computational Intelligence (JMLCI), 1*(1).

United States Census Bureau. (2019, June). *Coastline America*.

United States Geological Survey. (2019). *Introducing the next generation of USGS water data for the nation*.

Viavattene, C., Fadipe, D., Old, J., Thompson, V., & Thorburn, K. (2022). Estimation of Scottish Pluvial Flooding Expected Annual Damages Using Interpolation Techniques. *Water*, *14*(3), 308. https://doi.org/10.3390/w14030308

Vincent, R., & Folorunso, O. (2009). A Descriptive Algorithm for Sobel Image Edge Detection. *Proceedings of Informing Science & IT Education Conference (InSITE)*.

Vousdoukas, M. I., Mentaschi, L., Hinkel, J., Ward, P. J., Mongelli, I., Ciscar, J.-C., & Feyen, L. (2020). Economic motivation for raising coastal flood defenses in Europe. *Nature Communications*, *11*(1), 2119. https://doi.org/10.1038/s41467-020-15665-3

Wachinger, G. , R. O. , B. C. , C. T. , D. M. B. , D. L. , . . . & P. L. (2010). *Risk perception and natural hazards*.

Wada, K. (2016). *LabelMe: Image Polygonal Annotation with Python*. GitHub.

Walker, J. P., & Willgoose, G. R. (1999). On the effect of digital elevation model accuracy on hydrology and geomorphology. *Water Resources Research*, *35*(7), 2259–2268. https://doi.org/10.1029/1999WR900034

Wan, R., Shi, B., Hwee, T. A., & Kot, A. C. (2016). Depth of field guided reflection removal. *2016 IEEE International Conference on Image Processing (ICIP)*, 21–25. https://doi.org/10.1109/ICIP.2016.7532311

Wang, R. (2013). *Canny edge detection.*

Wang, T. (2021). Counting the financial cost of deadly flooding in China's central city of Zhengzhou. . *South China Morning Post*.

Wang, X., Wang, X., Zhai, J., Li, X., Huang, H., Li, C., Zheng, J., & Sun, H. (2017). Improvement to flooding risk assessment of storm surges by residual interpolation in the coastal areas of Guangdong Province, China. *Quaternary International*, *453*, 1–14. https://doi.org/10.1016/j.quaint.2016.12.025

Wang, Z., & Zlatanova, S. (2013). *Taxonomy of Navigation for First Responders* (pp. 297–315). https://doi.org/10.1007/978-3-642-34203-5_17

World Bank Group. (2021). *Floods and droughts: An epic response to these hazards in the era of climate change*.

Xi, M., & Smith, S. P. (2014). Simulating cooperative fire evacuation training in a virtual environment using gaming technology. *2014 IEEE Virtual Reality (VR)*, 139–140. https://doi.org/10.1109/VR.2014.6802090

Xu, Z., Wang, S., Stanislawski, L. V., Jiang, Z., Jaroenchai, N., Sainju, A. M., Shavers, E., Usery, E. L., Chen, L., Li, Z., & Su, B. (2021). An attention U-Net model for detection of fine-scale hydrologic streamlines. *Environmental Modelling & Software*, *140*, 104992. https://doi.org/10.1016/j.envsoft.2021.104992

Yadav, M., Sakib, M. N., Feng, K., Chaspari, T., & Behzadan, A. (2019). Virtual reality interfaces and population-specific models to mitigate public speaking anxiety. *2019 8th International Conference on Affective Computing and Intelligent Interaction (ACII)*, 1–7. https://doi.org/10.1109/ACII.2019.8925509

Zhang, K., Gann, D., Ross, M., Robertson, Q., Sarmiento, J., Santana, S., Rhome, J., & Fritz, C. (2019). Accuracy assessment of ASTER, SRTM, ALOS, and TDX DEMs for Hispaniola and implications for mapping vulnerability to coastal flooding. *Remote Sensing of Environment*, *225*, 290–306. https://doi.org/10.1016/j.rse.2019.02.028

Zhang, W., Villarini, G., Vecchi, G. A., & Smith, J. A. (2018). Urbanization exacerbated the rainfall and flooding caused by hurricane Harvey in Houston. *Nature*, *563*(7731), 384–388. https://doi.org/10.1038/s41586-018-0676-z

Zhu, L., Xie, Z., Liu, L., Tao, B., & Tao, W. (2021). IoU-uniform R-CNN: Breaking through the limitations of RPN. *Pattern Recognition*, *112*, 107816. https://doi.org/10.1016/j.patcog.2021.107816

Zhu, Z., & Brilakis, I. (2009). Automated Detection of Concrete Columns from Visual Data. *Computing in Civil Engineering (2009)*, 135–145. https://doi.org/10.1061/41052(346)14

APPENDIX A

A SURVEY FOR COMMUNITY NEEDS ASSESSMENT IN FLOOD EVENTS

In this section, the questions designed for the community survey are presented which are approved by Institutional Review Board (IRB) IRB2019-1506 on January 22, 2020.

1. What is your date of birth? (Note: you must be 18 years or older to participate in this study.)
2. Please enter you ZIP code.
3. Do you have prior first-hand experience with any type of flood event (i.e., hurricane, tropical storm, flood, storm surge, ...)?
    a. Yes
    b. No
    c. Don’t know
4. How many flood events have affected you personally (e.g., place of residence or work was impacted by flood waters) in the last 5 years?
    a. None
    b. 1
    c. 2
    d. 3
    e. 4
    f. 5 or more

5. Please describe those flood events in more detail (e.g., name, date, location, etc.)?
6. Did flood waters enter your home?
    a. Yes
    b. No
    c. Don't recall
7. How high was the flood waters in your home? Estimate as best as you can recall.
    a. 2 inches or less
    b. 3 - 6 inches
    c. 7 - 12 inches
    d. 1 - 2 feet
    e. 3 - 4 feet
    f. 5 - 6 feet
    g. more than 6 feet
8. Did you evacuate?
    a. Yes
    b. No
9. How did you evacuate?
    a. I evacuated on my own with no further help
    b. I evacuated, but required rescue assistance
10. What information did you use to help you evacuate?
11. Did any of the following limit your ability to evacuate from a flood event, whether you did or did not evacuate? Please select all that apply.

a. I didn't have enough time to evacuate to a safer location
b. I didn't have enough money to evacuate to a safer location
c. I didn't know where to go
d. I didn't know what evacuation routes existed
e. I had no access to transportation
f. I felt I could ride out the storm
g. I stayed to protect my home or business
h. My pets/animals made it difficult to evacuate
i. A medical condition or disability (either myself or a family member) made it difficult to evacuate
j. I had to stay for work
k. I stayed to care for family members
l. Other. Please specify:
m. No, I didn't experience any of these barriers

12. What information do you wish you had or wanted to help you evacuate?
13. Did you need help from first responders or volunteers to evacuate? Please check all that apply.
    a. Yes, I asked for evacuation information or directions
    b. Yes, I eventually required rescue assistance after evacuation
    c. No
14. How fast did rescue personnel arrive after you sent out a message or called for help?

a. Less than 30 minutes

b. Between 30 minutes to 1 hour

c. 1-2 hours

d. More than 2 hours

e. More than 6 hours

f. More than 12 hours

g. 1 day or more

h. Never

15. How long did it take for your household to recover from physical damages to your property?

a. No major damages

b. 1 week or less

c. 2-4 weeks

d. 4-8 weeks

e. 2-3 months

f. 4-6 months

g. 7-12 months

h. 1-2 years

i. More than 2 years

16. In the last 5 years, did you participate in rescuing others during the flood event either by boat or car?

a. Yes

b. No

17. Please describe those flood events in more detail (e.g., name, date, location, etc.)?
18. How high was the flood water in the areas of rescue operations you were involved in? If floodwater depths were variable, please check all that apply.
19. How did you get to people in need?
    a. On foot
    b. Surface drive boat (e.g., gator tail)
    c. Flat or short bottom boat
    d. Air boat
    e. Car
    f. Truck
    g. SUV
    h. Other (please specify):
20. What kind of information did you use when trying to get to people in need?
21. What challenges did you experience while conducting rescue operations? Check all that apply.
    a. Didn't know depth of floodwaters
    b. Didn't know where to take people after rescue
    c. Had trouble finding exact locations of victims
    d. Ran into debris
    e. Other (please specify)

22. What information do you wish you had or wanted to help you carry out rescue operations?
23. Do you have a mobile device (smartphone or tablet computer)?
    a. Yes
    b. No
24. Is it Android or iPhone? If you have multiple mobile devices, please check all that apply.
    a. iPhone (Apple)
    b. Android (such as Samsung, LG, Motorola)
25. Do you have access to data without WiFi (only through cellular network) on your mobile device?
    a. Yes
    b. No
26. On a daily basis, how much time do you spend on your mobile device?
    a. Less than an hour
    b. 1-2 hours
    c. 3 or more hours
27. In your opinion, what features should a mobile/computer app have in order to be useful for personal evacuation navigation or flood rescue operation?
28. What is your gender?
    a. Male
    b. Female

c. Non-binary

d. Do not wish to answer

29. What is your race/ethnicity? Please select all that apply.

a. White or Caucasian

b. Black or African American

c. Hispanic

d. Asian

e. American Indian or Alaska Native

f. Native Hawaiian or other Pacific Islander

g. Other

h. Do not wish to answer

30. What is your annual household income?

a. Below $14,000

b. $14,001 … $31,000

c. $31,001 … $63,000

d. $63,001 … $113,000

e. $113,001… $184,000

f. $184,001 … $248,000

g. $248,001 … $475,000

h. Above $475,000

i. Do not wish to answer

31. What is your highest level of education?

a. High school graduate

b. Some college

c. Associate's degree (2-year college)

d. Bachelor's degree (4-year college)

e. Master's degree

f. Doctoral or other professional degree

g. Do not wish to answer

APPENDIX B

PRE-SURVEY AND POST-SURVEY FOR FLOOD RISK PERCEPTION IN IMMERSIVE VIRTUAL REALITY

In this section, the pre-survey and post-survey designed for the study on human's risk perception are presented which are approved by Institutional Review Board (IRB) IRB #2023-0010D on January 24, 2023.

Pre-survey

1. What is your age? (Note: you must be 18 years or older to participate in this study.)

[ ]

2. What is your gender?

- Male
- Female
- Other
- Prefer not to answer

3. Which race or ethnicity best describes you? (Please choose only one.)

- American Indian or Alaskan Native
- Asian / Pacific Islander
- Black or African American
- Hispanic
- White / Caucasian
- Multiple ethnicity/ Other
- Prefer not to answer

4. Please enter the 5-digit ZIP code of your place of residence.

[ ]

5. Do you have prior first-hand experience with any type of flood event (i.e., hurricane, tropical storm, or flood)?

- o Yes
- o No
- o Do not know

6. If you had any first-hand flood experience, please describe those flood events in more detail (e.g., event name, date, location/zip code)? (If not, please report N/A)

[ ]

7. If you had evacuation experience during floods, how did you evacuate? (Please check all that apply.)

- o On foot
- o Surface drive boat (e.g., gator tail)
- o Flat or short bottom boat
- o Airboat
- o Car
- o Truck
- o SUV
- o Other (please specify):
- o N/A

8. How do you get information regarding flood depth for evacuation purposes and choosing the right type of vehicle? (Please check all that apply.)

- o FEMA flood maps
- o Dialing 911
- o Watching news
- o Social media
- o Flood gauges
- o Local measurement
- o Not getting flood depth information
- o Other (please specify):
- o N/A

9. Do you have a mobile device (smartphone or tablet computer)?

- o Yes
- o No

10. Was there any major interruption in your mobile data connectivity during the most recent flood you experienced (if any)?

- o Yes
- o No
- o N/A

11. In your opinion, what features should a mobile/computer app have in order to be useful for personal evacuation navigation or flood rescue operation?

[ ]

Post-survey

1. Rank the objects in the VR environment based on how they were easily recognizable? (1: “least recognizable”; 5: “most recognizable”)

[ ] Car

[ ] Stop sign

[ ] Fire hydrant

[ ] Buildings

[ ] Tree

2. Rank the objects in the VR environment based on how frequently you used them to estimate the depth of water? (1: “used the least”; 5: “used the most”)

[ ] Car

[ ] Stop sign

[ ] Fire hydrant

[ ] Buildings

[ ] Tree